Title
Spin Waves in Magnetic Insulators: Electrical Control of Damping and Low Dissipative Transmission

Author
Liu, Yuxiang

Publication Date
2021

Peer reviewed|Thesis/dissertation

UNIVERSITY OF CALIFORNIA

Los Angeles

Spin Waves in Magnetic Insulators: Electrical Control of Damping and Low Dissipative Transmission

A dissertation submitted in partial satisfaction of the

requirements for the degree Doctor Philosophy

in Electrical and Computer Engineering

by

Yuxiang Liu

2021

ABSTRACT OF THE DISSERTATION

Spin Waves in Magnetic Insulators: Electrical Control of Damping and Low Dissipative Transmission

by

Yuxiang Liu

Doctor of Philosophy in Electrical and Computer Engineering

University of California, Los Angeles, 2021

Professor Kang Lung Wang, Chair

Spin waves are collective excitations in magnetically ordered materials. Early spin-wave devices find applications in microwave technologies. In more recent years, spin waves have been widely considered as an information carrier in the field of magnonics for energy-efficient applications. Spin waves in insulators are free from Ohmic losses but still suffer from magnetic damping. When it comes to thin films, even the ferrimagnetic insulator, yttrium iron garnet (YIG), with extremely low magnetic damping is far from ideal for practical device applications. The spin-wave damping, however, can be compensated with spin-orbit torque (SOT) sourcing from a high spin-orbit coupling (SOC) material in adjacent to the magnetic material. We demonstrate spin-wave amplification at the edge of spin-wave passband with a topological insulator (TI) as the SOC material. We also show that by using alternating Pt and Ta bars as the SOC materials to generate a SOT wave and matching it in phase with the spin waves, the spin waves can be efficiently amplified at a specific wavelength in the main spin-wave passband. On the other hand, the

realization of low dissipative spin superfluid transport in a non-local spin transport configuration has been proposed theoretically, with some recent experimental signatures demonstrated. We show our non-local experimental results based on ferrimagnetic insulator YIG and antiferromagnetic insulator bismuth ferrite (BFO). Electrical control of spin superfluid transport in a magnetic Josephson junction is proposed and investigated numerically for practical spin superfluid device applications.

The dissertation of Yuxiang Liu is approved.

Yaroslav Tserkovnyak

Chandrashekhar Joshi

Robert Candler

Kang Lung Wang, Committee Chair

University of California, Los Angeles

2021

To my wife, my parents, and my friends.

Table of Contents

List of Figures

List of Tables

Acknowledgements

Firstly, I would like to thank my advisor, Prof. Kang L. Wang, for granting me the opportunity of the PhD program after I complete my Master's at UCLA. Everyone has his or her motivations behind taking on the journey of PhD. For me, one of the motivations is to train and acquire the traits of creativity as an engineer and exploration as a scientist. This is exactly what Prof. Wang tried to inspire from us during his class I took before my PhD and what he kept emphasizing in the PhD training. Prof. Wang always challenges us to continuously improve ourselves. Besides knowledge, insights and visions in the specific field, I learned from him during the PhD training, which I value as lifetime assets, including setting high standards, being professional and resourceful, asking significant and fundamental questions, thinking deeply and profoundly, communicating concisely and clearly, the composure when encountering new problems and the confidence in solving them, etc.

Additionally, I would like to thank Prof. Yaroslav Tserkovnyak for his support on the theory side. Not only did I learn physics from him in the class, but I was also able to get a glimpse of the admirable traits of a well-established theorist and inspired by his enthusiasm, insights, sharp mind and persistence in high quality work during the discussions, which is beneficial for me in the long term. I would also sincerely like to thank Prof. Chandrashekhar Joshi and Prof. Robert Candler for their valuable time, efforts, suggestions, comments and patience serving as the committee members. They both are essential for my PhD journey.

Among all the colleagues I worked with and learned from in the research group, Pramey Upadhyaya, now an assistant professor at Purdue University, was one of the first that I met, who, with high intellectual capacity yet a humble spirit, taught me the basics of micromagnetic

simulations, theory and theoretical mindset, how to effectively conduct research, clearly present your work, and even how to use Adobe Illustrator and Latex. Besides Pramey, Aryan Navabi is another colleague that I view as a mentor/friend. Aryan, as an excellent and well-organized scientist/engineer, is always generous in sharing his knowledge and skills, who taught me many most valuable technical skills, suggested useful details on improving my presentations and encouraged me to get out of the most difficult times of my PhD process. Without the help from them, it's hard to imagine where my PhD journey would end.

I would also like to thank colleagues in our group for helping with various aspects: Kin Wong helped with and taught me tips on nanofabrications; Hao Wu supported my research and helped with sputtering of heavy metals; Prof. Gen Yin taught me how to handle conversations under different circumstances; Haoran He always came up with good and fresh suggestions; Lei Pan, Peng Zhang and Lixuan Tai helped with TI film depositions; Xiaoyu Che helped with fabrications and measurements; Koichi Murata helped me with various measurements for the BFO experiments; Mohsen Yazdani and Farbod Ebrahimi introduced me to rf measurements. Other colleagues in the research group I want to thank include Prof. Pedram Khalili, Prof. Guoqiang Yu, Prof. Tian Yu, Mohammad Montazeri, Armin Razavi, Xiang Li, Di Wu, Quanjun Pan, Bingqian Dai, Yabin Fan, Prof. Qiming Shao, and all other group members. I would like to especially express my gratitude to our lab manager Katie Christensen for the support on administrative and academic stuff which greatly smooths my life in the group.

Other people I want to thank at UCLA help with various aspects on research that include Prof. Se Kwon Kim, Héctor Ochoa, Ricardo Zarzuela, Haozhan Tian, Richard Al Hadi, Minji Zhu, Prof. Bing Shen, Jie Xing. Outside UCLA, I would like to thank Prof. Ilya N. Krivorotov (UC Irvine), Prof. Igor Barsukov (UC Riverside), Prof. Joachim Gräfe and Felix Groß (Max Planck Institute

for Intelligent Systems) for their support on theory or experiments. I would also like to thank Toshimitsu Ito (National Institute of Advanced Industrial Science and Technology) for the high quality $BiFeO_3$ samples.

Last but not the least, I would like to thank my wife and my parents. I met my wife, Jiayun Li, at UCLA, started our relationship short after I started my PhD program, and finally got married. Being also a PhD student at UCLA, she shared a similar journey with me and did excellent in her field of study. Her emotional support and my motivation from her are key factors that get to this point of the PhD program. Needless to say, my parents raised me to be what I am, taught me to attend to details when I was young, helped me find interest in the field of science and engineering, and encouraged me to gradually achieve my goals.

Vita

Education

2013 - present	**University of California, Los Angeles, Los Angeles, CA, USA**
2015 - present	Ph.D. candidate in Electrical and Computer Engineering | GPA: 4.0/4.0
2013 - 2015	M.S. in Electrical Engineering | GPA: 3.95/4.0
2009 - 2013	**Tsinghua University, Beijing, China**
	B.S. in Mathematics and Physics | GPA: 90/100

Employment History

2020	Ph.D. Summer Intern
	Facebook, Inc.
	Menlo Park, CA, USA
2018	Ph.D. Summer Intern
	Fremont Research Center, Seagate Technology LLC
	Fremont, CA, USA

Selected Publications and Presentations

- Y. Liu, H. He, A. Navabi, H. Wu, T. Haozhan, T. Itoh, and K. L. Wang. "Spin-Wave Amplification Using Phase-Matched Spin-Orbit-Torque Waves," In Preparation (2021).
- Y. Liu, P. Upadhyaya, S. K. Kim, E. A. Montoya, C. J. Safranski, T. Schneider, I. Barsukov, A. H. MacDonald, I. Krivorotov, Y. Tserkovnyak, and K. L. Wang. "Voltage Control of Superfluid Spin Transport in Magnetic Josephson Junction," In Preparation (2021).
- A. Navabi*, Y. Liu*, P. Upadhyaya, K. Murata, F. Ebrahimi, G. Yu, B. Ma, Y. Rao, M. Yazdani, M. Montazeri, L. Pan, I. N. Krivorotov, I. Barsukov, Q. Yang, P. Khalili Amiri, Y. Tserkovnyak, and K. L. Wang. "Control of Spin-Wave Damping in YIG Using Spin Currents from Topological Insulators," *Physical Review Applied* 11 (3): 034046 (2019). *equal contribution
- Y. Liu, P. Upadhyaya, S. K. Kim, E. A. Montoya, C. J. Safranski, I. Barsukov, A. H. MacDonald, I. Krivorotov, Y. Tserkovnyak, and K. L. Wang. "Voltage Control of Superfluid

Spin Transport in Magnetic Josephson Junction," 62nd Annual Conference on Magnetism and Magnetic Materials, Pittsburgh, PA (2017 November).

- A. Navabi, Y. Liu, P. Upadhyaya, G. Yu, M. Yazdani, K. Murata, M. Montazeri, F. Ebrahimi, P. K. Amiri, Y. Tserkovnyak, and K. L. Wang. "Spin-Wave Amplification in YIG/Pt System: Frequency and Bias Magnetic Field Dependencies," 62nd Annual Conference on Magnetism and Magnetic Materials, Pittsburgh, PA (2017 November).
- H. Wu, J. Nance, S. A. Razavi, D. Lujan, B. Dai, Y. Liu, H. He, B. Cui, D. Wu, K. Wong, K. Sobotkiewich, X. Li, G. P. Carman, and K. L. Wang. "Chiral Symmetry Breaking for Deterministic Switching of Perpendicular Magnetization by Spin–Orbit Torque," *Nano Letters* (2020).
- H. Wu, F. Groß, B. Dai, D. Lujan, S. A. Razavi, P. Zhang, Y. Liu, K. Sobotkiewich, J. Förster, M. Weigand, G. Schütz, X. Li, J. Gräfe, and K. L. Wang. "Ferrimagnetic Skyrmions in Topological Insulator/Ferrimagnet Heterostructures," *Advanced Materials* 32 (34): 2003380 (2020).
- H. Wu, S. A. Razavi, Q. Shao, X. Li, K. L. Wong, Y. Liu, G. Yin, and K. L. Wang. "Spin-Orbit Torque from a Ferromagnetic Metal," *Physical Review B* 99 (18): 184403 (2019).
- T. Schneider, D. Hill, A. Kakay, K. Lenz, J. Lindner, J. Fassbender, P. Upadhyaya, Y. Liu, K. L. Wang, Y. Tserkovnyak, I. N. Krivorotov, and I. Barsukov. "Self-Stabilizing Spin Superfluid," *ArXiv:1811.09369* (2018).
- Q. L. He, X. Kou, A. J. Grutter, G. Yin, L. Pan, X. Che, Y. Liu, T. Nie, B. Zhang, S. M. Disseler, B. J. Kirby, W. Ratcliff Ii, Q. Shao, K. Murata, X. Zhu, G. Yu, Y. Fan, M. Montazeri, X. Han, J. A. Borchers, and K. L. Wang. "Tailoring Exchange Couplings in Magnetic Topological-Insulator/Antiferromagnet Heterostructures," *Nature Materials* 16 (1): 94–100 (2017).

1 Introduction

Spin waves are collective excitations in magnetically ordered materials. Since the spin waves concept was first proposed in 1930s [1], it has been intensively investigated and implemented in microwave technology applications [2], [3] such as microwave filters [4], signal-to-noise enhancers [5] and frequency selective limiters [6]. In more recent years, research interest in spin waves are probably motivated by the wide consideration that the concept of spin waves used as the information carrier in the field of magnonics [7] can be readily employed for spintronic applications.

Spintronics, or spin electronics, is a field that uses spin degrees of freedom in solid-state systems for computation, storage, etc [8], [9]. Compared with conventional electronics, where devices based on electron charges for logic operations and power amplification are volatile and hence consume considerable amount of power to retain the information, spintronic devices based on electron spin manipulations can be non-volatile due to hysteresis in magnetic systems. Therefore, spintronic devices can be energy efficient, which is crucial to address the rapidly growing energy demand in nowadays information technology.

The field of magnon spintronics [10] emerged with the usage of magnonic approaches in spintronics where information is transmitted and processed in the magnonic systems utilizing the wave nature and various unique properties of magnons. The additional benefits of data processing in magnonic system include, just to list a few: the wavelengths of the spin waves can reach nanometers, making down scaling of device sizes feasible; the operating frequencies of spin-wave devices can range from GHz to THz, selected by different magnetic materials and tunable by

applied magnetic fields; magnons as bosons can form a Bose-Einstein condensate (BEC) [11], [12], a coherent state that can have long magnon lifetime even at room temperature, etc.

While in magnon spintronics, highly efficient magnon excitations by spin-transfer torques that bridge spintronics and electronics are important for practical applications, spin transport with minimal losses is of equal importance for energy-efficient considerations. Spin waves in insulators, free from Ohmic losses, can benefit from energy-efficient insulator-based technology. In insulating magnetic materials, however, spin waves still suffer from the intrinsic magnetic damping of materials, which may be worsen with materials of low growth quality. Among all the insulating magnetic materials, yttrium iron garnet (YIG) has been the go-to material for device applications, mainly due to its extremely low magnetic damping. When it comes to thin films, however, the damping without compensation is far from ideal for practical device applications.

We shall see that spin waves can be viewed as magnetization precessions, and thus an intuitive method to counter spin-wave damping is to apply a torque in phase with the spin waves. Materials with high spin-orbit coupling (SOC), such as 5d transition metals and topological insulators (TIs) can efficiently generate spin currents (i.e., flow of spin angular momentum) as driven by an applied electron (charge) current, an emerging effect [13]. In a heterostructure composed of a high SOC material and an adjacent magnetic material, the spin current generated by SOC will flow into the magnetic material to effectively exert an spin orbit torque (SOT) onto the magnetization to reduce the spin-wave damping [14]–[16] or to switch its equilibrium direction [17], [18].

On the other hand, spin superfluidity, a phenomenon closely related to BEC of magnons, offers the possibility of low dissipative spin transport carried by the spin supercurrents. Theoretical proposal of realizing spin superfluid in easy-plane magnet sandwiched by two SOC materials were suggested [19], [20] and experimental signatures have been observed in non-local spin transport

setup based on antiferromagnetic insulators [21], [22]. While continuing research efforts have been made towards finding suitable material systems to realize spin superfluid at room temperature, investigations on control of superfluid spin transport are needed for practical device applications.

We have so far explained the technological background and the need to reduce magnetic damping for practical applications as the motivations behind the research conducted in this dissertation. In Chapter 2, we shall describe the relevant fundamental theory to help understand the findings of this dissertation, with a focus on the magnetic dynamics and its governing equation, Landau-Lifshitz-Gilbert (LLG) equation, which lays the foundations for classical spin-wave theory and spin superfluid. Spin Hall effect (SHE) will be introduced as the source of spin currents or SOT for reduction of spin-wave damping and excitation of incoherent magnons or spin superfluid.

The numerical methods used for studying spin-wave excitation by microwave antennas and spin-wave dynamics, will be discussed in Chapter 3. The LLG equation on spin-wave dynamics will be solved both numerically in a single domain mode and in micromagnetics simulations based on LLG Micromagnetics Simulator and MuMax3; the Oersted field for spin-wave excitation, along with other relevant simulations, will be calculated in COMSOL for design and verification purposes. Experimental methods involved in the dissertation will be discussed in Chapter 4, including propagating spin-wave spectroscopy (PSWS) used for the spin-wave damping compensation experiments and current-reversal method/delta method used for the non-local spin transport experiments.

Spin-wave amplification is investigated for coherent spin waves excited inductively by microwave antennas. We shall present the work on SOT induced damping compensation in YIG based on 1) the conventional spin-wave amplification configuration, where TI replaces 5d transition metals as the SOC material to provide the SOT with an improved efficiency, in Chapter 5, and 2) the “comb”

configuration generating a SOT wave to more efficiently transfer energy to the spin waves to amplify them, in Chapter 6.

Non-local spin transport scheme, where spin injection and detection are based on the SHE and the inverse SHE (ISHE), respectively, is used for incoherent magnon transport and spin superfluid experiments. In Chapter 7, we shall present our results on non-local spin transport experiments in magnetic insulators. In Chapter 8, we finally discuss our work on electrical control of the spin superfluid in the non-local spin transport scheme for practical device applications.

2 Fundamental Theory

In this chapter, we will describe the fundamental theory that is relevant to the research conducted in this dissertation. More details of these topics can be found in [23]–[28], [20], [19]. We will first describe the origin of magnetism and different types of magnetism in Section 2.1. The magnetic dynamics under the context of micromagnetics will then be introduced with its equation of motion, Landau-Lifshitz-Gilbert (LLG) equation, and the typical magnetic energy terms involved in Section 2.2. This then lays the foundations for classical spin-wave theory and spin superfluid, which will be described in Section 2.3 and 2.4, respectively. Finally, we will introduce spin Hall effect (SHE) as a source of spin currents in Section 2.5, which will be used for spin-wave damping reduction and spin injection in non-local spin transport.

2.1 Magnetism

Magnetism is originated from electrons of atoms in solid state materials. An electron of an atom has two kinds of angular momenta associated with it: orbital $\boldsymbol{L}$ and spin $\boldsymbol{S}$, which can be schematically viewed as shown in Figure 2-1. The orbital motion contributes to the magnetic moment as a current loop generates magnetic field and hence the magnetic moment. The electron spins, on the other hand, have no classical analogue. In quantum theory, electron is a spin-$\frac{1}{2}$ particle, with $S_z = +\frac{\hbar}{2}$ and $S_z = -\frac{\hbar}{2}$, referred to as "spin up" and "spin down" states, respectively, and electron spin also contributes to magnetic moment. Due to Hund's law, however, the spin magnetic

moments from up- and down-spin on the same orbit cancel each other, leaving only certain atoms or ions possessing permanent magnetic moments.

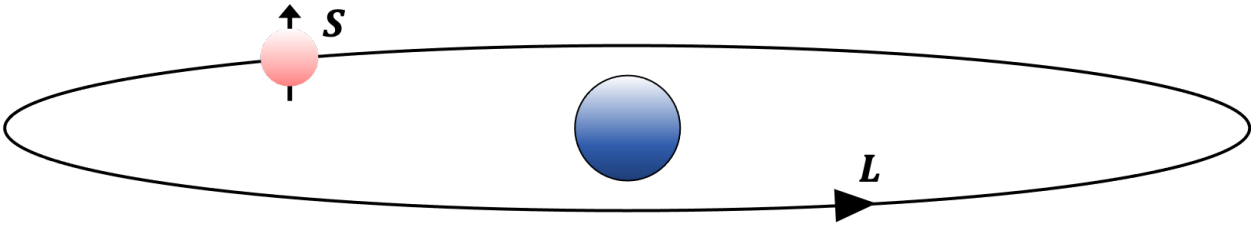

Figure 2-1 Illustration of the origin of magnetism, where the electron orbiting around the nucleus ($\boldsymbol{L}$) with its spin ($\boldsymbol{S}$) contributing to the magnetic moment associated with it.

The solid-state materials that consist of atoms or ions with permanent magnetic moments can be classified into four types depending on how they are ordered: paramagnetic, ferromagnetic, antiferromagnetic and ferrimagnetic materials, schematically shown in Figure 2-2. In paramagnetic materials, the magnetic moments are randomly aligned without a long-range order and thus have vanishing total magnetic moment. Under the application of magnetic field, the magnetic moments can be partially aligned generating a net magnetic moment.

The remaining three types of magnetic materials all have a long-range magnetic order below a certain transition temperature. In ferromagnetic materials, the exchange interaction between adjacent magnetic moments causes them to align in parallel, which leads to a spontaneous magnetic moment in the absence of external magnetic field. In antiferromagnetic and ferrimagnetic materials, on the other hand, the exchange interaction between adjacent magnetic moments induces antiparallel alignment between them, which can be viewed as two opposingly coupled ferromagnetic sublattices. The difference between antiferromagnetic and ferrimagnetic materials are that the antiparallelly aligned magnetic moments are of equal and unequal magnitudes, respectively.

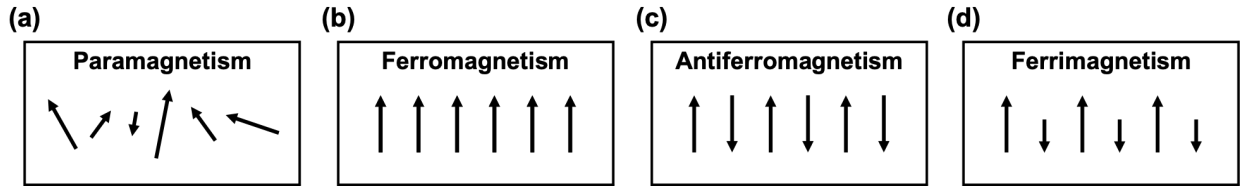

Figure 2-2 Four types of magnetism from materials with permanent magnetic moments: (a) paramagnetism, (b) ferromagnetism, (c) antiferromagnetism, (d) ferrimagnetism.

The material used for spin-wave damping reduction experiments and non-local magnon diffusion-relaxation transport experiment, yttrium iron garnet (YIG), is ferrimagnetic. The other material used for non-local transport measurement, bismuth ferrite (BFO), has antiferromagnetic order.

2.2 Magnetic Dynamics

In this section, we will briefly describe the micromagnetic model [29], [30] with a focus on the equation of motion, the Landau-Lifshitz-Gilbert (LLG) equation.

Micromagnetics deals with magnetic phenomena at sub-micron length scale, which is small enough to resolve magnetic structures such as domain walls, yet large enough to ignore the detailed atomic structure of materials. In this length scale, the continuum approximations can be applied such that magnetization as the spatially averaged magnetic moments: $\boldsymbol{M}(\boldsymbol{r}) = \frac{\sum_i \boldsymbol{\mu_i}}{dV_{\boldsymbol{r}}}$, varies smoothly in space and time.

Under the continuum approximations, the magnetization precession under the application of a magnetic field $\boldsymbol{H}$ according to the momentum theorem follows: $\frac{\partial \boldsymbol{M}}{\partial t} = -\gamma \boldsymbol{M} \times \boldsymbol{H}$, shown in Figure 2-3, where is γ the gyromagnetic ratio. Landau and Lifshitz first proposed the formalism of the precessional motion of the magnetization in 1935 and introduced an additional torque term to account for the magnetic dissipation. The corresponding equation is referred to as Landau-Lifshitz (LL) equation:

$$\frac{\partial \boldsymbol{M}}{\partial t} = -\gamma \boldsymbol{M} \times \boldsymbol{H}_{\boldsymbol{eff}} - \frac{\lambda}{M_S} \boldsymbol{M} \times (\boldsymbol{M} \times \boldsymbol{H}_{\boldsymbol{eff}}) \tag{2.1}$$

where $\boldsymbol{H}_{\boldsymbol{eff}}$ is the total effective field that takes into account the contributions from different magnetic interactions, which we will soon discuss, and λ is a phenomenological constant characterizing the damping of the magnetic material.

In 1955, Gilbert took a different approach and introduced the phenomenological damping as a "viscous" force [31]. The corresponding equation is generally referred to as Landau-Lifshitz-Gilbert (LLG) equation:

$$\frac{\partial \boldsymbol{M}}{\partial t} = -\gamma \boldsymbol{M} \times \boldsymbol{H}_{\boldsymbol{eff}} + \frac{\alpha}{M_S} \boldsymbol{M} \times \frac{\partial \boldsymbol{M}}{\partial t} \tag{2.2}$$

It should be noted that precessional motion has the magnetization magnitude preserved for both forms of the damping terms in LL and LLG equations. Additionally, it can be shown that Equation (2.2) can be transformed into the following equation:

$$\frac{\partial \boldsymbol{M}}{\partial t} = -\frac{\gamma}{1+\alpha^2} \boldsymbol{M} \times \boldsymbol{H}_{\boldsymbol{eff}} - \frac{\gamma\alpha}{(1+\alpha^2)M_S} \boldsymbol{M} \times (\boldsymbol{M} \times \boldsymbol{H}_{\boldsymbol{eff}}) \tag{2.3}$$

By having $\gamma_L = \frac{\gamma}{1+\alpha^2}$ and $\lambda = \frac{\gamma\alpha}{1+\alpha^2}$, Equation (2.3) becomes Equation (2.1). Therefore, LL and LLG equations are mathematically identical. They are considered the equation of motion for magnetic dynamics with a conserved magnitude of magnetization.

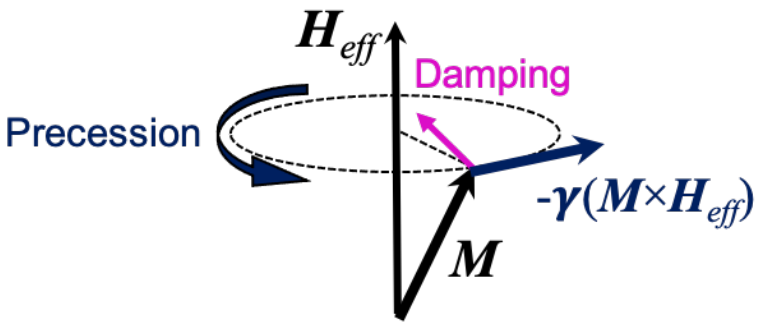

Figure 2-3 Magnetic dynamics illustrated as the gyromagnetic precession with a damping torque.

A key quantity in the equation is the total magnetic field $\boldsymbol{H_{eff}}$, the local field felt by the magnetization $\boldsymbol{M}(\boldsymbol{r})$ at $\boldsymbol{r}$, which can be calculated from the total free energy of the magnetic system, E_{tot}:

$$\boldsymbol{H_{eff}} = -\frac{\delta E_{tot}}{\delta \boldsymbol{M}} \tag{2.4}$$

There typically exist 4 contributions to E_{tot}: the Zeeman energy E_h, the magnetostatic energy E_h, the exchange energy E_{ex} and the anisotropy energy E_{an}.

$$E_{tot} = E_h + E_m + E_{ex} + E_{an} \tag{2.5}$$

Zeeman energy is the energy of a magnetic body subject to an externally applied magnetic field $\boldsymbol{H_a}$ and can be calculated as:

$$E_h = -\mu_0 \int \boldsymbol{M} \cdot \boldsymbol{H_a} d^3\boldsymbol{r} \tag{2.6}$$

The magnetostatic energy corresponds to the long-range dipolar interaction calculated as:

$$E_m = -\frac{\mu_0}{2} \int \boldsymbol{M} \cdot \boldsymbol{H_d} d^3\boldsymbol{r} \tag{2.7}$$

where $\boldsymbol{H_d}$ is the demagnetization field, which can be solved from magnetostatic Maxwell equations:

$$\nabla \times \boldsymbol{H_d} = 0 \tag{2.8}$$

$$\nabla \cdot \boldsymbol{B} = \mu_0 \nabla \cdot (\boldsymbol{H_d} + \boldsymbol{M}) = 0 \tag{2.9}$$

The solutions are:

$$\boldsymbol{H_d} = -\nabla\Phi_M \tag{2.10}$$

$$\Phi_M(\boldsymbol{r}) = -\frac{1}{4\pi}\int \frac{\nabla' \cdot \boldsymbol{M}(\boldsymbol{r}')}{|\boldsymbol{r}-\boldsymbol{r}'|} d^3\boldsymbol{r}' \tag{2.11}$$

The exchange energy stems from the short-range exchange interactions of pure quantum mechanical origin. The Heisenberg Hamiltonian considering only the nearest neighbor interactions for a cubic lattice of n spins is given by:

$$E_{ex} = -2J\sum \boldsymbol{S_i} \cdot \boldsymbol{S_j} \tag{2.12}$$

where J is the nearest neighbor exchange integral. In the semiclassical model, $\boldsymbol{S_i}$ and $\boldsymbol{S_j}$ can be viewed as vectors with small angle θ_{ij} in between them, and thus Equation (2.12) can be written as:

$$\begin{aligned} E_{ex} = -2JS^2\sum \cos\theta_{ij} &\approx \text{const} + JS^2\sum \theta_{ij}^2 \\ &\approx \text{const} + JS^2\sum \left(\boldsymbol{m_i} - \boldsymbol{m_j}\right)^2 \\ &= \text{const} + JS^2\sum \left(\Delta\boldsymbol{r_{ij}} \cdot \nabla\boldsymbol{m}\right)^2 \end{aligned} \tag{2.13}$$

where $\boldsymbol{m_i}$ and $\boldsymbol{m_j}$ are the directional vectors of $\boldsymbol{S_i}$ and $\boldsymbol{S_j}$, and $\Delta\boldsymbol{r_{ij}} = \boldsymbol{r_i} - \boldsymbol{r_j}$. Considering the cubic symmetry and neglecting the constant term irrelevant to equilibrium or dynamics, Equation (2.13) can be written in terms of the integration of the exchange-energy density:

$$E_{ex} = \int A(\nabla\boldsymbol{m})^2 d^3\boldsymbol{r} \tag{2.14}$$

where $\boldsymbol{m}$ can be written as $\boldsymbol{m} = \frac{\boldsymbol{M}}{M_S}$ and $A = \frac{1}{6}nJS^2\sum \Delta\boldsymbol{r_{ij}^2}$ for the cubic symmetry. The exchange energy expression of Equation (2.14) still holds for other types of symmetries.

The anisotropy energy mostly results from the material structure. The most common case is there exists a certain energy-favored direction for the magnetization direction to be aligned along, which is called the easy axis of the magnetic material. The anisotropy energy can be expressed in terms of the integration of anisotropy-energy density [1]:

$$E_{an} = \int f_{an} d^3\boldsymbol{r} \tag{2.15}$$

where the anisotropy energy density f_{an} in the case of materials with easy axis, that is, materials with uniaxial anisotropy, can be expressed in the spherical coordinate with the easy axis along z axis as:

$$f_{an} = K_0 + K_1 \sin^2\theta + \cdots \tag{2.16}$$

where K_i are anisotropy constants at different order. The anisotropic behavior mainly depends on the K_1 term. When K_1 is positive, the energy minimum occurs at $\theta = 0$ or π, and this is the easy axis situation with the magnetization preferably aligning along z or $-z$ direction. When K_1 is negative, however, the energy minimum occurs at $\theta = \frac{\pi}{2}$ corresponding to the xy plane, and thus instead of an easy axis, the material has an easy plane for the magnetizations to align along any direction on the plane, or equivalently speaking, there exists a spin-rotational symmetry. In the situation of easy plane anisotropy, spin superfluid can be supported, which we shall discuss in Section 2.4.

Due to the nonlinear nature of the LL and LLG equations, linear approximations are necessary for the analytical solutions. These analytical solutions are very powerful in understanding and even

[1] In literatures, both "+" and "-" sign can be found in front of the integral in the expression of anisotropy energy (i.e., $E_{an} = \int f_{an} d^3\boldsymbol{r}$ and $E_{an} = -\int f_{an} d^3\boldsymbol{r}$), such as in [24] and [32], respectively. Both conventions have their corresponding signs of K_i [see Equation (2.16)], the anisotropy constants. In this dissertation, we adopt the convention of "+" sign such that the negative K_1 indicates the easy-plane anisotropy.

quantifying the physics phenomena. We shall discuss two examples with different linearization process for the theory of spin waves and spin superfluid in Section 2.3 and Section 2.4, respectively.

2.3 Spin Waves

We now focus our discussion on the magnetostatic spin waves with an external fixed magnetic field $\boldsymbol{H}$ applied along the z direction. We first consider the dipolar spin waves with only the Zeeman energy and magnetostatic energy and ignore the damping term in Equation (2.2), that is $\boldsymbol{H_{eff}} = \boldsymbol{H} + \boldsymbol{h}(t)$ and $\alpha = 0$, where $\boldsymbol{h}(t) = \boldsymbol{h}e^{-i\omega t}$ is small. For the linearization, we consider the situation of a small deviation $\boldsymbol{m}(t) = \boldsymbol{m}e^{-i\omega t}$ in the magnetization vector from z axis, $\boldsymbol{M} = \boldsymbol{M_0} + \boldsymbol{m}(t)$, and we can derive the following relation from the LLG equation:

$$\boldsymbol{m} = \bar{\chi}\boldsymbol{h} \tag{2.17}$$

where $\bar{\chi}$ is the Polder susceptibility tensor with the expressions of χ and κ as:

$$\bar{\chi} = \begin{bmatrix} \chi & -i\kappa & 0 \\ i\kappa & \chi & 0 \\ 0 & 0 & 0 \end{bmatrix} \tag{2.18}$$

$$\chi = \frac{\omega_H \omega_M}{\omega_H^2 - \omega^2} \tag{2.19}$$

$$\kappa = \frac{\omega \omega_M}{\omega_H^2 - \omega^2} \tag{2.20}$$

In the above equations, $\omega_H = \gamma \mu_0 H$ and $\omega_M = \gamma \mu_0 M_S$. When damping is considered, ω_H should be replaced with $\omega_H - i\alpha\omega$.

For the magnetostatic Maxwell equations, similar to Equation (2.8) and (2.9), we have:

$$\nabla \times \boldsymbol{h} = 0 \tag{2.21}$$

$$\nabla \cdot \boldsymbol{b} = \mu_0 \nabla \cdot (\boldsymbol{h} + \boldsymbol{m}) = 0 \tag{2.22}$$

Also similar to Equation (2.10), we can then introduce a scalar potential $\boldsymbol{h} = -\nabla\Phi$ based on Equation (2.30). Equation (2.31) then leads to the Walker equation:

$$(1+\chi)\left[\frac{\partial^2\Phi}{\partial x^2} + \frac{\partial^2\Phi}{\partial y^2}\right] + \frac{\partial^2\Phi}{\partial z^2} = 0 \tag{2.23}$$

For a thin film of thickness d, i.e., $x \in [-\frac{d}{2}, \frac{d}{2}]$, and extended infinitely in yz plane, as shown in Figure 2-4. We look for the plane wave solution, i.e., $\Phi \propto e^{i\boldsymbol{k}_\parallel \cdot \boldsymbol{r}}$, propagating in yz plane with $\boldsymbol{k}_\parallel = (0, k_\parallel \sin\varphi, k_\parallel \cos\varphi)$ with φ being the angle between the spin-wave propagation direction and magnetic field direction. Considering the boundary conditions that the tangential component of $\boldsymbol{h}$ and the normal component of $\boldsymbol{b} = \mu_0(\boldsymbol{m} + \boldsymbol{h})$ are continuous at $x = \pm\frac{d}{2}$, the general dispersion relation of dipolar spin waves can thus be obtained as:

$$k_\parallel^2 - (1+\chi)^2 k_\perp^2 - \kappa^2 k_\parallel^2 \sin^2\varphi + 2(1+\chi)k_\perp k_\parallel \cot(k_\perp d) = 0 \tag{2.24}$$

where $k_\perp = k_\parallel \sqrt{-\frac{1+\chi\sin^2\varphi}{1+\chi}}$ corresponds to the wavevector along x perpendicular to $\boldsymbol{k}_\parallel$, and the dependency of Φ on x is sinusoidal inside the film and exponentially decaying outside the film (shown in Figure 2-4).

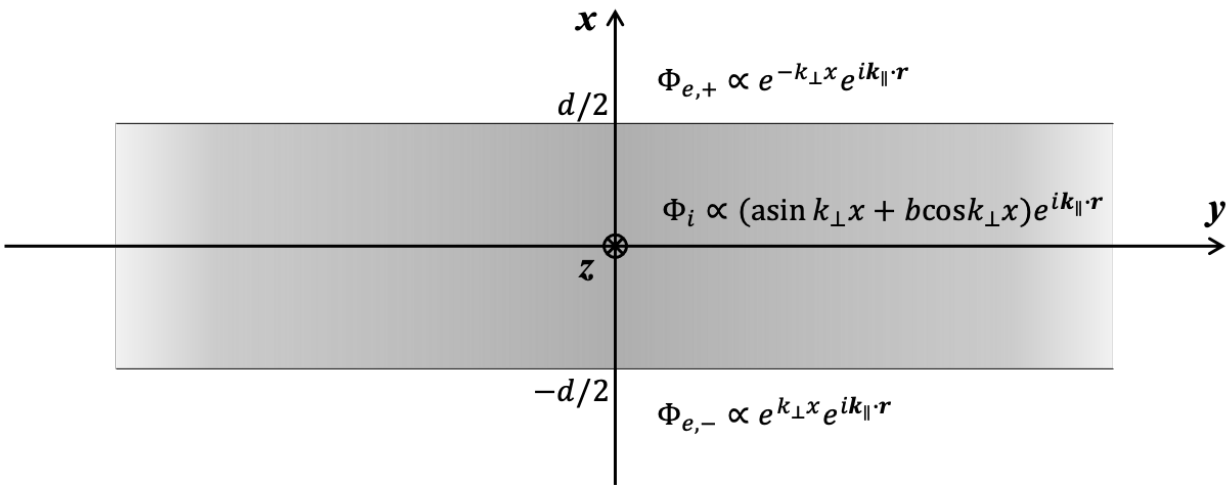

Figure 2-4 The in-plane magnetized thin film considered for the dipolar spin waves. The external field $\boldsymbol{H}$ is applied along the z direction. The form of the magnetostatic potential expression is marked in different regions, with "i" and "e" indicate the interior and exterior regions of the film and "+", "-" indicate the $+x$ and $-x$ region. $k_\parallel$ and $k_\perp$ correspond to the wavevectors in the yz plane and along the x direction, respectively.

When $k_\perp$ is real, the spin-wave mode is called backward volume magnetostatic waves (BVMSWs), with "backward" indicating that the group velocity, $v_g = d\omega/dk$, is negative, and "volume" indicating that the spin waves are extended across the entire thickness of the film.

When $k_\perp$ is imaginary, the spin-wave mode is called magnetostatic surface waves (MSSWs). This spin-wave mode decays exponentially inside the film and thus localized at the surface of the film. It has a unique property that when excited inductively by an antenna, that is $\boldsymbol{m}(t)$ couples to the $\boldsymbol{h}(t)$ induced by rf currents $\boldsymbol{J}$ in the antenna, the spin-wave at the top and bottom surface of the film propagates to opposite directions under a given $\boldsymbol{H}$ direction, as shown in Figure 2-5. This is the non-reciprocity property of the MSSWs. The difference of phase distribution between $\boldsymbol{m}(t)$ at the top and bottom surfaces results from the dynamic dipolar field generated from them [33], which leads to $-k_y$ and $+k_y$ for the top and bottom surface spin waves and thus the non-reciprocity. The spin waves discussed in this dissertation are the MSSWs.

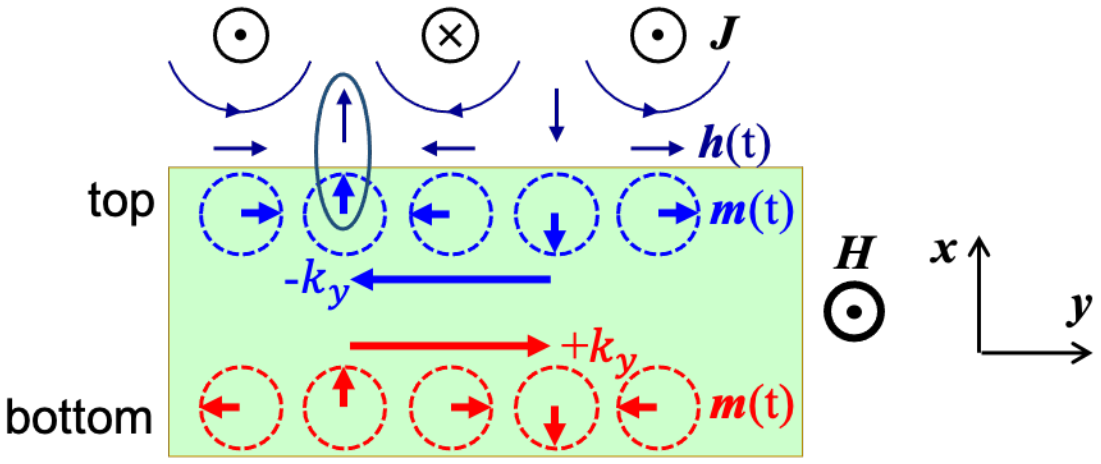

Figure 2-5 Illustration of non-reciprocity of MSSW. The top and bottom surface $\boldsymbol{m}(t)$ have different phase distributions resulted from the dynamic dipolar field generated from them, which leads to $-k_y$ and $+k_y$ for the top and bottom spin waves.

For two special cases, $\boldsymbol{H} \perp \boldsymbol{k}_{\parallel}$ and $\boldsymbol{H} \parallel \boldsymbol{k}_{\parallel}$, the former being a MSSW and the latter being a BVMSW, their dispersion relations can be simplified from Equation (2.24) as:

$$\omega_{MSSW}^2 = \omega_H(\omega_H + \omega_M) + \frac{\omega_M^2}{4}(1 - e^{-2k_{\parallel}d}) \tag{2.25}$$

$$\omega_{BVMSW}^2 = \omega_H\left[\omega_H + \omega_M\left(\frac{1 - e^{-k_{\parallel}d}}{k_{\parallel}d}\right)\right] \tag{2.26}$$

The situation with exchange interaction included is a bit more complicated, we shall skip the mathematical details and only present the result as [34]:

$$\omega^2 = \left[\omega_H + \gamma\frac{2A}{M_S}k^2 + \omega_M(1 - P_n)\right]\left(\omega_H + \gamma\frac{2A}{M_S}k^2 + \omega_M P_n \sin^2\varphi\right) \tag{2.27}$$

where $P_n = \frac{k_{\parallel}^2}{k_{\parallel}^2+\kappa_n^2} - \left(\frac{k_{\parallel}^2}{k_{\parallel}^2+\kappa_n^2}\right)^2 \frac{F_n}{\sqrt{2(1+\delta_{0n})}}$ and $F_n = 2\frac{1-(-)^n e^{-k_{\parallel}d}}{k_{\parallel}d}$, $k^2 = k_{\parallel}^2 + \kappa_n^2$, $\kappa_n = \frac{n\pi}{d}$.

Figure 2-6 shows the dispersion curves calculated numerically based on Equation (2.27) with n = 0 (i.e., $k = k_{\parallel}$, no thickness mode considered). Other parameters are set as $\boldsymbol{H} = 600$ Oe and $d =$

1 μm with YIG material parameters. By changing the value of $\boldsymbol{H}$, the dispersion curve can be shifted up and down, and thus for spin waves with certain wavevectors, the spin-wave frequency can be tuned by the external field value.

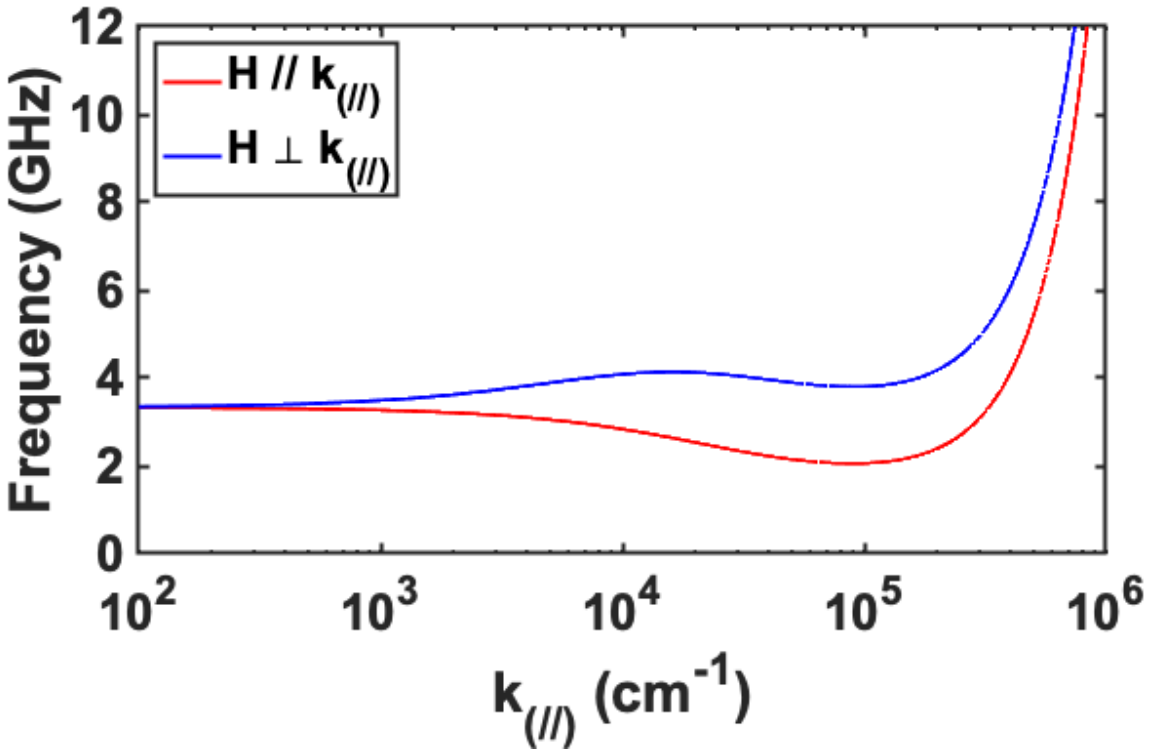

Figure 2-6 Dipolar exchange spin-wave dispersion curves calculated numerically based on Equation (2.27) with $n = 0$ (i.e., $k = k_{\parallel}$, no thickness mode considered). Other parameters are set as $\boldsymbol{H} = 600\ Oe$ and $d = 1\ \mu m$ with YIG material parameters.

It is worth mentioning that for the situation when the external magnetic field is applied perpendicular to the film along the x direction in Figure 2-4, the corresponding spin-wave mode is a forward volume magnetostatic wave (FVMSW). More details of this mode can be found in the references listed at the beginning of this chapter.

Finally, we comment that by quantum treatment (refer to [35] for the Holstein-Primakoff approach), the Hamiltonian of multi-spin systems coupled through exchange and dipolar interactions can be written as:

$$\mathcal{H} = \sum_k \hbar\omega_k \alpha_k^\dagger \alpha_k \tag{2.28}$$

This Hamiltonian is in analogy to that of harmonic oscillators. This quantum treatment yields the quanta of spin waves, called magnon. Similarly, $\alpha_k^\dagger$ and α_k are magnon creation and annihilation operators, respectively, and $n_k = \alpha_k^\dagger \alpha_k$ is the magnon number operator. The coherent state of magnon is given as the eigenstate of α_k (i.e., $\alpha_k|c_k\rangle = c_k|c_k\rangle$) as:

$$|c_k\rangle = e^{-\frac{1}{2}|c_k|^2} \sum_{n_k=0}^{\infty} \frac{(c_k)^{n_k}}{(n_k!)^{1/2}} |n_k\rangle \tag{2.29}$$

The average spin components in this coherent state are plane waves [2] and thus recover the classical spin-wave behaviors.

2.4 Spin Superfluid

Spin superfluidity refers to the ability to support dissipationless spin transport. In a magnetic system with the U(1) spin-rotational symmetry, such as in an easy-xy-plane ferromagnet, the small z projection of spin follows a loose conservation law, leading to an algebraic rather than exponential decay of spin supercurrents.

We consider only exchange interaction and anisotropy energy in this case, and $E_{tot} = \int d^3\boldsymbol{r}[A(\nabla \boldsymbol{n})^2 + Kn_z^2]/2$ where $\boldsymbol{n}$ is the unit vector along spin density vector $\boldsymbol{s}$ and can be

[2] The average spin components in the coherent state can be calculated as $\langle S_i^{x(y)} \rangle = \left\langle c_k \middle| S_i^{x(y)}(t) \middle| c_k \right\rangle$. Then we can obtain $\langle S_i^x \rangle \propto \cos(\boldsymbol{k}\cdot\boldsymbol{r_i} - \omega_k t + \beta_k)$ and $\langle S_i^y \rangle \propto \sin(\boldsymbol{k}\cdot\boldsymbol{r_i} - \omega_k t + \beta_k)$, where β_k is the phase of c_k. These plane wave solutions represent the spin precession.

parametrized as $\boldsymbol{n} = (\sqrt{1 - n_z^2}\cos\varphi, \sqrt{1 - n_z^2}\sin\varphi, n_z)$ in the spherical coordinate. Unlike the spin-wave case where the linearization is carried out by considering the small $\boldsymbol{m}$ deviated from the precession axis, we consider the situation with small n_z in the spin superfluid. In the strong-anisotropy and long-wavelength limit, i.e., $\lambda \gg \sqrt{A/K}$, we can expand LLG equation [Equation (2.1)] into different orders of n_z, consider only the lowest order, we arrive at the following equations where the spin density $s = \frac{M_S}{\gamma}$:

$$\dot{\varphi} = Kn_z/s + \alpha\dot{n}_z \tag{2.30}$$

$$\dot{n}_z = A\nabla^2\varphi/s - \alpha\dot{\varphi} \tag{2.31}$$

In the absence of damping, these two equations are essentially coupled Hamilton equations with φ and sn_z as canonically conjugated variables. Similar to the charge density continuity equation, $\dot{\rho} + \nabla \cdot \boldsymbol{J} = 0$, a spin supercurrent can be defined from Equation (2.31) ($\alpha = 0$) as $\boldsymbol{J_S} = -A\nabla\varphi$.

The spin superfluid can be induced by injecting z spins into an easy plane ferromagnet from a spin injector on the left in the structure with translation symmetry along y and z directions as shown in Figure 2-7. The detection of the spin supercurrent at the detector can be based on the inverse process of spin injection. The steady state solutions of Equations (2.30) and (2.31) are $n_z(\boldsymbol{x}) = \text{const} \equiv n_z$ and $\varphi(\boldsymbol{x}, t) = \varphi(\boldsymbol{x}) + \Omega t$, where n_z is the small z projection of spin in the linear regime and the precession frequency is $\Omega = Kn_z/s$, that is a global precession of a spiraling magnetic texture in the easy plane. The dissipation of spin supercurrent is linear: $J_S^L - J_S^R = \alpha s\Omega L$ with L being the distance between the spin injector and detector.

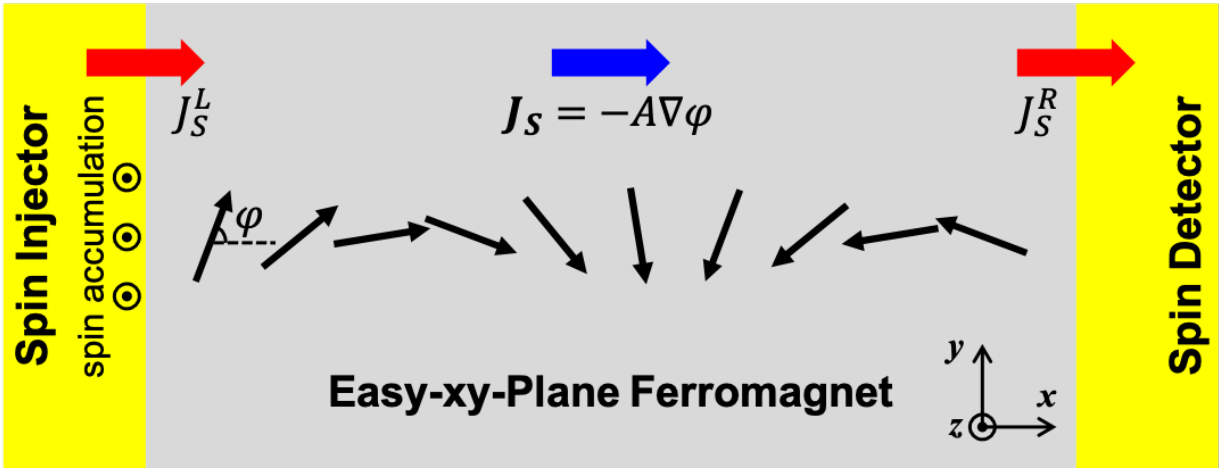

Figure 2-7 Schematic of realizing spin superfluid in an easy-xy-plane ferromagnet. A spin supercurrent $\boldsymbol{J_S} = -A\nabla\varphi$ is transported from the spin injector to the spin detector carrying a small z projection of spin.

2.5 Spin Currents

Generally speaking, just like electric charge current is a flow of charges, spin current is a flow of spins. In spintronics, spin current is typically generated from spin polarized electric current via spin Hall effect (SHE) in 5d transition metals or from the surface states of topological insulators (TIs) as a result of the spin-orbit coupling (SOC).

The spin Hall effect was first introduced by Hirsch [36] in analogy with the Hall effect that charges accumulated laterally in an electrical conductor developing a Hall voltage transverse to the electric current direction when the conductor is subject to an applied magnetic field perpendicular to the electric current. In the case of SHE, accumulation of spins is developed on the lateral direction of the electric current in the absence of magnetic fields. The SHE originates from the SOC that when an electron is orbiting around a positively charged iron, it will experience an electric field that transforms to a relativistic magnetic field in the reference frame of the electron, which in turn interacts with the electron spin and causes them to deflect. In materials with high SOC, when an electric charge current is passing through, mechanisms such as skew scattering [37], [38] or side

jump scattering [39] cause electrons with opposite spins scatter to the opposite directions and thus effectively generate a transverse spin current. For a thin film material with thickness comparable to its spin diffusion length, the top and bottom surface will have spin accumulations with opposite polarizations as a result of the transverse spin current. The process is illustrated in Figure 2-8 (a). The charge and spin currents are related by a unitless parameter θ_{SH} called the spin Hall angle as $J_s = \theta_{SH} \frac{\hbar}{2e} J_c$, where θ_{SH} is typically between 0 and 1 for heavy metals.

Topological insulators, on the other hand, is a special class of materials that has an insulating bulk and conductive surface states hosting spin-polarized currents also as a result of strong SOC [40]. The SOC pushes the valence band above the conduction band, i.e., band inversion. Due to the continuity of the band structure, a massless Dirac fermion forms at the TI surfaces and the currents at the surfaces are spin polarized with the polarization locked to the momentum of the electrons, shown in Figure 2-8(b). Since the surface spin currents of TI are purely spin polarized with the application of a certain direction of electric currents, they are more efficient in sourcing the spin currents compared with the heavy metals, and the corresponding spin Hall angle θ_{SH} can be greater than 1 for TI.

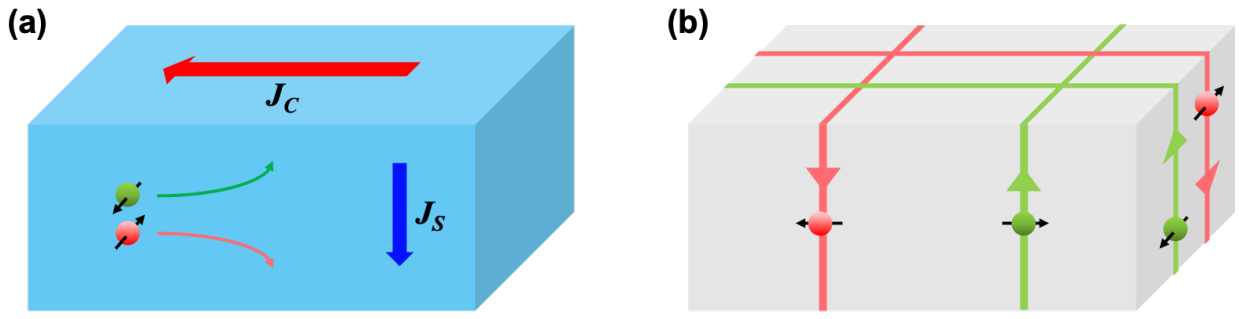

Figure 2-8 Source of spin currents in spintronics. (a) SHE: transverse spin currents are generated when electric charge currents pass through a heavy metal and electrons with oppositely polarized spins scatter to opposite directions. (b) Spin of the surface currents in TI is locked to the momentum of the electrons.

In the heterostructure consisting of a SOC material and a magnetic material, due to the angular momentum conservation, as the spin polarized current generated in the SOC material scatters off the interface, the angular momentum will be transferred to the magnetic material, creating magnons or effectively exert a anti-damping torque [i.e., spin-orbit torque (SOT)] to the magnetic moments. The spin-wave damping compensation (in Chapter 5 and 6) and the spin injection and detection in the non-local spin transport measurement (in Chapter 7 and 8) are based on such effects.

3 Numerical Methods

As discussed in Chapter 2, magnetic dynamics is governed by LLG equation, whose analytical solutions may be obtained under linear approximations for spin waves or spin superfluid in the linear regime. Considering the nonlinear nature of the LLG equation, however, in most general situations, we need to resort to the numerical solutions to investigate magnetic dynamics. In Section 3.1, we shall see in a single domain model how LLG equation can be solved numerically to gain insight of the numerical process and how magnetic dynamics is affected under the application of the spin torque. In Section 3.2 and 3.3, two simulation software solving magnetic dynamics based on LLG equation, LLG Micromagnetic Simulator and MuMax3, will be introduced, respectively. Besides solving LLG equation to gain insight for magnetic dynamics, COMSOL Multiphysics (COMSOL for short) has also been adopted for design and analysis purpose. Examples of using COMSOL to calculate Oersted field distribution around the antenna for spin-wave emission and leakage current will be discussed in Section 3.4. For the numerical methods discussed in this chapter, some numerical process and all numerical results are processed either in Python with NumPy and SciPy or in Matlab.

3.1 Numerically Solving LLG Equation in a Single Domain Model

In this chapter, we will discuss numerically solving LLG equations without introducing any spatial dependent parameters, and thus essentially in a single domain model. We choose the Landau-Lifshitz equation and introduce the spin torque term as follows:

$$\frac{d\boldsymbol{M}}{dt} = -\gamma \boldsymbol{M} \times \boldsymbol{H_{eff}} - \frac{\alpha}{M_s} \boldsymbol{M} \times \left(\boldsymbol{M} \times \boldsymbol{H_{eff}}\right) + \gamma \frac{\hbar \theta_{SH} J_c}{2e M_s^2 t} \boldsymbol{M} \times (\hat{\boldsymbol{\sigma}} \times \boldsymbol{M}) \tag{3.1}$$

The 3rd term on the right hand side of Equation (3.1) corresponds to the spin torque generated from the adjacent spin orbit coupling (SOC) material via spin Hall effect (SHE), where $\hbar$ is the reduced Planck's constant, e is the elementary charge, θ_{SH} is the spin Hall angle, and thus $\frac{\hbar \theta_{SH} J_c}{2e}$ denotes the flow of spin angular momentum, t is the effective thickness of the ferromagnetic layer, and $\hat{\boldsymbol{\sigma}}$ is the direction of the generated spin magnetic moment.

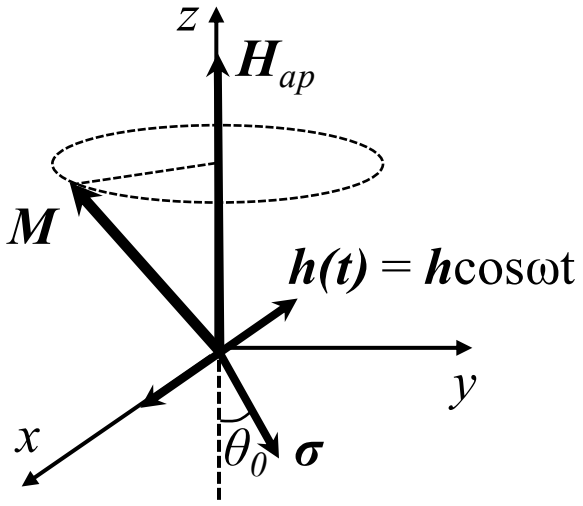

Figure 3-1 Single domain magnetic dynamics in the Cartesian coordinates. The applied magnetic field $\boldsymbol{H_{ap}}$ is along z direction. $\boldsymbol{h(t)} = \boldsymbol{h}cos\omega t$, along the x direction, is the AC Oersted field for the spin-wave excitation induced by

inductive microwave techniques (more details will be discussed in Section 4.1). The spin polarization $\boldsymbol{\sigma}$ is in the yz plane with an angle θ_0 with respect to the $-z$ axis [3], considered for the general case. In such a configuration, the magnetic moment $\boldsymbol{M} = (M_x, M_y, M_z)$ is expected to precess primarily around $\boldsymbol{H_{ap}}$ direction (i.e., z axis).

Considering the magnetic dynamics in the Cartesian coordinates shown in Figure 3-1 and the case of $\boldsymbol{H_{eff}} = \boldsymbol{H_{ap}} + \boldsymbol{h}$, Equation (3.1) can be decomposed into:

$$\dot{m}_x + \alpha m_z \dot{m}_y - \alpha m_y \dot{m}_z = -\omega_0 m_y - \eta \cos\theta_0 m_x m_z - \eta \sin\theta_0 m_x m_y \tag{3.2}$$

$$-\alpha m_z \dot{m}_x + \dot{m}_y + \alpha m_x \dot{m}_z = \omega_0 m_x - \omega_1 \cos\omega t m_z - \eta \cos\theta_0 m_y m_z + \eta \sin\theta_0 (1 - m_y^2) \tag{3.3}$$

$$\alpha m_y \dot{m}_x - \alpha m_x \dot{m}_y + \dot{m}_z = \omega_1 \cos\omega t m_y + \eta \cos\theta_0 (1 - m_z^2) - \eta \sin\theta_0 m_y m_z \tag{3.4}$$

where $m_{x(y,z)} = M_{x(y,z)}/M_s$ is the normalized magnetic moment along x (y, z) direction, $\omega_0 = \gamma H_{ap}$, $\omega_1 = \gamma h$, $\eta = \gamma \frac{\hbar \theta_{SH} J_c}{2eM_s t}$, all have the dimension of angular momentum, and η is proportional to J_c denoting the strength of the spin torque.

By assigning initial values to $m_{x(y,z)}(t = 0)$, Equation Set (3.2)-(3.4) essentially becomes an initial value problem of the ordinary differential equations (OEDs), which is most commonly solved numerically using the Runge-Kutta (RK) method, and in particular, RK5(4), the 4th order RK method with 5th order truncation error [41]. The formalism of the RK method is beyond the scope of this dissertation. For our case, in short, t will be discretized and the current step value of $m_{x(y,z)}(t = t_{n+1})$ will be calculated based on the previous step value $m_{x(y,z)}(t = t_n)$ using the RK5(4) formula. The SciPy ODE solver, *solve_ivp* [with RK5(4) as the default method] [42] or

[3] The angle θ_0 is chosen with respect to the $-z$ axis such that the $\theta_0 = 0°$ situation, corresponding to $\boldsymbol{\sigma}$ aligning along $-z$ direction opposite to $\boldsymbol{H_{ap}}$, results in an antidamping spin torque.

the Matlab ODE solver, *ode45* [43], based on RK5(4), can be used for solving Equation Set (3.2)-(3.4). The results shown in this dissertation are based on *ode45*.

As an example, we present the results calculated for the situation of $\theta_0 = 0°$ and constant $\hat{\boldsymbol{\sigma}}$, i.e., $\hat{\boldsymbol{\sigma}} = -\hat{\boldsymbol{z}}$. This is the case for spin-wave damping compensation in the conventional geometry, which will be discussed in Chapter 5 in a yttrium iron garnet (YIG)/topological insulator (TI) heterostructure. Additionally, the initial condition is set as $\boldsymbol{m}(t = 0) = (0,0,1)$, and $\alpha = 0.1$, $\omega_0 = 2\pi \times 1.2$ GHz , $\omega_1 = \omega_0/300$, corresponding to $H_{ap} = 430$ Oe and $h = 1.4$ Oe , respectively. The time evolutions of m_x and m_y with $J_c = 0$ ($\eta = 0$) are shown in Figure 3-2(a), where the time-average magnetic momenta, $\overline{m}_x$ and $\overline{m}_y$, are 0, indicating that the precession is around z axis, and the amplitudes of m_x and m_y indicate the precession amplitude of magnetic oscillations. Frequency dependent precession amplitude is shown in Figure 3-2(b), where the resonance is at $2\pi f = \omega_0 = \gamma H_{ap}$, the Larmor frequency. It should be noted that by introducing the demagnetization field N$\boldsymbol{M}$ into $\boldsymbol{H_{eff}}$, where N is the diagonal demagnetization tensor [44], will recover the ferromagnetic resonance (FMR) frequency given by the Kittel formula, i.e., $2\pi f = \gamma\sqrt{H_{ap}(H_{ap} + M)}$. At the resonant frequency, we tune the strength of the spin torque by varying η, and plot the dependency of precession amplitudes on spin-torque strength in Figure 3-2(c). It can be seen that the precession amplitude is attenuated for negative η, and amplified for positive η, consistent with the spin torque, $\boldsymbol{\tau_{st}} = \eta \frac{\boldsymbol{M}}{M_s} \times (\hat{\boldsymbol{\sigma}} \times \boldsymbol{M})$, acting as damping and antidamping torque for negative and positive η, respectively.

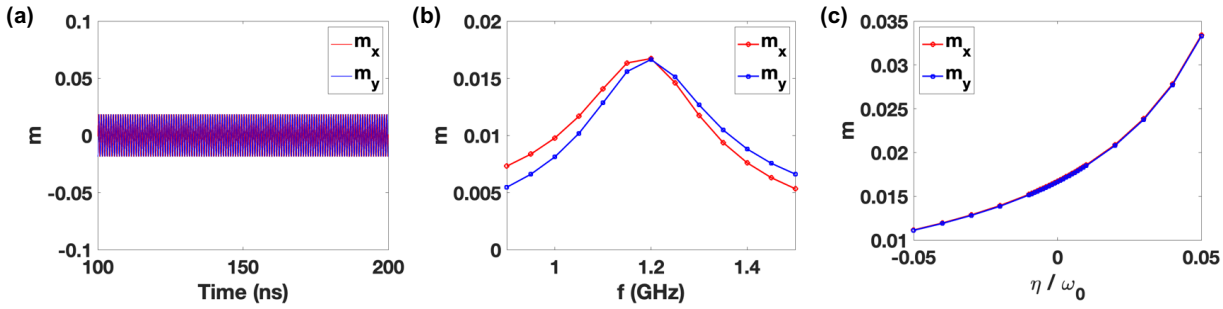

Figure 3-2 Numerical results of Equation Set (3.2)-(3.4) calculated using RK5(4) method with $\theta_0 = 0°$, constant η and $\boldsymbol{m}(t = 0) = (0,0,1)$. (a) Time evolutions of m_x and m_y with $\eta = 0$. The time averaged values indicate the orientation of precession axis and the amplitudes indicate the precession amplitudes of magnetic oscillations. (b) Frequency dependent precession amplitudes at $\eta = 0$. (c) Dependency of precession amplitudes on spin-torque strength (indicated by η normalized by ω_0) at the resonant frequency $f = 1.2\ GHz$.

The numerical solutions based on the simple single domain model can give insight to the antidamping mechanism in magnetic dynamics. Another example of the antidamping magnetic dynamics replacing the time invariant η with an AC η**,** will be discussed in Section 6.

Besides the temporal evolution of the single domain magnetic dynamics, the spatial evolution is of equal importance, especially for investigating propagating spin-wave dynamics. To do so, the spatial discretization will be introduced to mesh the simulation region into small cubes, each treated as a single domain, and then the temporal evolution of the magnetic dynamics will be numerically calculated in the same fashion discussed in this section and collectively for all the spatial grids. We leave the complexity of the spatial discretization and collective calculation process to the simulation software, and we will discuss 2 of the micromagnetic simulation software, LLG Micromagnetics Simulator and MuMax3, in the next 2 sections, respectively.

3.2 LLG Micromagnetics Simulator

LLG Micromagnetics Simulator is a micromagnetic simulation software with a comprehensive graphical user interface (GUI). While its design and implementation details can be found in its manual [45], we will briefly discuss the relevant functionalities, implementations and the simulation procedure.

As mentioned in the previous section, the entire simulation region will be discretized into small single domain cubes, each with a corresponding $\boldsymbol{H_{eff}}$. Different from the simple example of the previous single domain model, $\boldsymbol{H_{eff}}$ will include comprehensive contributions from externally applied magnetic field (i.e., Zeeman term), exchange interaction, magnetic anisotropy, demagnetization, etc, as discussed in Section 2.2. The spin torque term is implemented based on the Slonczewski spin-transfer torque [46].

The simulation procedure is shown in Figure 3-3. Firstly, we define the simulation region and the mesh size. The dimension of the mesh should be small enough to reach convergence but large enough for the continuum approximation of micromagnetics to be valid. As a rule of thumb, the grid dimension should be smaller than the domain wall width, $\sqrt{A/K}$, and the exchange length, $\sqrt{A/M_s^2}$, and for typical ferri- or ferromagnetic materials, such as YIG or CoFeB, a mesh dimension of a few nanometers should be good choices. Based on the specific situation, periodic boundary condition can be properly introduced to reduce the computation cost. Secondly, we define the material parameters and the effective field components, which will in turn determine $\boldsymbol{H_{eff}}$. Optionally, we can introduce the spin torque by setting the current and spin polarization. We then assign the initial condition to $\boldsymbol{m}$, configure the simulation by setting α and the simulation duration time or convergence criterion, etc, and finally start the simulation.

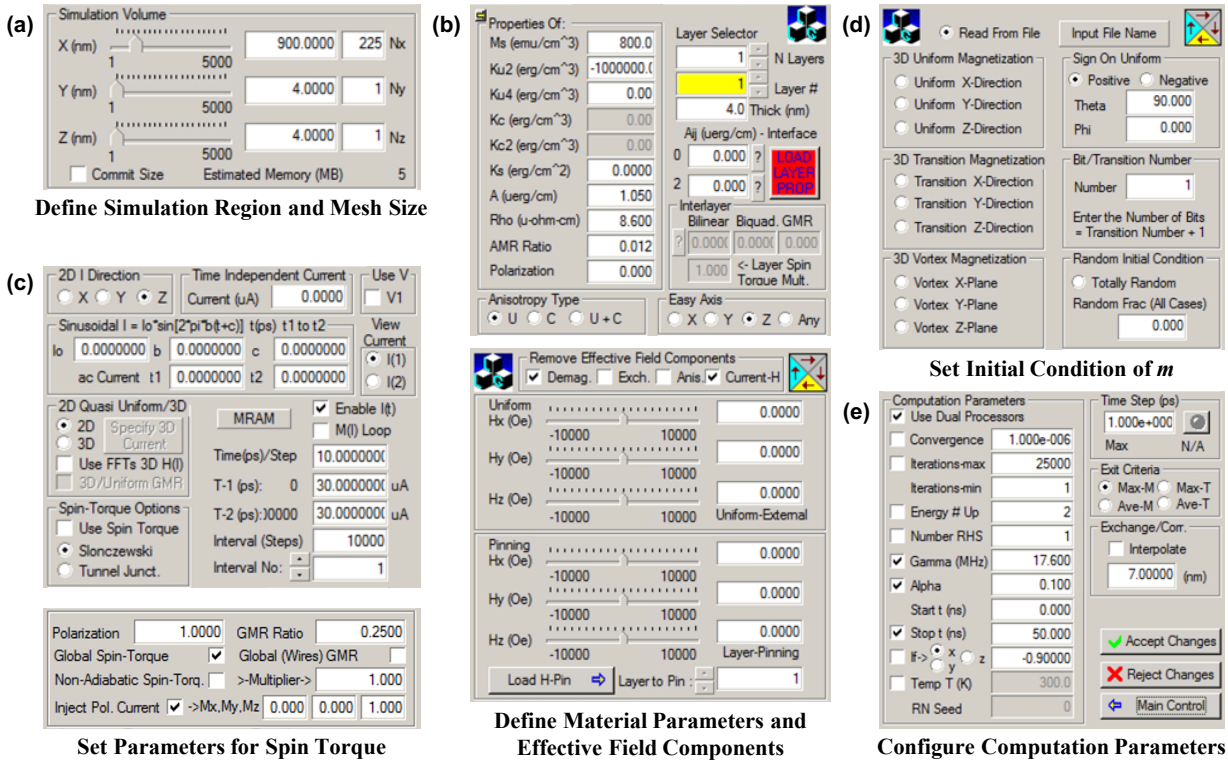

Figure 3-3 Simulation procedure of LLG Micromagnetics Simulator illustrated by screenshots of the GUI configurations. (a) Define the simulation region and mesh size, which should be small enough to reach convergence but large enough for the continuum approximation of micromagnetics to be valid. (b) Define the material parameters and set effective field components. In this example, the demagnetization field and Oersted field are removed. (c) Optionally define the parameters for spin torque (implemented based on Slonczewski spin-transfer torque). (d) Set initial $\boldsymbol{m}(t = 0)$, which can either use the predefined initial condition or take inputs from a file. (e) Configure the computation parameters, in particular, the damping parameter, α, the simulation duration time or the convergence criterion.

As the calculation is in place, the results can be viewed live. After the simulation's done, the results will be saved as files, each contains spatial distribution of $\boldsymbol{m}$ for a specific time instance, based on which physics quantities, such as spin-wave amplitude, superfluid spin current, etc, can be derived for analysis. Optionally, the results can be saved as a movie (*.llg_movie) that can be examined frame-by-frame, which will be useful for understanding the physics process. Shown in Figure 3-4

is an example where we use the movie playback to identify the phase slip event in the magnetic Josephson Junction. We shall discuss the relevant details in Chapter 8, where LLG Micromagnetics Simulator is used for the numerical investigation of electrical control of the superfluid spin transport in a gated easy-plane magnet.

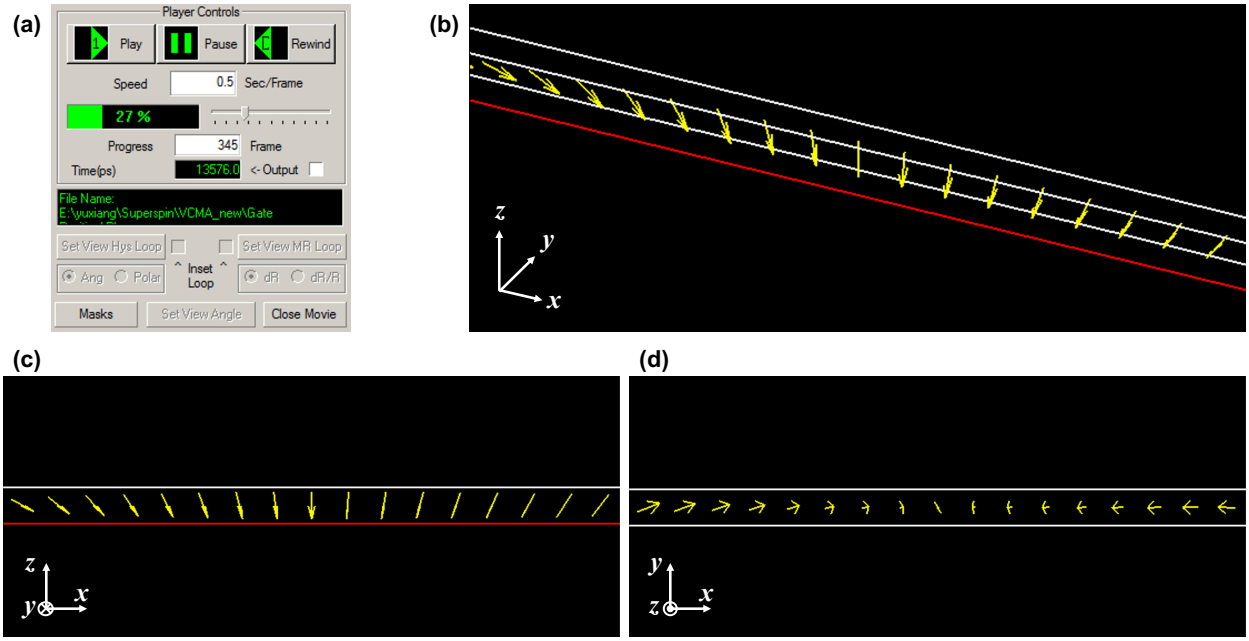

Figure 3-4 An example illustrating the usage of movie (*.llg_movie) in LLG Micromagnetics Simulator to identify the phase slip event in magnetic Josephson Junction. (a) The panel that controls the movie with a by-frame resolution. The frame 345 corresponds to an instance of the phase slip event shown in different perspectives in (b-d). More details will be discussed in Chapter 8.

3.3 MuMax3

MuMax3 is an open-source, GPU-accelerated micromagnetic simulation software [32]. Besides the high performance, in terms of massive computational power supported by GPU and optimized low memory requirement, MuMax3 simulations are configured by scripts (scripting language based on Go [47]) instead of a GUI, and thus provides more flexibilities in the simulations. It has a simple web-based GUI allowing users to inspect and control the simulations, though. Similar to

the previous section, we will only briefly discuss the relevant functionalities, implementations and the simulation procedure, while the design and implementation details can be found in [32], [48], [49].

In addition to the basic externally applied magnetic field (i.e., Zeeman term), demagnetization field, Heisenberg exchange field and magnetic anisotropy field, the Dzyaloshinskii-Moriya exchange (i.e., antisymmetric or noncolinear exchange [50], [51]) field is also supported in MuMax3.

Similarly, spin torque is implemented based on Slonczewski spin-transfer torque [46], [52], transformed to the Landau-Lifshitz formalism based on [32]:

$$\boldsymbol{\tau_{st}} = \beta \frac{\epsilon - \alpha\epsilon'}{1+\alpha^2}\left(\boldsymbol{m} \times (\boldsymbol{m_P} \times \boldsymbol{m})\right) - \beta \frac{\epsilon' - \alpha\epsilon}{1+\alpha^2}\boldsymbol{m} \times \boldsymbol{m_P} \tag{3.5}$$

$$\beta = \gamma \frac{j_z \hbar}{M_s e d} \tag{3.6}$$

$$\epsilon = \frac{P\Lambda^2}{(\Lambda^2+1) + (\Lambda^2-1)(\boldsymbol{m} \cdot \boldsymbol{m_P})} \tag{3.7}$$

where j_z is the electric charge current density along the z axis, d is the free layer thickness, $\boldsymbol{m_P}$ is the magnetization of the fixed layer with P as the spin polarization, Λ is the unitless Slonczewski parameter [4] characterizes the spacer layer and ϵ' is the secondary spin-torque parameter.

The anti-damping torque is configured by setting the parameters such that the coefficient for the field-like torque [i.e., the 2nd term on the right hand side of Equation (3.5)] is 0. In particular, we set $P = 1$, $\Lambda = 1$ and $\epsilon' = \alpha\epsilon = \alpha/2$, and thus $\boldsymbol{\tau_{st}} = \beta \frac{1-\alpha^2/2}{1+\alpha^2}\left(\boldsymbol{m} \times (\boldsymbol{m_P} \times \boldsymbol{m})\right)$.

[4] In MuMax3, the Slonczewski spin-transfer torque is based [52] on transformed to the Landau-Lifshitz formalism. $\Lambda^2 = GR$, where R is the effective resistance of the spin-polarized electrons and G is the conductance.

Similar to the simulation procedure using LLG Micromagnetics Simulator, the simulation procedure for MuMax3 is to 1) define the simulation region and the mesh size, 2) set the material parameters, including the exchange stiffness (A), magnetic anisotropy, damping constant (α), parameters for the Slonczewski torque, etc, 3) define excitations, including externally applied magnetic field ($\boldsymbol{H_{ap}}$), electrical current density ($\boldsymbol{J}$), etc, 4) set initial condition for $\boldsymbol{m}$, 5) schedule outputs and run the simulations. Compared with LLG Micromagnetics Simulator, MuMax3 has much more flexibility in the simulation configuration: for instance, the simulation geometry has the freedom of taking a black/white image input for any customized shape; customized material regions can be defined to independently set material parameters and excitations for each region; output quantities can be selected from a long list of pre-defined quantities and even derived ones; loops can be included in the scripting to run the simulations with varying parameters, etc.

MuMax3 will be used as the numerical tool for the research topic in Chapter 6.

3.4 COMSOL Multiphysics

COMSOL is a multiphysics simulation software, based on finite element analysis. That is, it solves the partial differential equations (PDEs) describing different physics systems (e.g., Maxwell equations, Poisson's equation, etc) by spatial discretization with boundary conditions as the constraints. While COMSOL is a versatile simulation software, in this dissertation, we only use it to calculate the Oersted field generated by rf currents in the antennas so as to design antennas to generate spin waves with specific wavelengths (Chapter 4 and 6) and leakage current in non-local experiments to exclude trivial causes of the observed non-local signal (Chapter 7).

The Magnetic Fields interface [5] under AC/DC is used for Oersted field calculation generated by rf currents in the antennas. Considering in our studies of spin waves, the frequency of rf currents is below 5 GHz, corresponding to electromagnetic wave (EM) wavelength of above 6 cm, and the device dimension is submillimeter, less than 1.7% of the EM wavelength, and thus the lumped-element circuit model is sufficient, where any phase change of rf currents across the conductor can be neglected. Therefore, a 2-dimensional simulation model with uniform electric currents passing through across the input and output conductors along two opposite directions, shown in Figure 3-5(a), calculating magnetic fields around them (i.e., Oersted fields) is sufficiently accurate, which has also been verified separately against results from full simulation model in HFSS. The simulation region is bound with an Infinite Element Domain [6], sufficiently far away from the structure of interest, to effectively extend the simulation region boundary to infinity. More discussions of how the Oersted field distribution calculated from COMSOL simulations related to spin-wave excitations will covered in Section 4.1, and examples of the design of spin-wave devices based on COMSOL calculated Oersted field distribution will be discussed in Chapter 6.

In this dissertation, we will also use COMSOL simulations to calculate leakage current induced non-local voltages in non-local experiments. The relevant interface is the Electric Currents interface [7] under AC/DC. We use a 3-dimensional model to exactly capture the non-local device structure with 3 parallel Pt bars on top of $BiFeO_3$ (BFO) and both ends of each Pt bar are connected to DC contacts (Au), as shown in Figure 3-5(b). An electric current is injected in the middle Pt bar

[5] The Magnetic Fields interface is under the AC/DC>Electromagnetic Fields in COMSOL. It is used to compute magnetic field and induced current distributions in and around structures, such as coils, conductors, and magnets.
[6] The Infinite Element Domain is a feature in COMSOL [53], which can be viewed as a virtual domain surrounding the physical region of interest to stretch the finite-element simulation region in the radical direction effectively to infinity. Since this layer is at the simulation region boundary, far away from the structure of interest, it is not shown in Figure 3-5(a).
[7] The Electric Currents interface is under the AC/DC>Electromagnetic Fields in COMSOL. It is used to compute electric field, current, and potential distributions in conducting media when the skin depth is much larger than the device dimension.

from the input DC contact to the output DC contact in the simulation, and then the electric potentials at the 2 DC contacts connected with the Pt bar on the right can be extracted as V_1 and V_2, based on which the non-local voltage can be calculated as $V_{nl} = V_1 - V_2$. Three Pt-bar structure is adopted to investigate the non-local signals when electric currents are injected from the left and right Pt bars, respectively. More details of the non-local device structure and experiments will be discussed in Section 7.3.

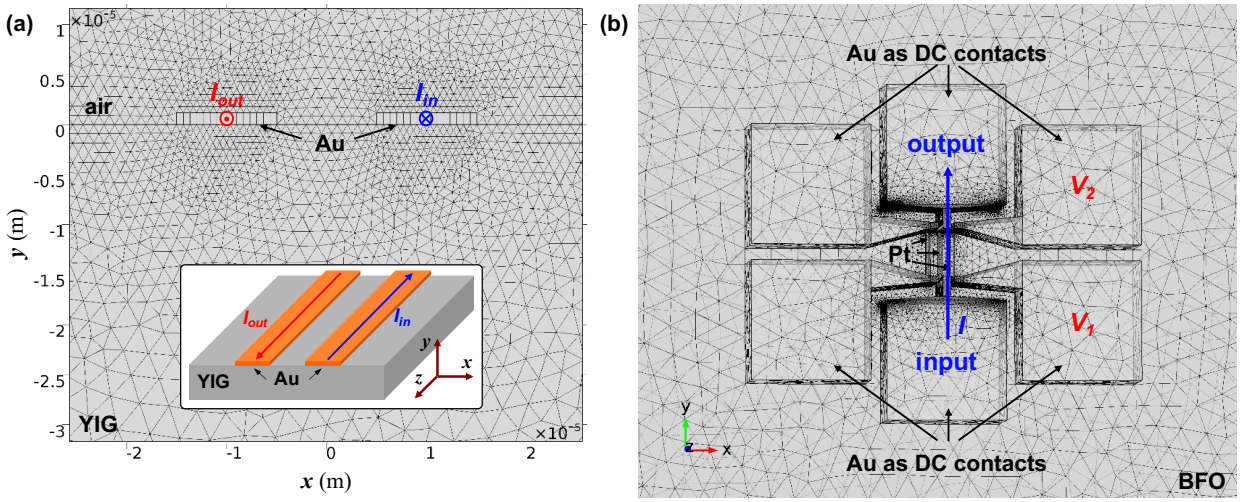

Figure 3-5 Examples of COMSOL simulation models after meshing (i.e., spatial discretization). (a) A 2-dimensional model based on magnetic field interface under AC/DC, where uniform electric currents are driven in the output and input conductors, I_{out} and I_{in}, along two opposite directions, respectively. The inset shows the equivalent schematic 3-dimensional structure for the clarification purpose. The magnetic field distributions around the conductors will be calculated. (b) A 3-dimensional model based on electric currents interface under AC/DC, where 3 parallel Pt bars are on top of BFO, each connected with 2 DC contacts on their ends, and an electric current, I, is driven in the middle Pt bar from the input DC contact to the output DC contact. The non-local voltage is calculated as $V_{nl} = V_1 - V_2$, where V_1 and V_2 are the electric potentials at 2 DC contacts connected to the Pt bar on the right, respectively.

4 Experimental Methods

This chapter will discuss relevant experimental methods with a focus on device characterization techniques to analyze spin-wave dynamics. In Section 4.1, we shall discuss propagating spin-wave spectroscopy (PSWS) as a key technique widely used to characterize spin waves. Typically, PSWS is performed with a vector network analyzer (VNA) for both spin-wave excitation and detection. Alternatively, a signal generator (SG) and an oscilloscope or spectrum analyzer can be used for spin-wave excitation and detection, respectively. In Section 4.2, we will introduce the current-reversal method and delta method as efficient means for measuring small electric signals buried in the thermoelectric voltages (thermoelectric EMFs). This technique is powerful in investigating non-local spin transport in magnetic insulators.

4.1 Propagating Spin-Wave Spectroscopy (PSWS)

PSWS has been used to measure magnetostatic spin waves characteristics since late 1960s [25], [54], [55]. In more recent years, miniaturized version of this technique has been applied to investigate short-wavelength spin waves [56], [57], where important information of spin-wave dispersion spectrum, spin-wave passband and propagation loss can be obtained. A typical device structure for such measurements is shown in Figure 4-1, where two antennas are placed in parallel at a separation on top of the spin-wave medium used for spin-wave excitation and detection, respectively. These two antennas are connected to two ports on VNA, which measures RF power absorption and transmission induced by spin waves in the form of scattering parameters (S-parameters). We shall then discuss in detail how spin waves are excited, detected and examine

some exemplary results to demonstrate fundamental spin-wave properties observed in the experiments.

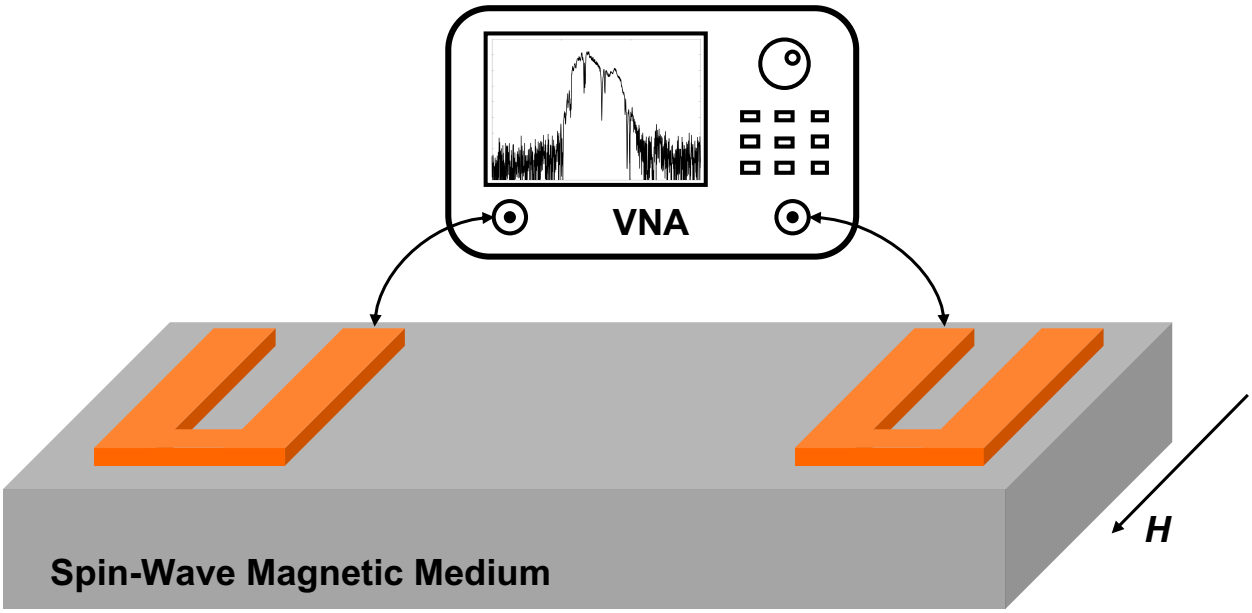

Figure 4-1 Typical PSWS device structure and measurement configuration.

In ferromagnetic resonance (FMR) experiments, in addition to a DC external magnetic field, an AC magnetic field is applied uniformly across the magnetic material to excite the uniform precession mode (FMR mode) that all magnetic moment precesses with the same phase and amplitude, when the FMR condition is met. This FMR mode can be viewed as non-propagating spin waves with zero wavevector k, or equivalently speaking, infinite wavelength λ. To excite spin waves with a finite wavelength, a non-uniform spatial profile of AC magnetic field is necessary, which can be induced by AC current drive in the antennas as the spin-wave injectors. In PSWS measurements, VNA drives RF signal to the antennas, which creates an AC current and a corresponding Oersted field around the antennas (Figure 4-2) to excite spin waves. The Oersted field has a spatial distribution which generates spin waves with wavevectors corresponding to the Fourier transform of the Oersted field's spatial profile [58]. By designing the configuration and

dimensions of antennas, the spin waves with specific wavevectors distribution, i.e., specific wavelengths, will be excited most efficiently.

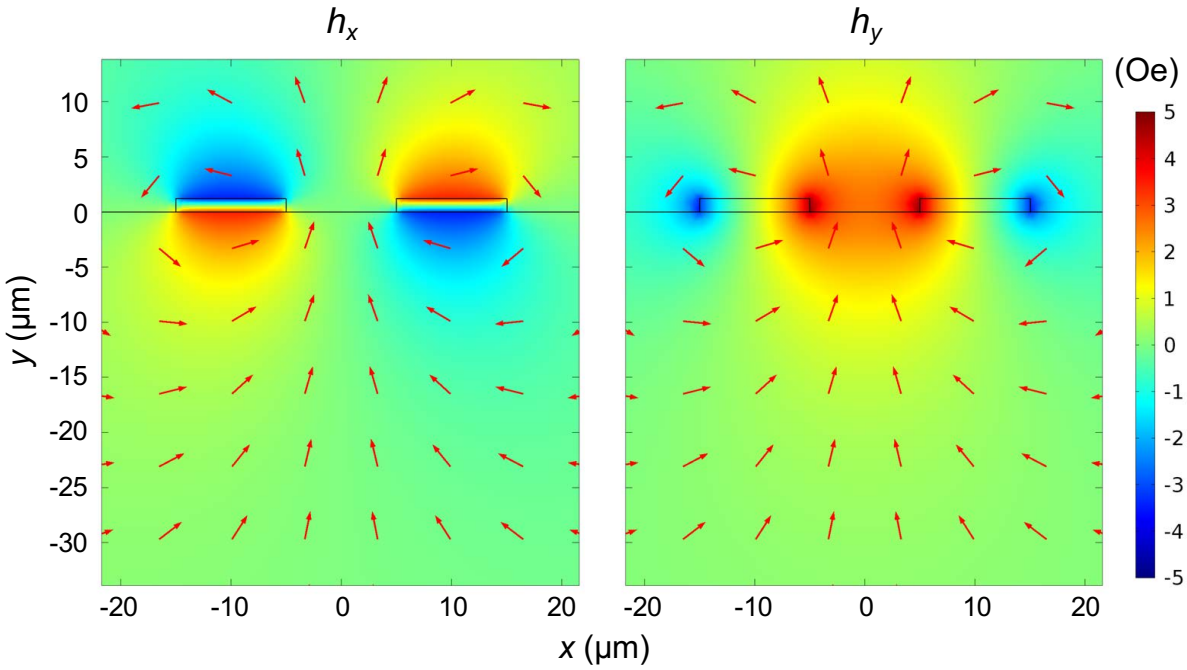

Figure 4-2 Oersted field distribution around a coplanar strip (CPS) line as the antenna, calculated from COMSOL. The area in $y < 0$ corresponds to the magnetic material as spin-wave medium.

We now examine three typical antennas used in spin-wave experiments (shown in Figure 4-3) to illustrate the process of antenna design for spin-wave excitation of a specific k distribution: microstrip (MS) line, coplanar strip (CPS) line, and coplanar waveguide (CPW). For each antenna configuration, we first calculate the Oersted field distribution around the antenna by COMSOL. As discussed in Section 3.4, for spin waves below 10 GHz and submillimeter spin-wave device dimensions in our experiments, a 2-dimensional simulation model with a uniform current distribution in the antenna conductors is sufficiently accurate. The Oersted field spatial distributions are then Fourier transformed to yield k distributions, as shown in Figure 4-3 (g-i).

The spin waves at corresponding k components with higher amplitudes will be excited more efficiently.

In the simulations, the width of the lines of MS, CPS and CPW, and the separation between the lines in CPS and CPW are all set to be 10 μm. As can be seen from Figure 4-3 (g-i), each type of antenna couples most efficiently to a correspondingly specific range of wavevectors. The MS couples efficiently to spin waves with wavevectors up to a cutoff value, or, equivalently speaking, with wavelengths larger than a threshold value. For MS with width $w = 10\ \mu\text{m}$, the cutoff wavevector is 6259 cm^{-1}, which is very close to $\frac{2\pi}{w}$ with a value of 6283 cm^{-1}, and the threshold wavelength is 10.04 μm, which is close to w. The MS is typically used for excitation of wide-band spin waves. Unlike MS, the CPS and CPW couple efficiently to narrower bands of spin waves with a peak wavevector. For CPS and CPW with signal-to-ground central distance $d = 20\ \mu\text{m}$, the peaks are located at wavevectors 1381 cm^{-1}, 1457 cm^{-1}, respectively, which are close to $\frac{\pi}{d}$ with a value of 1571 cm^{-1}. Therefore, CPS and CPW are typically used for excitation of spin waves with finite passband, with the maximum at wavelength around $2d$. Comparing with CPS, CPW has a sharper cutoff at lower wavevectors, due to its additional ground line. A meander type CPW can be formed by introducing multiple repetitions of the CPW signal and ground lines, which can be used to excite spin waves with an extremely narrow range of wavelengths, typically considered as a specific wavelength [57].

Similar to being used as spin-wave injectors, antennas can also be implemented as spin-wave detectors, with electromagnetic induction as the detecting mechanism. Like injecting antennas, the detecting antennas couple most efficiently to specific wavelengths of spin waves, depending on the configuration and dimensions of the antennas as previously discussed. In the typical spin-wave device configuration, the detecting antenna is placed at a distance from the injecting antenna to

detect spin waves after propagating across in the spin-wave medium. The distance determines the direct electromagnetic coupling between the antennas, which is independent from spin-wave dynamics and is considered as the noise floor of the spin-wave device.

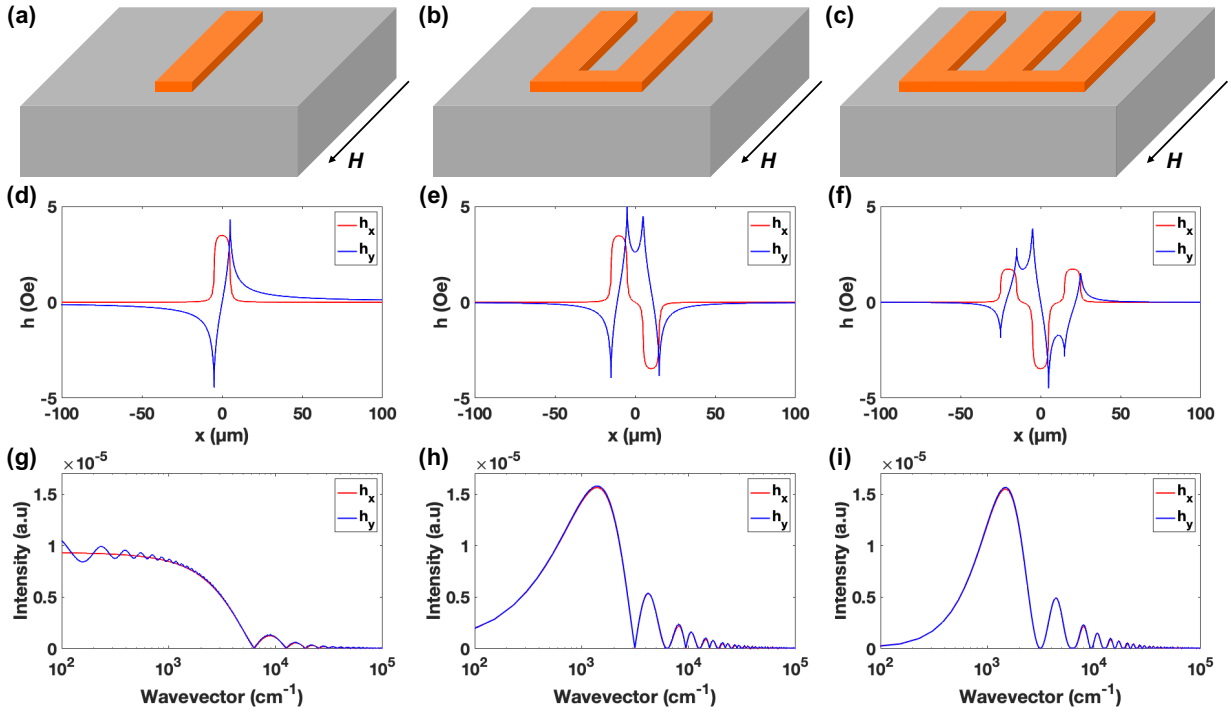

Figure 4-3 Typical antennas used in spin-wave experiments for spin-wave excitation and detection: (a) microstrip (MS) line, (b) coplanar strip (CPS) line, (c) coplanar waveguide (CPW). The spatial distributions of the generated AC Oersted field amplitudes are shown in (d - f), with their corresponding Fourier transform shown in (g - i) as indications of the coupling efficiency of the antennas to spin waves with different wavevectors k. In PSWS measurements, the values of k can be obtained by fitting the streaks feature in S_{11} or S_{22} as a function of frequency f and magnetic field H (Figure 4-4 (a, c)) with spin-wave dispersion relation.

Next, we shall examine the PSWS experimentally measured in the form of S parameters by VNA. Figure 4-4 shows typical S parameters (amplitude) as a function of frequency f and magnetic field H for spin waves excited and detected both with CPS lines placed at 220 μm apart on top of 2.3 μm thick YIG. Figure 4-4 (a) and (c) are S_{11}, S_{22} reflecting the power absorbed at the spin-wave emitting and detecting antenna, when the input power is driven at each of them respectively. The

absorbed powers are used to excite spin waves, and thus excited spin-wave k spectrum can be extracted from S_{11} and S_{22}. To be more specifically, the streaks parallel to the dashed lines marked in the figure correspond to spin waves with specific wavevectors, the values of which can be obtained by fitting with the spin-wave dispersion relation. Figure 4-4 (b) and (d) are S_{21}, S_{12} reflecting the power transmitted from the spin-wave emitting antenna to the spin-wave detecting antenna and vice versa, respectively. S_{21} and S_{12} can be used to obtain spin-wave passband and propagation loss. The position of the spin-wave passband, and correspondingly spin-wave device operation frequencies, can be tuned by the magnetic field, as discussed in Section 2.3. Since the spin-wave emitting and detecting antennas are the same in shape and dimensions, features and amplitudes of S_{11} and S_{22} are identical. However, features and amplitudes of S_{21} and S_{12} are not identical. By examining S_{21} and S_{12} for a fixed magnetic field [i.e., a vertical cross section of the color plots in Figure 4-4 (b, d)], it can be observed that S_{21} is greater than S_{12} in the main spin-wave passband, as shown for 600 Oe in Figure 4-5. This is due to the non-reciprocity of magnetostatic surface spin waves excited inductively by antennas discussed in Section 2.3. On the other hand, spin-wave phase recorded in PSWS by VNA measurements can be used to estimate spin-wave group velocity: $v_g = \frac{\partial \omega}{\partial k} \approx \frac{2\pi\delta f}{2\pi/s} = \delta f s$, where δf is the frequency difference corresponding to a 2π change of the spin-wave phase and s is the spin-wave propagation distance [59]. Figure 4-6 shows the phase of S_{21}, where for 600 Oe at around 3.5 GHz, $\delta f = 0.094\text{GHz}$, and thus can be used to calculate v_g to be 2.068×10^4 m/s.

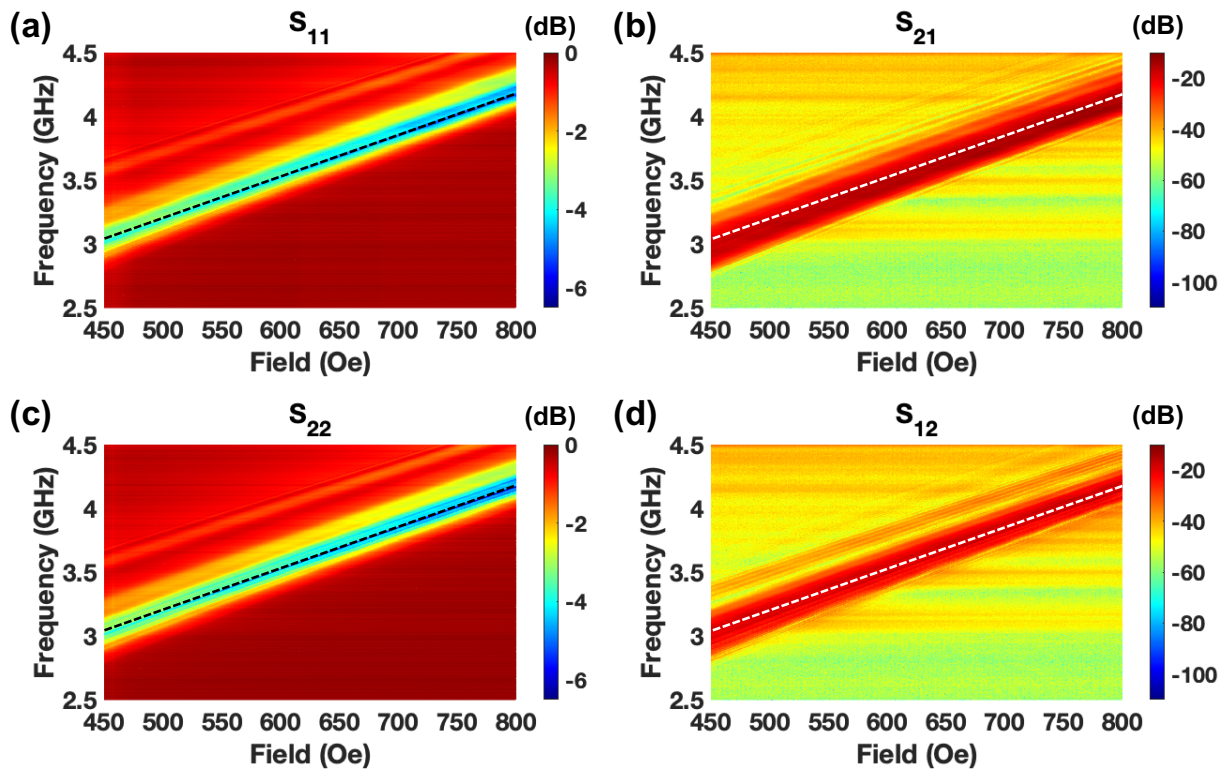

Figure 4-4 Typical S-parameters obtained from PSWS measurements by VNA. Black dashed lines in (a, c) and white dashed lines in (c, d) are artificially added to indicate the spin wave with a specific wave vector. Spin waves are emitted and detected by the identical CPS lines (width: 20 μm, gap: 20 μm) placed at 220 μm apart on top of a 2.3 μm thick YIG.

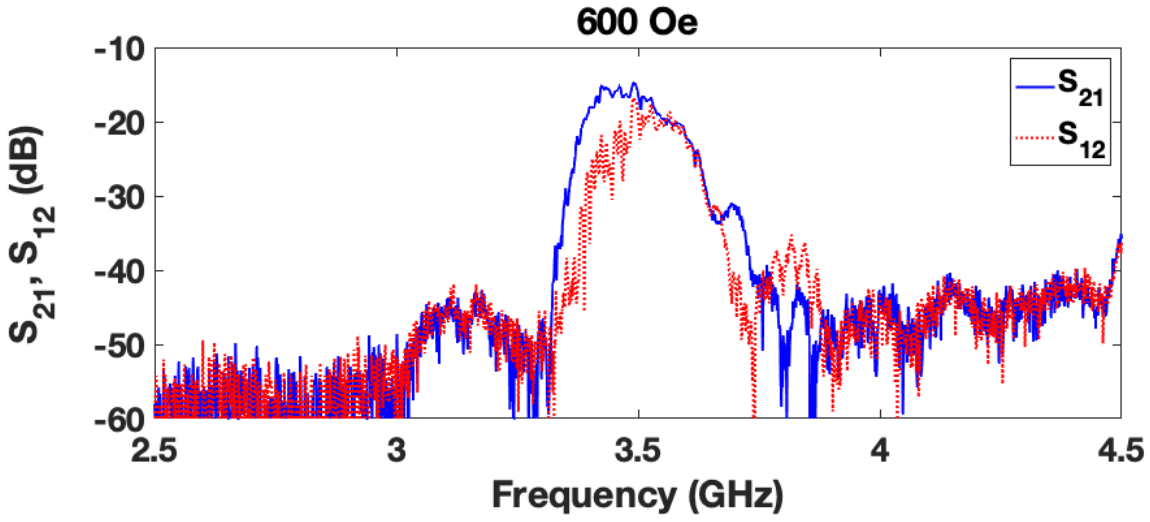

Figure 4-5 S_{21} and S_{12} at 600 Oe, extracted from the results in Figure 4-4 (b, d) by taking vertical cross sections of the color plots.

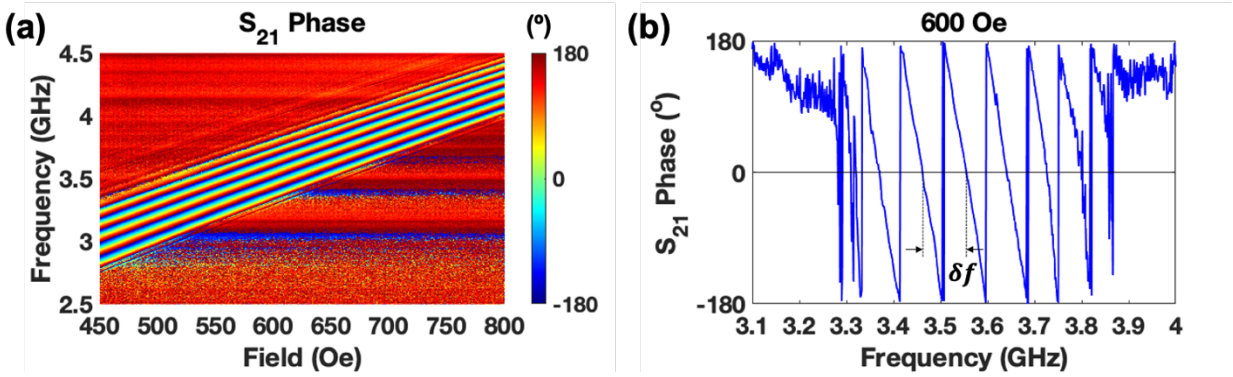

Figure 4-6 Measurements to extract the spin-wave group velocity. (a) Phase of S_{21} by VNA measurements. (b) Phase of S_{21} at 600 Oe by taking a vertical cross section of the color plots in (a). δf corresponding to a 2π (180º) change of spin-wave phase at around 3.5 GHz. In this measurement, the separation between two antennas s is 220 μm, δf is 0.094 GHz, and thus the group velocity can be calculated as $v_g \approx \delta f s = 2.068 \times 10^4$ m/s.

Besides VNA measurements, PSWS can be obtained by using a combination of a signal generator and an oscilloscope connected to the spin-wave emitting and detecting antennas, respectively. By generating CW signals from the signal generator and sweeping the frequencies of the signals, the oscilloscope can be used as a spectrum analyzer such that the response signal amplitude at the input frequency can be obtained from Fourier transform of the time domain signal, as shown in Figure 4-7. The time evolution of the transmitted signal can be captured by the oscilloscope, and thus this method brings in the possibility of measuring spin-wave amplification when the antidamping SOT is generated by a pulse current to reduce the heating effects. In these measurements, for a fixed frequency spin wave, the transmitted signals before and during the application of the pulse current can be used to calculate the gain. Such measurement method will be applied in the studies discussed in Chapter 5.

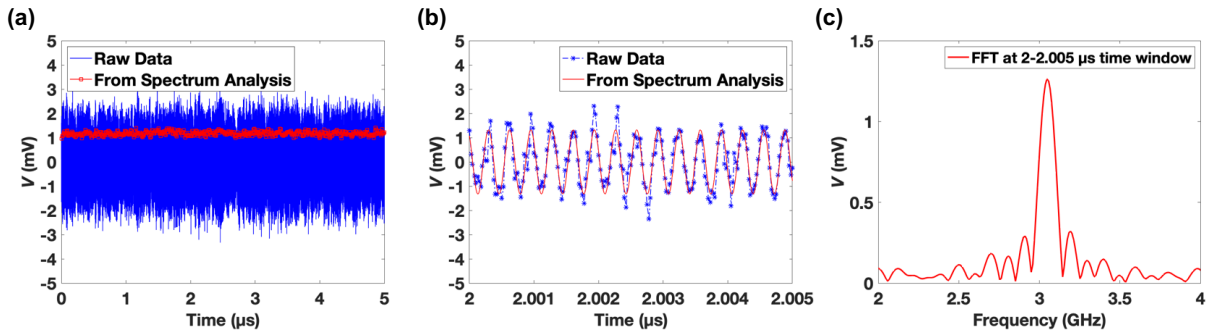

Figure 4-7 Spectrum analysis of the time domain signal to obtain the response signal amplitude at the spin-wave excitation frequency. The results shown in the figures are based on measurements from 2.3 μm YIG, biased at 500 Oe and driven at 3.05 GHz. This spectrum analysis process is necessary especially when the signal is around the noise floor. The raw data of the time domain signal is shown as the blue curve in (a), which is sliced temporally into consecutive time windows, i.e., the 5 μs long time domain signal is sliced into 1000 consecutive time windows, each with a 5 ns duration. (b) is an example of one such 5 ns time window, where the blue curve corresponds to the raw signal extracted from that within 2 – 2.005 μs from (a). Fast Fourier transform (FFT) is then conducted for the raw signal in each time window, as shown in (c) for FFT of the 2 – 2.005 μs time window, from which the maximum frequency component is obtained as the signal amplitude for that specific time window. The frequency of the maximum component is equal to the spin-wave excitation frequency, as expected. The results from the spectrum analysis are then plotted as red curves in (a, b) - the time evolution of the signal is plotted as the red curve in (b); the amplitude of the signal is plotted as the red curve in (a).

4.2 Current-Reversal Method and Delta Method

In this section, we will briefly discuss experimental techniques for low level measurements (e.g., voltage or resistance) when measured signals are buried in thermoelectric EMFs. More detailed descriptions can be found in [60].

Measurements errors may result from offset signals (DC) and noise sources (AC). Even though measurement errors are ubiquitous, they typically can be easily reduced or separated, especially when measuring large signals. For low level measurements, however, the measurement errors can

be tricky to reduce or separate even with careful experimental setups, and they can corrupt the desired signals. Thermoelectric voltages, or thermoelectric EMFs, are the most common sources of errors in low level measurements. Thermoelectric EMFs result from Seebeck effect, and are generated in the testing circuits at the presence of a temperature gradient and especially when two different materials A and B are joined to form connections in the form of $V_{EMF} = S_{AB}\Delta T_{AB}$, where S_{AB} is the Seebeck coefficient at the connection and ΔT_{AB} is the temperature difference between A and B. As an example, copper, typically used as the center conductor for coaxial cables, when pairing with copper, silver, gold, has Seebeck coefficients ≤ 0.2 μV/°C, 0.3 μV/°C, 0.3 μV/°C, respectively. If any part of the circuits has oxidizations, however, the Seebeck coefficient can increase by orders of magnitudes. Junction by copper and copper oxide has a Seebeck coefficient as high as ~ 1000 μV/°C, which in the presence of slight temperature fluctuations leading to ΔT_{AB} even as low as 0.001 °C will result in $V_{EMF} \approx 1$ μV, making sub-μV voltages indetectable. Figure 4-8 shows an example of the impact of thermoelectric EMFs on the measured signal. The voltage readings were taken with a constant supply of 10 mA currents for an extended period of time. Even though fluctuations due to thermoelectric EMF are ~0.1-0.2 μV, for a short duration of 1 s, the change of voltage readings is smaller than 10 nV.

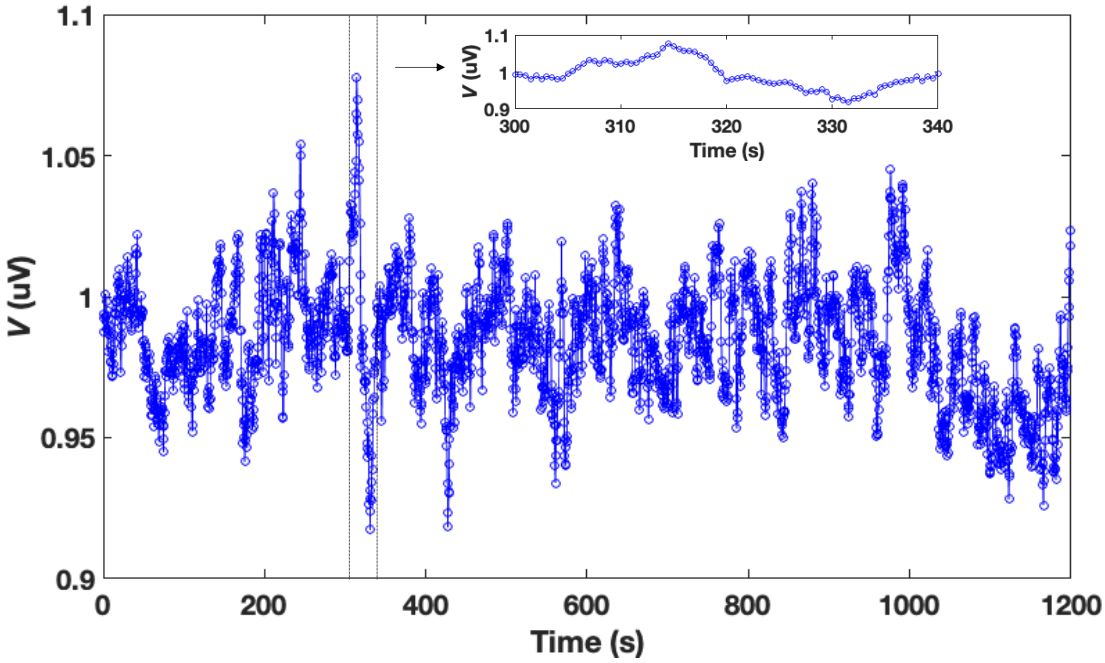

Figure 4-8 Example of the impact of thermoelectric EMFs on the measured signal. The measurement has been carefully set up to isolate from common sources of errors, such as rf and heat. The voltages are measured at a constant driven current of 10 mA in the test circuit. Inset shows the results in a focused time window from 300 s to 340 s, where even though there exists ~0.2 μV fluctuations in the voltages, the change of voltage readings for 1 s time window is smaller than 10 nV.

In experiments, reducing temperature gradients and using same materials for the conductors can help minimize thermoelectric EMFs. In situations when device under test (DUT) is in low temperature chambers and testing instruments are in the ambient air, or when conductors are in DUT on-chip, however, other techniques are necessary to reduce the impact from thermoelectric EMFs. One effective method is by reversing the source polarity to cancel thermoelectric EMFs. When the measured voltages result from the application of the electrical currents, the measurements essentially become resistance measurements, local or non-local depending on the measurement circuits. The idea of reversing the source polarity to cancel thermoelectric EMFs leads to the current-reversal method and the delta method for these low resistance measurements.

Current-reversal method is conducted with a bipolar current source and a nanovoltmeter so that voltages can be measured at positive and negative current polarities as $V_{M+} = V_{EMF+} + V_{DUT}(+I)$ and $V_{M-} = V_{EMF-} + V_{DUT}(-I)$, respectively. $V_{DUT}(\pm I)$ corresponds to the voltage drops at DUT when positive or negative current polarity is applied. If the current polarity is switched fast and each voltage measurement is taken in fast response to the application of a certain polarity of current, V_{EMF+} and V_{EMF-} are close to each other. By "fast", we mean that the time scale is shorter than the thermal time constant. Under this condition, V_{EMF} manifests as a constant offset and thus can be canceled out, leaving $V_{DUT}(+I) - V_{DUT}(-I) = V_{M+} - V_{M-}$. This way, odd-order terms of I in V_{DUT} can be extracted, where the 1st order term is:

$$IR = (V_{M+} - V_{M-})/2 \tag{4.1}$$

with R being local or non-local resistance depending on the test circuits. It should be noted that the 2nd order term ($\propto I^2$) results from thermal effects as well.

An improved version of the current-reversal method takes into the consideration that in a small time scale, any change in the measured signal of the system can be approximated linearly, as shown in Figure 4-9. In this scenario, three consecutive voltage measurements can be taken for changing current polarities as $V_{M1} = V_{EMF1} + V_{DUT}(+I)$, $V_{M2} = V_{EMF2} + V_{DUT}(-I)$ and $V_{M3} = V_{EMF3} + V_{DUT}(+I)$, where $V_{EMF2} = V_{EMF1} + \delta V$ and $V_{EMF3} = V_{EMF2} + \delta V$. Similarly, the 1st order term of I can be worked out as:

$$IR = (V_{M1} + V_{M3} - 2V_{M2})/4 \tag{4.2}$$

This measurement method is called delta method, and each data point is the moving average of the three voltage readings, as in Equation (4.2). The current-reversal can be viewed as a 2-point delta method.

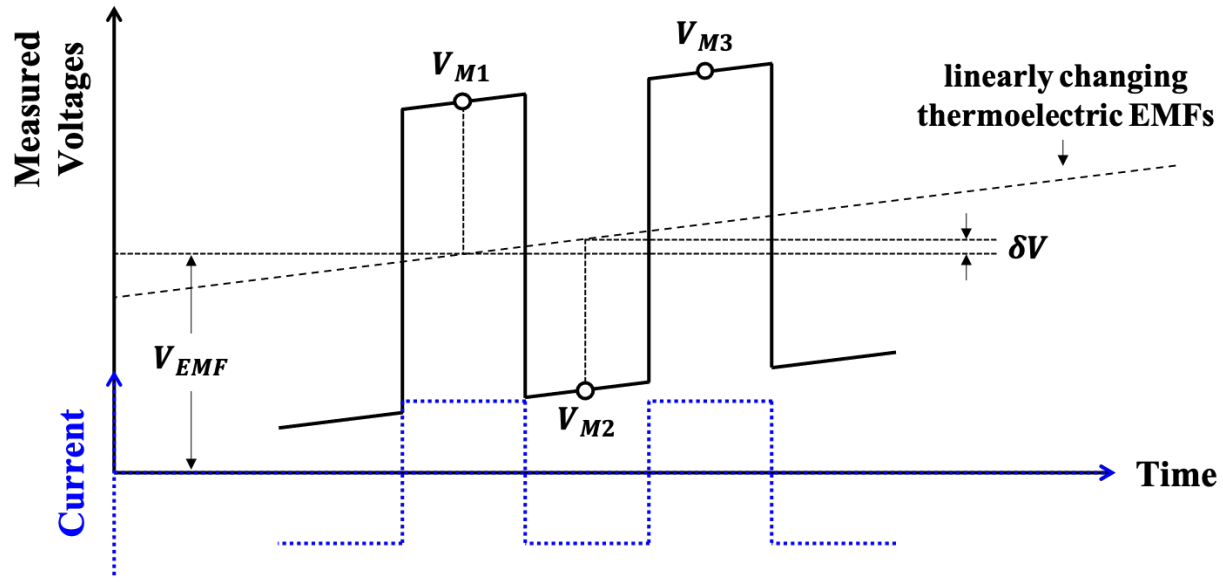

Figure 4-9 Illustration of cancellation of thermoelectric EMFs with a bipolar current source and nanovoltmeter. Two consecutive voltage readings (e.g., V_{M1} and V_{M2}) will be used as the moving average in the current-reversal (i.e., 2-point delta) method and three consecutive voltage readings (e.g., V_{M1}, V_{M2} and V_{M3}) will be used as the moving average in the delta method.

In measurements, Keithley 2182A can be used as the nanovoltmeter, which can be synced with fast switching bipolar current sources such as Keithley 6221 or Keithley 2400 to provide the fast response speed required. The current-reversal method or delta method has been implemented for measuring low level resistances such as non-local magnetoresistance in non-local spin transport experiments [61]. We also apply these methods in studying the non-local spin transport in magnetic insulators, which will be discussed in detail in Chapter 7.

5 Spin-Wave Damping Reduction with Pulsed DC Current in Topological Insulators

In this and the following chapter, we will present the study on spin-wave damping compensation based on SOT for coherent spin waves excited inductively by microwave antennas in insulating Yttrium Iron Garnet (YIG). Planar YIG films can be integrated with silicon technology to realize devices such as tunable filters, frequency selective limiters, and signal-to-noise enhancer. However, such films suffer from spin-wave damping which limits their use in such applications. In this chapter, we show that spin currents in topological insulators (TIs) can be used to reduce spin-wave damping. TI supports surface spin currents, potentially making it an efficient source of anti-damping torque. We show that in a YIG/Bi_2Se_3 bilayer, the spin-wave damping rate can be reduced by 60% at a current density of 8×10^5 A/cm^2. Furthermore, we show that the damping reduction has a strong dependence on spin-wave frequency, and we demonstrate that this dependence arises from nonlinear magnons scattering.

5.1 Introduction

As introduced in Chapter 1, spin waves are coherent oscillations of spin in magnetic materials and have been used in tunable radio frequency (rf) filters that are based on Yttrium Iron Garnet (YIG) [62]–[65]. Spin waves have also been used for frequency selective limiters, signal-to-noise enhancers, phase shifters, as well as logic operations [63], [66]–[68]. However, damping remains a key factor in rf electronics that are based on thin YIG films. For practical rf applications where

power handling is critical, thick YIG films (>1 μm) grown using liquid phase epitaxy (LPE) are preferred. A great deal of effort has been put into growing thick YIG films of ultralow damping [69], [70], yet a finite amount of damping in these films still hinders practical spin-wave applications. One method to compensate the spin-wave damping is to transfer angular momentum of spin-polarized electrons to spin waves [14]–[16], [71]–[73] as discussed previously. In these spin-wave devices, the spin current is typically generated through Spin Hall Effect (SHE) (see Section 2.5) in heavy metals such as Pt or W. In spin-wave devices based on YIG, spin orbit torque (SOT) takes place at the surface, based on which several groups have achieved a reduction of spin-wave damping rate in pulsed laser deposition (PLD)- [16], [71] and LPE-grown [14], [15], [74] YIG, using spin currents from Pt.

Here, we utilize a topological insulator (TI) layer on a 2.3 μm thick LPE-grown YIG to reduce the damping rate of magnetostatic surface spin waves (MSSW) with the device shown in Figure 5-1(a). TI is a special class of material where, in accord with the time-reversal symmetry (TRS), the spins of the Dirac-like surface states are locked to their momentum [75]–[82]. As discussed in Section 2.5, TI can potentially be more efficient in providing the antidamping torque, and thus be more efficient in reducing spin-wave damping compared with conventional heavy metals. In our experiments, we choose Bi_2Se_3 as the TI material, with a thickness of 15 nm to avoid the electronic hybridization between the two surfaces. Although there have been several studies on SOT in TI and FM metal layers [83]–[86], there have been fewer studies that have demonstrated interface effects in a YIG/TI system [87], [88]. This could be mostly due to the challenges of growing a high-quality TI layer on a YIG substrate.

5.2 Experimental Details

An optical image of the device showing the dimensions is shown in Figure 5-1(a). The antennas are shaped in a ground-signal-type CPW (i.e., CPS) where both ground (G) and signal (S) lines, as well as the gap between them, have a width of 20 μm. The gap between the antennas and the gold metal contacts (L_g) and the width of the gold contacts (L_c) are both 40 μm. The length of the TI layer (L_{TI}) is 60 μm and its width is 320 μm.

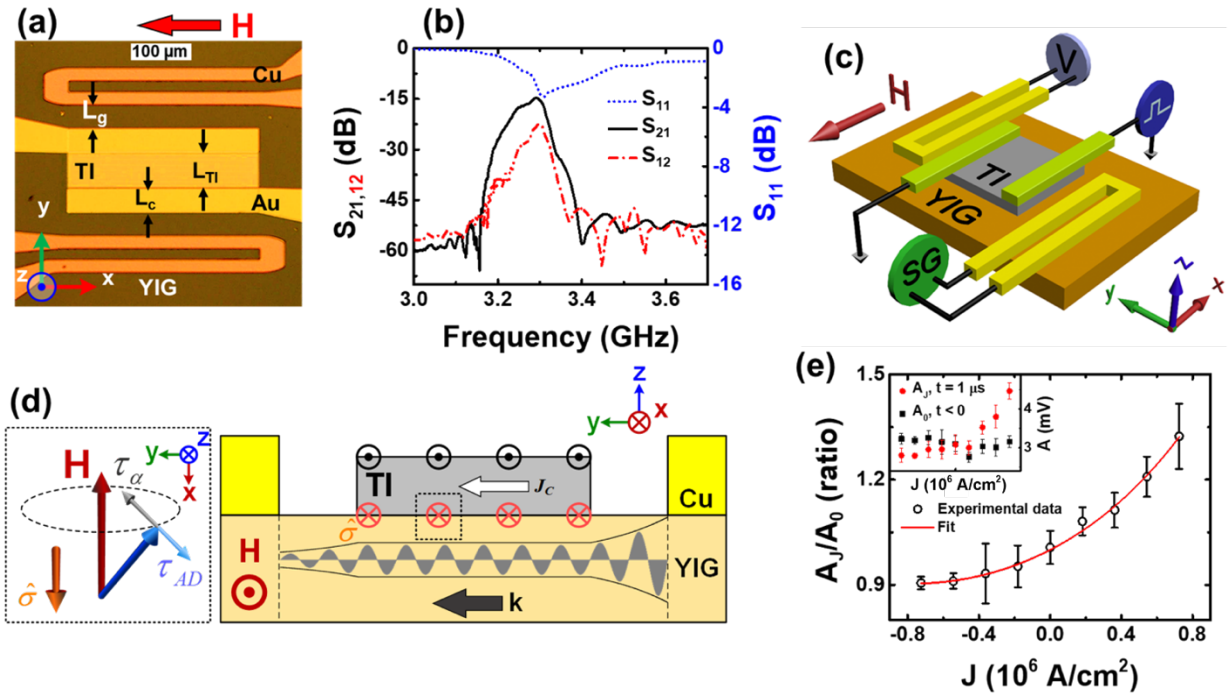

Figure 5-1 Amplification of spin waves. (a) Optical image of the spin-wave device. (b) S parameters of the spin-wave device measured using a VNA. (c) A signal generator (SG) launches a spin wave while a current pulse drives a spin-polarized current in the TI that enhances the spin-wave signal. (d) The spin currents from TI (with spin polarization $\hat{\sigma}$) transfer the angular momentum of the spin to the spin wave with wavenumber k. Damping is compensated at a critical current density, J_C. (e) Spin-wave amplitude controlled by spin currents from TI measured at 500 Oe and 3.38 GHz. The data is fitted (red solid line) using Equation (5.2) (Inset: amplitude of the spin wave before and after the current pulse is applied).

Figure 5-1(b) shows the Scattering (S-) parameters of the device obtained using a Vector Network Analyzer (VNA) with the magnetic field oriented along the $-x$ direction and set to 500 Oe. The S_{11} parameter, which is observed to be the same as the S_{22} parameter, is shown with the dotted blue line and it is indicative of the power absorbed by the YIG. The S_{21} is shown with the solid black line and indicates the transmitted power. In our measurements, due to the geometry of our device, we observe both volume spin waves and surface spin waves, also known as Damon-Eshbach (DE) modes [89]. The S_{12} (red dot-dashed line) shows a higher insertion loss because of the nonreciprocity of surface spin waves [90]–[92].

Next, we drive a current through the TI layer as spin waves with a frequency of 3.38 GHz at H = 500 Oe are continuously excited using a Signal Generator (SG) with an output power of 4 dBm. Figure 5-1(c) shows the schematic of the measurement setup. The amplitude of the propagating spin wave is measured using an oscilloscope, which we also use as a spectrum analyzer [93]. We use a 1-μs current pulse with a repetition period of 50 ms to reduce the Joule heating. The Oersted field generated by the conductive TI layer is calculated to be between 1 to 2 Oe at the highest current densities, which causes an insignificant change in the resonant frequency. Figure 5-1(d) illustrates the concept of using TI for transferring the angular momentum from spin currents to spin waves in YIG. As spin waves propagate and decay due to the damping torque (τ_α), for a given direction of current, the antidamping torque (τ_{AD}) caused by the spin currents (with spin polarization $\hat{\sigma}$) acts on the magnetization, preventing the spin-wave amplitude from further decay until it reaches the other end of the TI layer. When a current of the opposite direction is driven in TI, the spin polarization of the generated spin currents is reversed and thus the SOT from the TI further attenuates the spin-wave amplitude. The results are shown in Figure 5-1(e). The gain is defined as the ratio of the spin-wave amplitude when a 1-μs current pulse is applied, A_J, over the

amplitude before the current pulse is applied, A_0. Figure 5-1(e) shows gain for positive currents of up to 32% for a current density of 8×10^5 A/cm^2 and an attenuation of nearly 90% for negative currents of the same magnitude. The measured amplitudes of the spin wave before and after the current pulse are shown in the inset in Figure 5-1(e) using the black square and red circle markers, respectively. To analyze the gain of the spin-wave amplitude, we adopt the method used by E. Padrón-Hernández et al. [15], [74] where the amplitude is expressed as [8]:

$$A(J) = A_J e^{-i\omega t} = c_k(0) e^{-i\omega t} e^{-(\alpha_k - \eta_k J - \zeta_k \nabla T)t} \tag{5.1}$$

where $c_k(0)$ is the initial spin-wave amplitude with wavenumber k, ω is the spin-wave angular frequency, α_k is the spin-wave damping rate, η_k is the parameter related to SOT, and J is the current density that is driven through the TI layer. ζ_k is the parameter proportional to the Spin Seebeck Effect (SSE) and ∇T is the longitudinal temperature gradient across the film [74] and is proportional to J^2, which is considered to be small in our experiment since the pulse duration and duty cycle are very low. The gain G can be determined by:

$$G(J) = \frac{A(J)}{A(0)} = e^{a(J/J_C + \nabla T/\nabla T_C)} \tag{5.2}$$

where the prefactor a is equal to $\alpha_k L_{TI}/v_g$ with v_g being the group velocity. J_C is the critical current density and equal to α_k/η_k. Based on this formulation, J_C is essentially an extrapolated parameter and it is the current density at which the damping of the spin waves is entirely compensated [15], [16], [74], [85], [95]–[99]. Similarly, ∇T_C is also an extrapolated parameter, equal to α_k/ζ_k, and is defined as the temperature gradient at which the damping is compensated [74]. It should be noted that since there are gaps between the two antennas and the TI contacts that

[8] In this dissertation, we consistently use α for damping constant and η for coefficient in SOT, different from the notations in [74], [94].

are equal to $2 \times (L_g + L_c)$, the spin current from the TI does not exert any torque on the spin waves within these gaps [see Figure 5-1 (a) and (d)]. Even if we use current densities equal to be J_C, there will still be losses in this gap that we could not compensate for due to our device geometry. The losses under the gold contacts regions are even more significant because of the changes in the surface conductance and boundary conditions [92], [100]. To be able to estimate J_C, the group velocity needs to be determined, which requires an accurate estimation of the wavenumber k at the operating frequency. We will return to evaluating J_C later in this chapter.

We repeat the measurements done in Figure 5-1(e) for frequencies ranging from 3.15 GHz to around 3.4 GHz. Figure 5-2(a) shows the spin-wave spectrum when no current is applied to the TI layer, that is, J = 0. In Figure 5-2(b), we show examples of the gain obtained at different frequencies. The figure clearly shows that the gain at the highest current density changes with frequency. To further illustrate this frequency dependence, we plot the maximum gain in dB obtained at the extreme current density values, $\pm 8\times10^5$ A/cm^2, vs frequency in Figure 5-2(c). The red curve with the upward triangle data points shows the gain for $+8\times10^5$ A/cm^2 and the blue curve with the downward triangle data points shows the gain for -8×10^5 A/cm^2. At frequencies close to 3.38 GHz, we observe a peak in the gain. The total gain is attributed to two components, one is due to SOT, the other due to SSE, which is an even function with respect to the current. To separate the SOT and the SSE contributions in the gain, we fit the data points in Figure 5-2(b) for all frequencies to the exponential term in the gain equation [Equation (5.2)]. We remove the $a\nabla T/\nabla T_C$ term in the exponent that is proportional to J^2, which corresponds to Joule heating that results in SSE, and only plot the gain in dB that is linearly dependent on J in Figure 5-2(d); we call this component of the gain $Gain_{odd}$. $Gain_{odd}$ is maximized at 3.38 GHz, roughly 100 MHz above the

frequency of maximum spin-wave transmission (for $J = 0$), and the gain is almost zero elsewhere within the pass band.

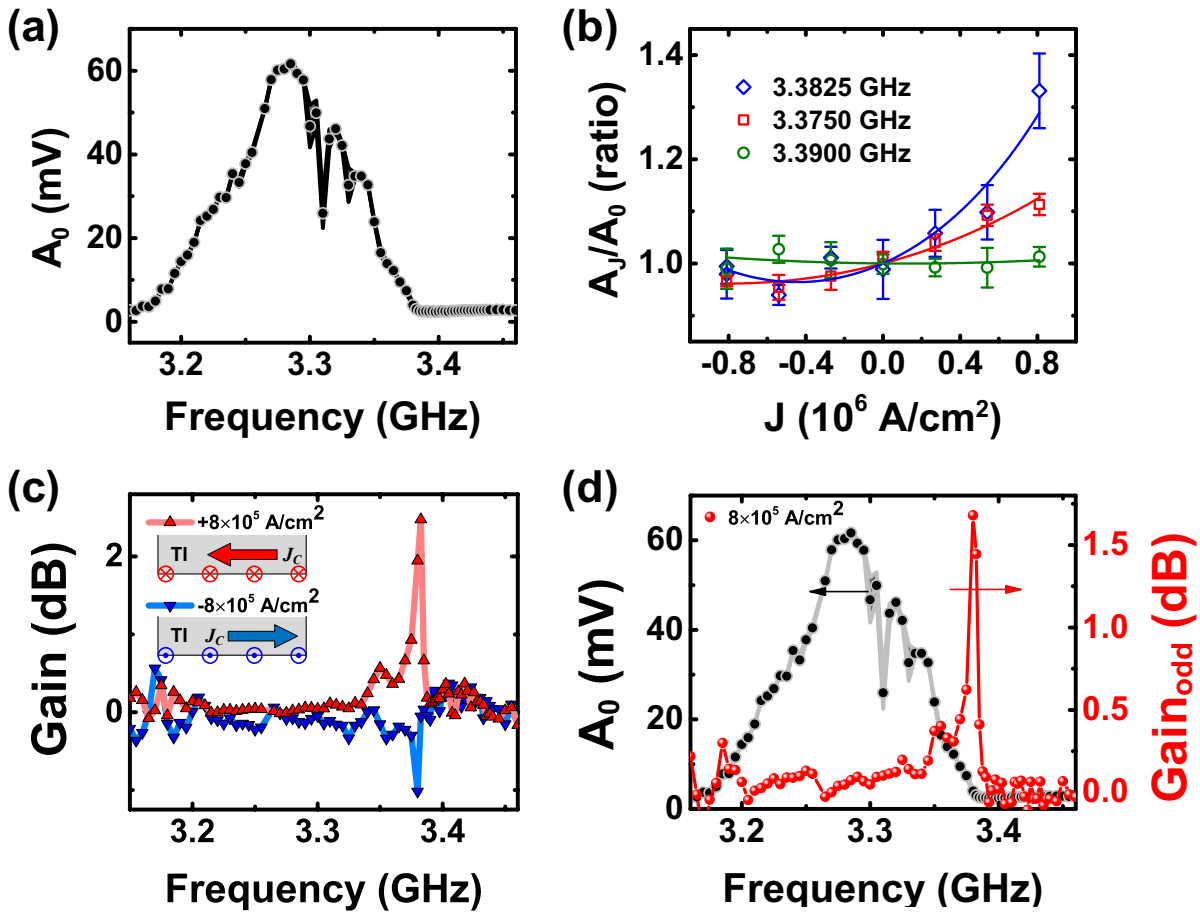

Figure 5-2 Dependence of the gain on spin-wave frequency. (a) Spin-wave amplitude measured using an oscilloscope/spectrum analyzer with the external magnetic field set to 500 Oe. (b) Different spin-wave frequencies show different amounts of gain. The markers show experimental data and the solid lines are the fits to Equation (5.2). (c) The dependence of the total gain on spin-wave frequency is illustrated by plotting the maximum total gain in dB. The figure shows that the gain is more significant for a narrow range of frequencies above the maximum transmission frequency. (d) The gain due to SOT vs the spin-wave pass band for $J = 8 \times 10^5\ A/cm^2$.

The details of the spin-wave transmission and the strong frequency dependence of the gain curves are discussed next.

5.3 Results and Discussion

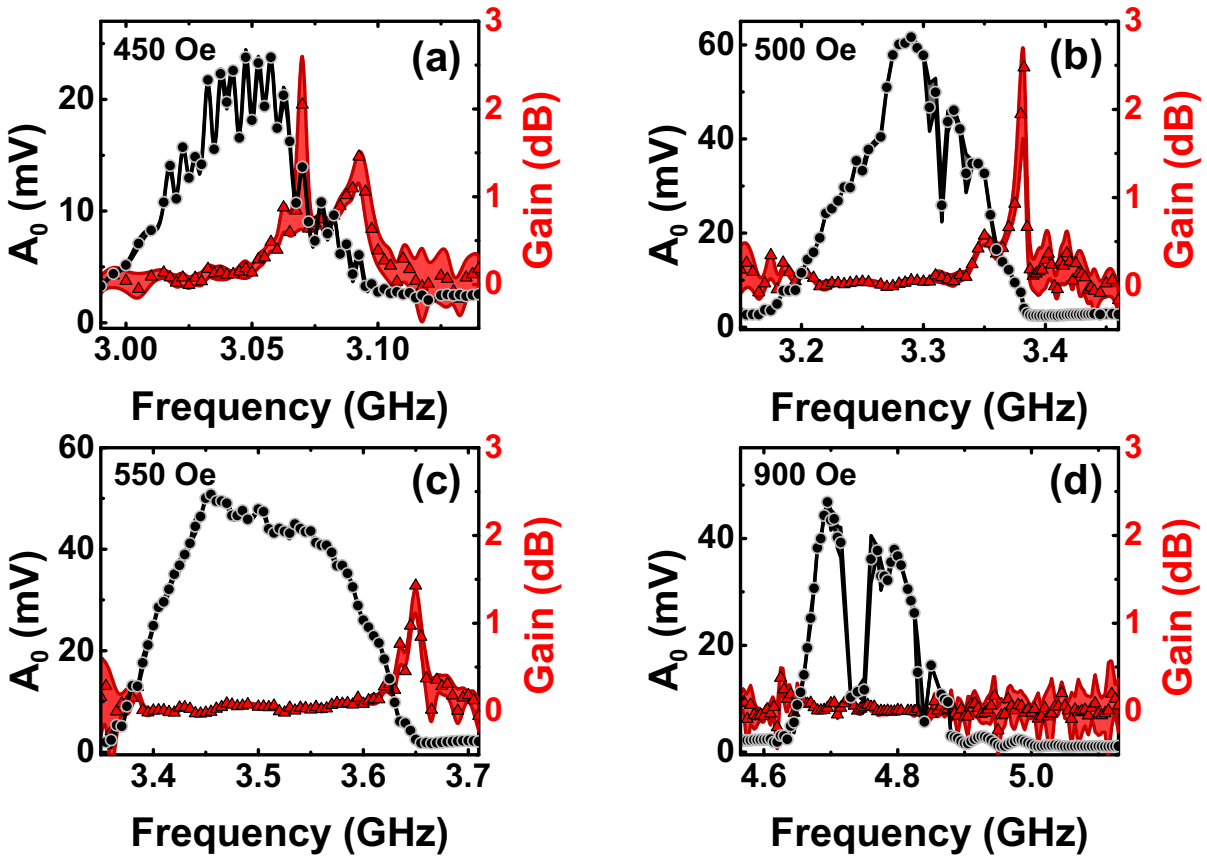

Figure 5-3 Dependence of the gain enhancement on external magnetic field. Spin-wave pass band spectrum (black circles) and total gain of spin-wave amplitude in dB (red triangles) with a current density of 8×10^5 A/cm^2 at (a) 450 Oe, (b) 500 Oe, (c) 550 Oe, and (d) 900 Oe. The data shown in (b) is the same as that in Figure 5-2 (a) and (c) (red upward triangles) for comparison. The total gain has a peak at some frequency above the maximum transmission frequency (a-c), whereas the total gain in (d) does not show any enhancement even for frequencies 400 MHz above the maximum transmission frequency due to the absence of three-magnon scattering process.

In Figure 5-3, we plot the total gain that is measured for H = 450, 500, 550, and 900 Oe. We see that in the cases of 450, 500, and 550 Oe, the gain is maximized for a narrow frequency range above the center of the pass band, while in the case of 900 Oe, no significant gain is observed even at frequencies 400 MHz above the maximum transmission frequency. We note that the frequency

differences between the peak of maximum transmission and maximum gains we observe are different for the three magnetic fields, which shows that neither an Oersted field nor a field-like torque is the reason behind the shift in frequency. To understand the dependence of gain on spin-wave frequency and the external magnetic field, we use the VNA to perform the PSWS (as discussed in Section 4.1) to obtain the S_{21} parameter for magnetic fields ranging from 400 to 600 Oe with steps of 2 Oe, as shown in Figure 5-4(a). The color scale represents the magnitude of the S_{21} parameter in dB. Therefore, a vertical cut of this color plot, such as the one along the solid black line at 500 Oe, is a single measurement by the VNA shown in Figure 5-1(b). One main feature in this figure is the red triangle that starts at 450 Oe and around 3 GHz. This region of the plot is indicative of high spin-wave transmission. Another set of features are the streaks that are parallel to the white dashed lines. These streaks are spin waves with unique wavenumbers that couple most efficiently to the antennas [101]. Therefore, by fitting the dispersion relation to these lines and using the thickness of YIG and an estimate value of M_S from superconducting quantum interference device (SQUID) magnetometry, we can find the wavenumbers of the spin waves corresponding to the lines, and thus we obtain the wavenumbers for each individual frequency at a given magnetic field. Using the wavenumber, we can determine the group velocities and the critical current densities.

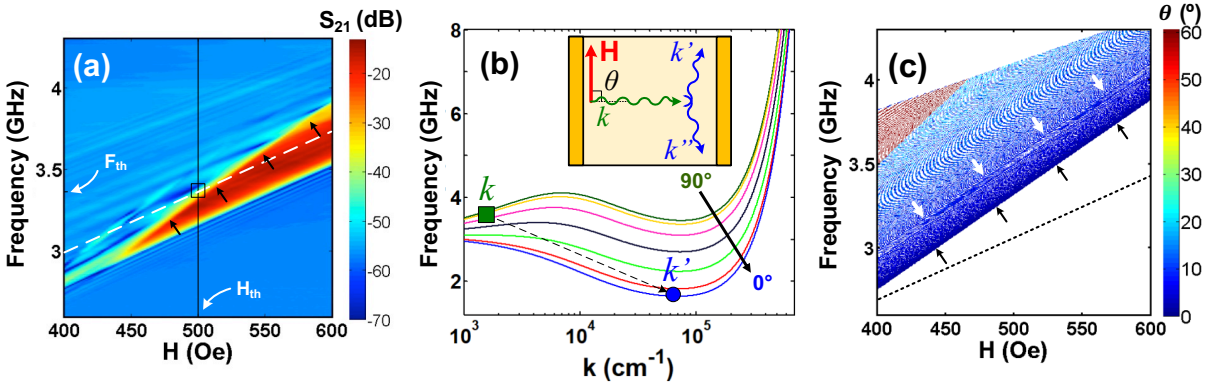

Figure 5-4 Three-magnon scattering in YIG. (a) Experimental data showing the S_{21} parameter for 500 Oe. The white dashed line is a spin wave with a wavenumber that crosses $F_{th} \approx 3.38$ GHz. The four black arrows highlight a line that separates the linear and nonlinear regimes. For the spin wave with wavenumber corresponding to the white dashed line, beyond the magnetic field H_{th} at 500 Oe (solid black square), three-magnon scattering is suppressed and spin-wave transmission increases. (b) The calculated dispersion curves based on Equation (2.27) for spin waves propagating at angles ranging from 0° to 90° with respect to H. The inset shows the scenario when a spin wave propagating at 90° (green rectangle) scatters to two other spin waves (blue circle). (c) Analytical calculation based on the dispersion relation for frequency and magnetic field values at which three-magnon scattering occurs. The transition boundary marked with the four black arrows and is at the same location as the boundary marked with the four black arrows in (a). In the region where three-magnon scattering occurs, the spin-wave transmission measured in (a) is low.

As mentioned above, the red triangular feature in Figure 5-4(a) represents high-spin-wave transmission. For a spin wave of a unique wavenumber, such as the one represented with the white dashed line, the spin-wave transmission increases once a threshold magnetic field and frequency, H_{th} and F_{th} [9], respectively, are reached, in this case 500 Oe and about 3.38 GHz. This threshold magnetic field increases for higher wavenumbers and it always lies along the line marked with the four black arrows. This behavior allows for the assumption that three-magnon scattering [102]–[106] is being suppressed above the threshold field, thus enhancing the spin-wave transmission. This can be understood using Figure 5-4(b), which shows the dispersion curves calculated based on Equation (2.27) [10] for spin waves excited at 500 Oe and propagating at angles θ ranging from just above 0° to 90° with respect to the external magnetic field H. For spin waves that are excited at a frequency and a wavenumber represented with the green square, they propagate at 90° at low but finite k values. For such spin waves with frequency f, there exist states at wavenumber k' with

[9] The threshold magnetic field, H_{th}, is defined such that at a fixed frequency for $H > H_{th}$, the three-magnon scattering is suppressed. Similary, the threshold frequency, F_{th}, is defined such that at a fixed magnetic field for $f < F_{th}$, the three-magnon scattering is suppressed.

[10] Similar to Figure 2-6, here we set $n = 0$ in Equation (2.27), i.e., $k = k_{\parallel}$, no thickness mode considered.

a frequency of approximately $f/2$ (blue circle) to which they can scatter. For the energy and momentum to be conserved [11], the spin wave also scatters to another state also with a frequency close to $f/2$ with a negative wavenumber k", not shown in Figure 5-4(b), where $\vec{k} = \overrightarrow{k'} + \overrightarrow{k"}$. In the scenario shown in Figure 5-4(b), the only states the spin waves can scatter to are the ones at the very bottom of the dispersion curve of spin waves propagating almost parallel to the magnetic field. For magnetic fields higher than H_{th}, this scattering process is suppressed since there will be a frequency offset in all the curves along the positive frequency direction and the condition for energy conservation can no longer be satisfied. Since three-magnon scattering is a nonlinear process, it can be identified by comparing the measured insertion losses at different input powers. The power dependence of the S_{21} parameter is shown in Figure 5-5, where the red triangular feature recovers into the normal trapezoidal shape with lower VNA input powers as a result of the lower magnon population and accordingly reduced scattering possibility. To further confirm that this feature stems from three-magnon scattering, we use the dispersion relation to estimate the frequencies and magnetic fields at which three-magnon scattering occurs [Figure 5-4(c)]. Based on these results, we can conclude that the line marked by the four black arrows is the boundary between linear and nonlinear dynamics. It should be noted that the gain curves we observe in Figure 5-2(d) and Figure 5-3 are not artifacts caused by the Oersted field, which may shift the entire spin-wave spectrum. Near the three-magnon boundary, this effect may shift the spin waves from a low transmission nonlinear regime to a high transmission linear regime. If this were the case, one would observe a pair of gain peaks with opposite polarities on both sides of the maximum

[11] Since the magnon energy is $\hbar\omega$ with $\omega = 2\pi f$, the energy conservation leads to $f = f' + f"$, where f and $f'(f")$ are the frequencies of the incoming magnon and the 2 outgoing magnons in the three-magnon scattering process. Similarly, since the (linear) momentum of the magnon is $\hbar\vec{k}$, the momentum conservation leads to $\vec{k} = \overrightarrow{k'} + \overrightarrow{k"}$, where $\vec{k}$ and $\overrightarrow{k'}(\overrightarrow{k"})$ are the wavevectors of the incoming magnon and the 2 outgoing magnons in the three-magnon scattering process.

transmission frequency, which are not present in our experiments. Additionally, the Oersted field induced spin-wave spectrum shift is estimated to be below 5 MHz, which is much narrower than the gain peak. This again rules out the Oersted field as the cause for our observed gain curve. Same results are also observed in devices with different geometries.

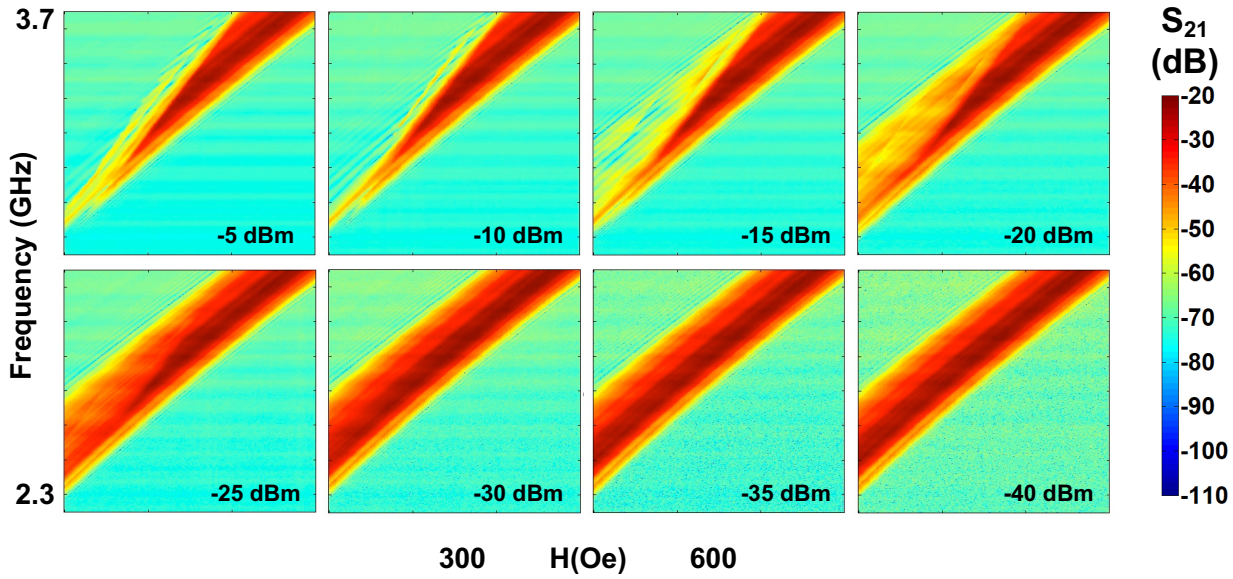

Figure 5-5 S_{21} parameter of spin waves in YIG for different VNA input powers. The data is for magnetic fields ranging from 300 Oe to 600 Oe (left to right for each subplot) and 2.3 to 3.7 GHz (bottom to top for each subplot). The figures show that at low input powers, the red triangular feature that we observe at -5 dBm recovers into a normal trapezoidal high spin-wave transmission region [as in Figure 4-4 (b)]. This indicates that this particular feature, where the normal trapezoidal high spin-wave transmission region is cut into a triangular shape at higher VNA input powers, is a result of the three-magnon scattering, which increases with higher spin-wave excitation powers.

The important finding of this study is that the maximum gain measured at different magnetic fields occurred at their corresponding F_{th} and on the boundary between linear and nonlinear dynamics. Thus, three-magnon scattering is the reason behind the frequency dependence of the gain. This hypothesis is supported by the input power dependent gain [Figure 5-6], where the maximum gain occurring on the boundary between the linear and nonlinear regimes reduces at decreasing input

powers and becomes negligible at low input powers with suppressed three-magnon scattering. While a quantitative analysis of the three-magnon scattering contribution to enhanced gain is beyond the scope of this study, we present a qualitative explanation of the three-magnon scattering enhanced gain. Spin waves at a frequency F_{th} scatter to a very small phase space located at the bottom of the approximately 0° propagation angle dispersion curve in Figure 5-4(b). A high population of low-energy magnons induced by the SOT can suppress and ultimately even reverse the three-magnon scattering process that drains the low k modes. Such a reversal is expected at the onset of the SOT-induced condensation of magnons at the dispersion minima. The tendency of a pumped magnon gas to condense at the finite-momentum dispersion minima has been previously established in the case of parametric pumping [107]–[109].

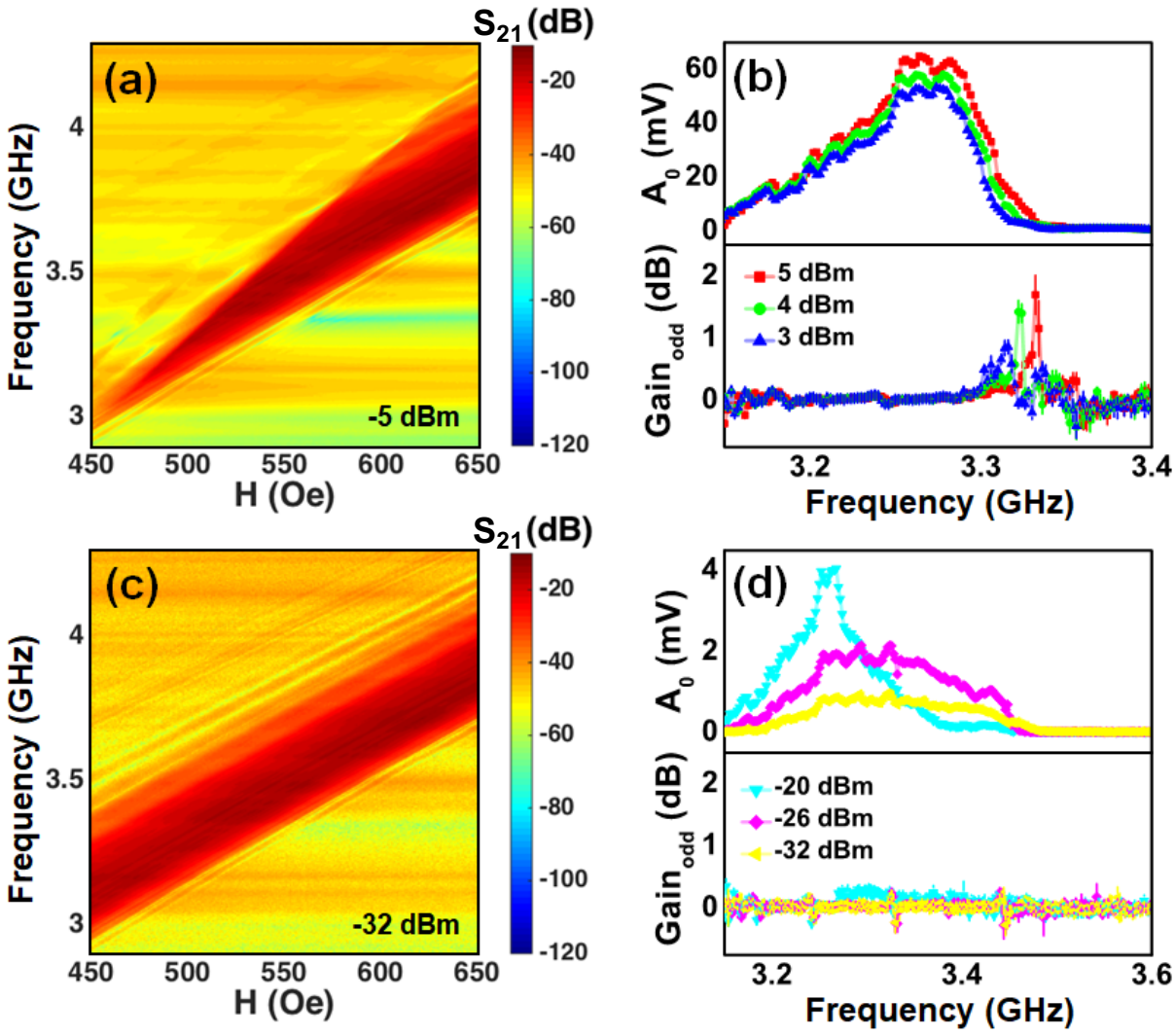

Figure 5-6 S_{21} parameter of spinwaves in YIG at (a) -5 dBm and (c) -32 dBm. (b) (d) The gain due to SOT (i.e., $Gain_{odd}$, the gain after separating the SSE contributions) vs the spin-wave passband measured at 490 Oe for different input powers. The slight shift of the maximum gain frequency aligns with the shift of the spin-wave stopband edge, the boundary between the linear and nonlinear regime in (b).

Finally, we determine the critical current density, J_C, for the three magnetic fields where we measure maximum gain. As mentioned before, we use the parallel streaks in Figure 5-4(a) and the dispersion relation to determine the wavenumber at the frequencies showing maximum gain as accurately as possible. The results are shown in Figure 5-7, where we also show a critical current

density of 1.19×10^6 A/cm^2 at 450 Oe with a 60% reduction in the damping rate, $\Delta\alpha$, at a current density of 8×10^5 A/cm^2. By taking the effect of the TI metal contacts on the dispersion relationship into account [34] we calculate J_C to be 1.5×10^6 A/cm^2. This is smaller than that observed in YIG/Pt bilayer [15], which is just above 2.16×10^6 A/cm^2 at 89 Oe, and is much smaller than values measured in micrometer-wide YIG films deposited using pulsed laser deposition (PLD) [71]. The results also indicate that the SOT process becomes less efficient at higher fields and more current is required to overcome the damping. This field dependent SOT efficiency can be understood as the following: the three-magnon scattering decreases with higher fields (for the same spin-wave excitation power)[12], which in turn lowers the SOT efficiency in reducing spin-wave damping.

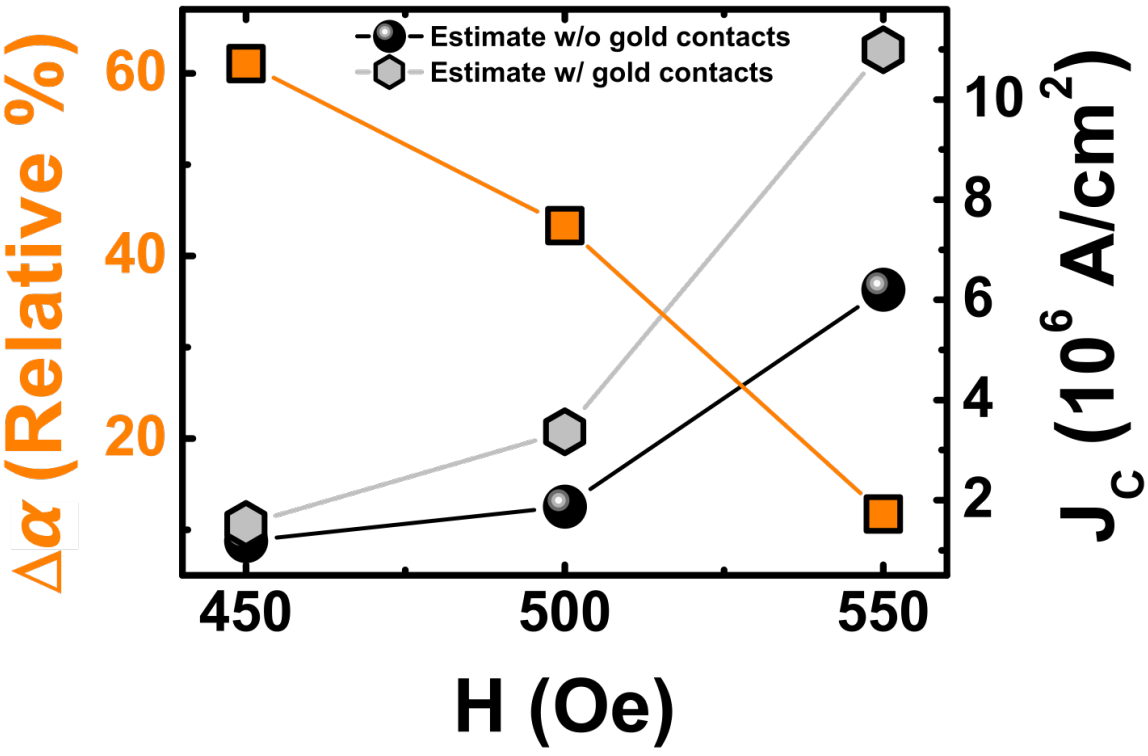

[12] For the same spin-wave excitation power, the precession cone angle of spin waves reduces with higher magnetic fields. Equivalently speaking, the total number of magnons reduces with higher magnetic fields. The nonlinear three-magnon scattering process is thus suppressed as a result of the reduced total number of magnons.

Figure 5-7 The change in spin-wave damping rate, $\Delta\alpha$ (orange squares) and critical current density, J_C (black circles), for different external magnetic fields. At 450 Oe, the control of spin-wave damping rate is the most efficient where at 8×10^5 A/cm^2 60% of the damping rate is reduced. This is also shown in the critical current density data where the value of J_C is lowest at 450 Oe. The gray hexagonal markers are the critical current densities when group velocities are recalculated by taking into account the effect of the metal lines on the dispersion relationship. This increases J_C at 450 Oe to 1.5×10^6 A/cm^2.

5.4 Conclusions

We demonstrate the reduction of spin-wave damping in YIG using spin currents from an adjacent TI layer. The spin-wave amplitude is amplified by 32% and by isolating the contribution of SSE, a gain due to SOT of 1.7 dB equivalent to a 21% gain in amplitude is achieved. Even if Bi_2Se_3 has a semiconducting bulk and thus the spin currents may have bulk contributions, the overall gain from both surface and bulk states is still higher than the 5% achieved in PLD YIG at the same current densities [71]. Due to three-magnon scattering, the frequency at which this peak gain is observed is above the pass band. The results indicate that the combined effect of the SOT and the three-magnon scattering process leads to an efficient mechanism, which reduces spin-wave damping. In order to achieve gain at the center frequency with the least amount of insertion loss, physical considerations such as three-magnon scattering and device geometry need to be considered and optimized. By uncovering these physical contributions and demonstrating the first YIG/TI system for control of spin-wave damping, this work paves the way for the utility of TI-produced SOT on magnetic insulators.

6 Spin-Wave Amplification with Phase-Matched Spin-Orbit Torque Waves

In the previous chapter, we discuss spin-wave damping reduction in the conventional configuration, that is DC currents are used to generate the spin polarization antiparallel to the spin-wave precession axis and the corresponding antidamping torque. The gain, however, is maximized at the edge of the spin-wave passband where the transmitted spin-wave amplitude is small. To enhance the spin-wave amplification efficiency, in this chapter, we propose to rotate the spin polarization perpendicular to the spin-wave precession axis and to synchronize it with the spin waves temporally and spatially. This way, a SOT wave is created with an enhanced antidamping SOT amplitude. We demonstrate via micromagnetics simulations and experiments, in the spin-wave device with a "comb" structure generating the SOT wave, when the SOT wave and the spin waves are phase-matched, the spin wave with a specific wavevector corresponding to the periodicity in the "comb" can be optimally amplified. The amplification is more efficient compared with that based on the conventional configuration. Our proposed device can find application as a tunable spin-wave filter with built-in amplification.

6.1 Introduction

As discussed in Chapter 1 and Chapter 5, spin-wave damping reduction has been previously achieved in magnetostatic spin waves (MSWs) with the Damon-Eshbach (DE) configuration by interfacing the spin-wave medium, such as Yttrium Iron Garnet (YIG), with high spin-orbit

coupling (SOC) materials, such as 5d transition metals Pt [94], [110], [111] and topological insulators [112], where the spin-orbit torque (SOT) is generated to reduce the spin-wave damping in YIG. A gain of <1 dB was obtained from microwave measurements amid the main spin-wave passband where spin-wave amplitude is relatively large [110]. A large amplification seems to be obtained from Brillouin light scattering measurement at an extremely high current density (3×10^7 A/cm^2) in thin (20 nm) YIG [111] with limited power handling capability. Our prior work, as discussed in Chapter 5, shows a 1.7 dB gain due to SOT in the nonlinear regime. No spin-wave amplifier with a reasonable gain has yet been achieved in the main spin-wave passband.

In these structures, a DC charge current is applied in the SOC material parallel to the spin-wave propagation direction, $\boldsymbol{k}$, to generate spin magnetic moment $\boldsymbol{\sigma}$ along the same direction as the precession axis set by the internal magnetic field $\boldsymbol{H}$ as shown in Figure 6-1(a). The SOT, τ, has a strength proportional to $m_\perp$, where $\boldsymbol{m}_\perp$ (or $\boldsymbol{m}_{xz}$) is the projection of the precessing magnetic moment $\boldsymbol{m}$ in the plane perpendicular to the precession y axis (shown in Figure 6-1(b)). The $\boldsymbol{\tau}$ is small when the precessing angle θ, and correspondingly $m_\perp$ is small in the linear regime of spin waves, and thus limits the SOT strength to compensate the spin-wave damping. Spin waves deep in the nonlinear regime suffer from magnon scattering events that attenuate spin-wave transmission, which contradicts the SOT antidamping effect, and thus not favorable for magnonic applications related to spin-wave amplification.

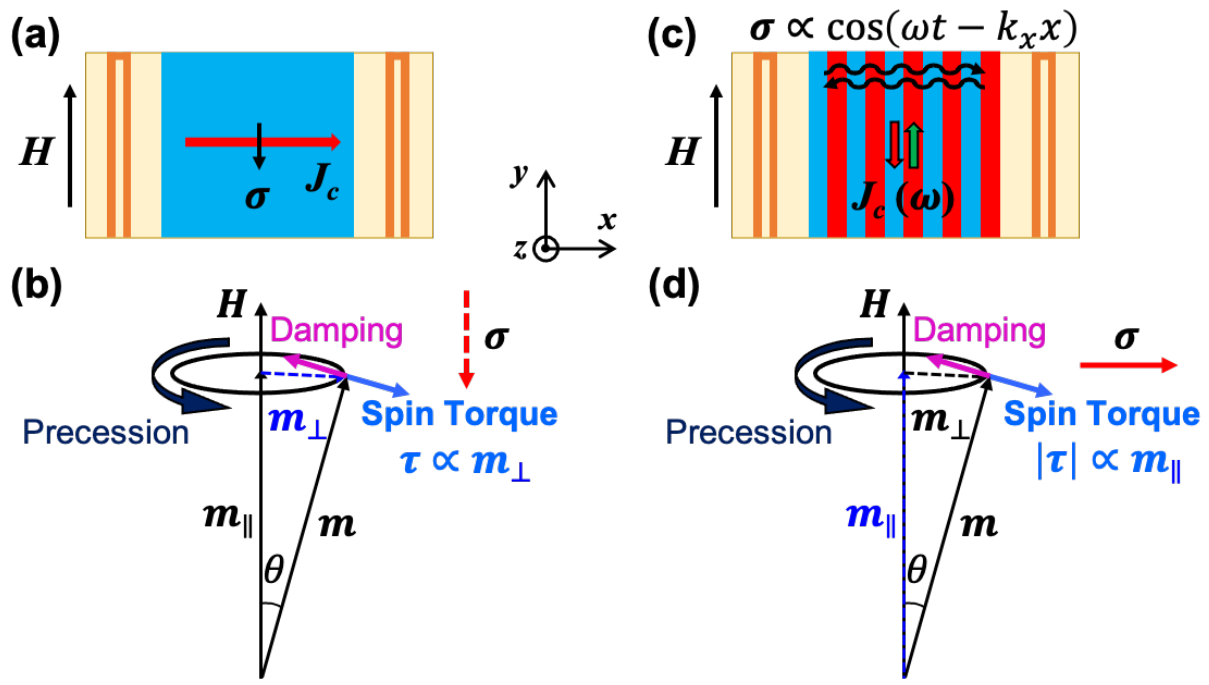

Figure 6-1 Spin-wave damping reduction mechanism of different device configurations (top view). (a) Spin-wave damping reduction in a device configuration with $\boldsymbol{\sigma}$ parallel or antiparallel to $\boldsymbol{H}$. (b) The illustration of SOT damping reduction mechanism with $\boldsymbol{\sigma}$ parallel or antiparallel to $\boldsymbol{H}$. (c) The structure with $\boldsymbol{\sigma}$ perpendicular to $\boldsymbol{H}$ and SOT proportional to $cos(\omega t - k_x x)$, designed to phase-match to and thus amplify the spin waves with wavevector k_x. (d) SOT for $\boldsymbol{\sigma}$ perpendicular to $\boldsymbol{H}$ and in the plane spanned by $\boldsymbol{H}$ and $\boldsymbol{m}$. Note that for (a) and (b), the strength of spin torque is proportional to $m_\perp$, which is much smaller than the SOT in (c) and (d) for which the SOT proportional to $m_\parallel$ for typical spin waves in the small θ regime.

In this work, we propose spin-wave damping reduction based on the device configuration shown in Figure 6-1(c), where the rf current is made in the direction along $\boldsymbol{H}$ and accordingly $\boldsymbol{\sigma}$ is perpendicular to the precession axis, and thus the maximum strength of SOT is changed as proportional to $m_\parallel$ (or m_y), where $\boldsymbol{m}_\parallel$ is the projection of $\boldsymbol{m}$ along the precession axis [Figure 6-1(d)]. In this situation, the torque strength can be much larger compared with the former configuration in Figure 6-1(a, b), since $m_\parallel$ is typically much larger than $m_\perp$ for spin waves in the small θ regime. The maximum strength is achieved when $\boldsymbol{\sigma}$, $\boldsymbol{m}$ and the precession axis are in the

same plane, i.e., $\boldsymbol{\sigma}$ is phase-matched to $\boldsymbol{m}$. For the single domain model or the FMR mode ($k = 0$) as in Figure 6-1(b, d), this is identical to $\boldsymbol{\sigma}$ or SOT being temporally synchronized to $\boldsymbol{m}$ or magnetic oscillations, i.e., AC SOT. Similar AC/rf SOT has been demonstrated capable of spin waves generation [113]. On the other hand, for the propagating spin wave mode with $k \neq 0$, additional spatial synchronization between $\boldsymbol{\sigma}$ or SOT and $\boldsymbol{m}$ or spin waves is required for maximally reducing the spin-wave damping. Considering both temporal and spatial synchronization between SOT and spin waves, $\boldsymbol{\sigma}$ and thus $\boldsymbol{\tau}$ takes the form, $\cos(\omega t - k_x x)$, as shown in Figure 6-1(c), which can be viewed as a traveling SOT wave. Just like the synchronization between electron bunches and electromagnetic waves, which leads to energy transfer between them in traveling-wave tubes (TWTs), the synchronization between SOT wave and spin waves can lead to energy transfer to spin waves to amplify them, following similar traveling wave amplification principle.

6.2 Numerical Calculation Based on Single Domain Model

To verify that AC SOT when synced with spin waves is more efficient in reducing spin-wave damping, we first perform the numerical calculations based on single domain model, as discussed in Section 3.1. The numerical calculation is based on Equation Set (3.2)-(3.4) with $\eta = \eta_0 \cos\omega t$ and $\theta_0 = 90°$, that is for the situation when AC SOT is temporally synchronized and in-phase with the magnetic oscillations. The same parameters as in Section 3.1 are applied as $\boldsymbol{m}(t = 0) = (0,0,1)$, and $\alpha = 0.1$, $\omega_0 = 2\pi \times 1.2$ GHz, $\omega_1 = \omega_0/300$, corresponding to $H_{ap} = 430$ Oe and $h = 1.4$ Oe, respectively. These parameters with small AC magnetic field ($h = 1.4$ Oe) for spin-wave excitation lead to a very small precession angle $\theta \approx 0.95°$ at $\eta = 0$. Figure 6-2 shows how the spin-wave gain, defined as $m_x(\eta)/m_x(0)$, depends on the SOT strength, indicated by η. The dependency for the case of spin-wave damping reduction based on DC SOT is also plotted as a

comparison. It can be seen from the figure that AC SOT with $\boldsymbol{\sigma} \perp \boldsymbol{H}$ is much more efficient in reducing spin-wave damping compared with DC SOT with $\boldsymbol{\sigma} \parallel -\boldsymbol{H}$, which results from the small θ and hence the strength of AC SOT proportional to $m_{\parallel}$ is much larger than that of DC SOT proportional to $m_{\perp}$. The numerical calculations based on the single domain model only considers the temporal synchronization between AC SOT and spin waves, and complete micromagnetic simulations are necessary when both spatial and temporal synchronizations need to be considered, which will be discussed in the next section.

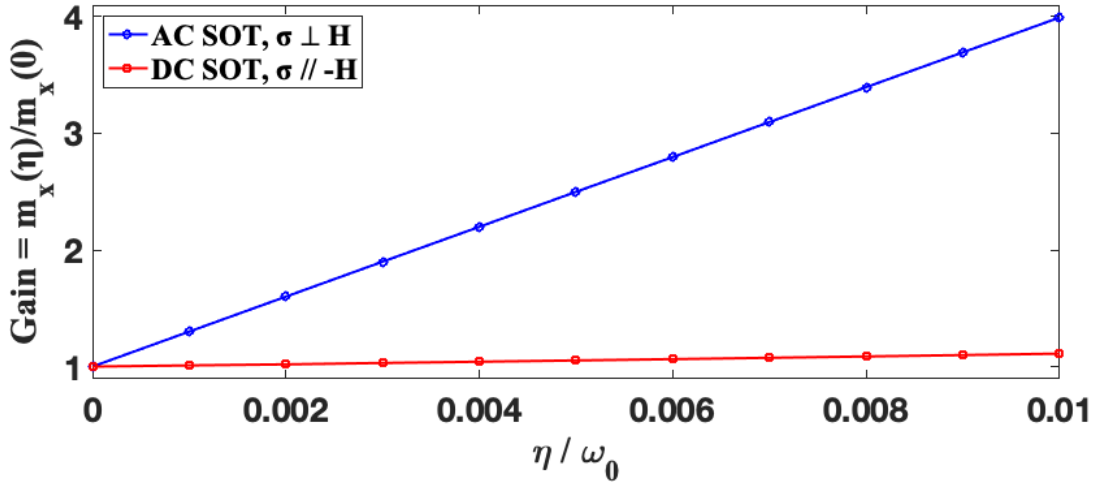

Figure 6-2 Dependency of precession amplitudes amplification on SOT strength (indicated by η normalized by ω_0) for AC SOT with $\boldsymbol{\sigma} \perp \boldsymbol{H}$ and DC SOT with $\boldsymbol{\sigma} \parallel -\boldsymbol{H}$ based on numerical calculation with single domain model [Equation Set (3.2)-(3.4)]. The parameters are $\boldsymbol{m}(t=0) = (0,0,1)$, and $\alpha = 0.1$, $\omega_0 = 2\pi \times 1.2\ GHz$, $\omega_1 = \omega_0/300$, same as Section 3.1.

6.3 Micromagnetics Simulation

The micromagnetic simulation model is based on a quasi 1-dimensional ferromagnetically coupled spin chain, shown schematically in Figure 6-3(a). The spin chain has a length of 8192 nm extended by periodic boundary conditions along y direction and with 64 nm long exponential damping

profile set on each end tested to be sufficient to reduce spin-wave reflection. The material parameters are set based on YIG with $M_s = 120\,\mathrm{emc/cm^3}$ and exchange stiffness $A_{ex} = 0.3\,\mathrm{erg/cm}$. Gilbert damping constant α, however, is set as 0.02 to reduce the simulation time required for the system to reach steady state, which has impact on spin-wave characteristics such as the decay length but will not alter the damping reduction phenomena. YIG is biased by a fixed magnetic field of 500 Oe along y direction. Spin-wave excitations by antennas are implemented in the simulations using AC magnetic fields with spatial profiles obtained from COMSOL simulations (as discussed in Section 3.4). The corresponding antenna for spin-wave excitation is a CPS with the widths of the conductors and their separation all being 100 nm, placed at 1050 nm from the left end of the spin chain.

The result of spin-wave propagation at 2 GHz is shown in Figure 6-3(b) as a color plot of $m_x(x,t)$ in space and time. The transmitted spin-wave amplitudes are calculated in the following steps: 1) extract the amplitudes of $m_x(x)$ at each x from its time evolution in the steady states; 2) take the spatial averages of the amplitudes of $m_x(x)$ over 300 nm range of x from the right end of the spin chain. The data of $m_x(x,t)$ for calculating transmitted spin-wave amplitudes are marked by the dashed white box in Figure 6-3(b). By sweeping the spin-wave excitation frequency, the passband of the spin waves is obtained and shown in Figure 6-3(c), which shows a transmission peak at ~1.9 GHz corresponding to the spin-wave modes coupled most efficiently to the spin-wave excitation antenna.

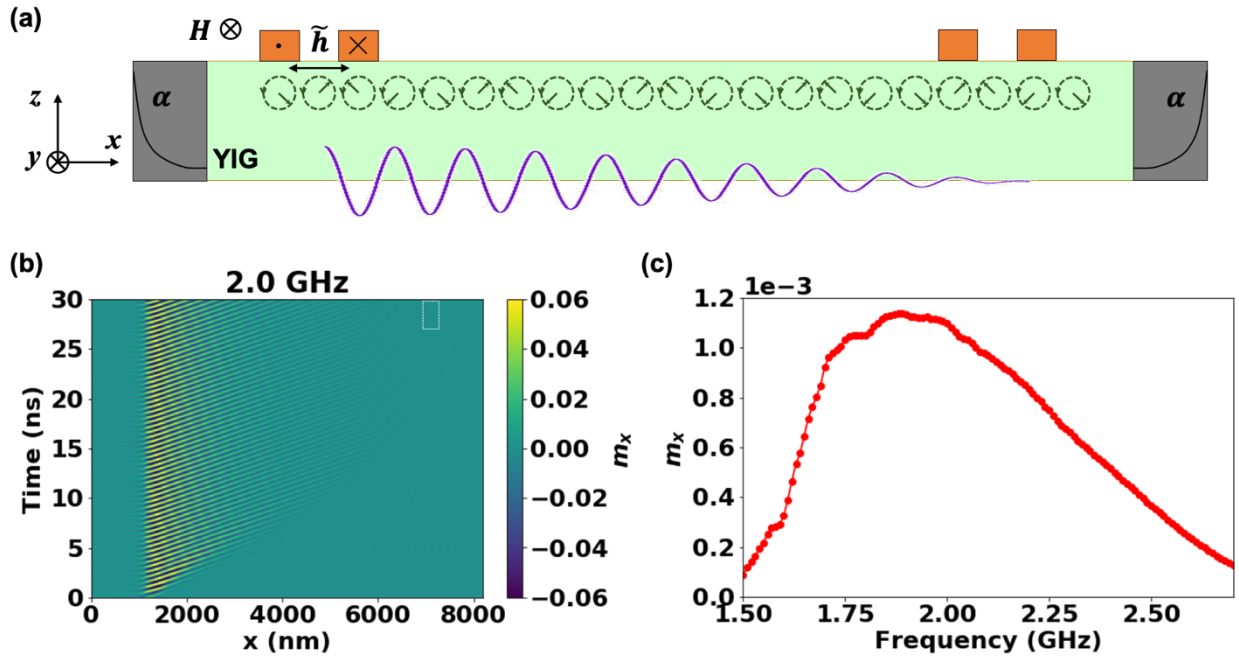

Figure 6-3 Micromagnetic simulation model. (a) Schematic of the simulation model (side view) based on a quasi 1-dimensional ferromagnetically coupled spin chain of 8192 nm long extended by periodic boundary conditions along y direction. The gray areas on each end indicate the 64 nm long exponential damping profile to reduce spin-wave reflection. The parameters are chosen as $M_s = 120\ emc/cm^3$, $A_{ex} = 0.3\ erg/cm$ and $\alpha = 0.02$. (b) Color plot of $m_x(x,t)$ in space and time showing spin-wave propagation. The white dashed box marks the region used for calculation of transmitted spin-wave amplitudes. (c) Frequency dependency of the transmitted spin-wave amplitudes that shows a peak at ~1.9 GHz.

The traveling SOT wave can be simulated with spin polarization that has a square-wave spatial profile whose fundamental harmonic is $\hat{\sigma}\cos(k_x x)$, where $\hat{\sigma}$ is along x direction. Accordingly, with temporal evolution considered, the SOT wave is $\hat{\sigma}\cos(k_x x)\cos(\omega t + \varphi)$, which consists of two counter-propagating traveling waves, i.e., $\hat{\sigma}\cos(k_x x)\cos(\omega t + \varphi) = \frac{1}{2}\hat{\sigma}\cos(\omega t - k_x x + \varphi) + \frac{1}{2}\hat{\sigma}\cos(\omega t + k_x x + \varphi)$. In the simulations, the square wave has 8 periods each 300 nm wide and φ is introduced as the parameter to tune the SOT wave in phase with the spin waves. For spin waves in DE configuration, $\frac{1}{2}\hat{\sigma}\cos(\omega t - k_x x + \varphi)$ will interact with top surface spin waves with

the same wavevector. Considering α in the simulation is much larger than the typical value ($\sim 10^{-5}$) in actual YIG, the absolute values of current densities in the simulation responsible for SOT generation will be not a direct reflect of those in actual experiments, and thus we normalize the coefficient η of SOT in $\boldsymbol{\tau} = \eta \boldsymbol{m} \times (\boldsymbol{\sigma} \times \boldsymbol{m})$ [based on Equation (3.5)] to the resonant precession frequency $\omega_0 = 2\pi \times 2$ GHz similar to the single domain model in the previous section. Spin-wave gain can be calculated as $m_x(\eta)/m_x(0)$, where $m_x(\eta)$ is the transmitted spin-wave amplitudes at SOT with coefficient η and $m_x(0)$ is the transmitted spin-wave amplitudes at $\eta = 0$ when no SOT is applied. The frequency dependency of the spin-wave gain is shown in Figure 6-4(b) for $\frac{\eta}{\omega_0} = 6.4 \times 10^{-4}$, $\varphi = -12°$ and $168°$ ($180°$ phase difference). It can be seen from the figure that the spin-wave gain is oscillating with respect to the frequency and whenever a peak appears in the $-12°$ curve, the $168°$ curve shows a corresponding valley, and vice versa. This is a result of the change of the relative phase difference $\Delta\varphi$ between SOT wave and spin waves at different frequencies, which we shall discuss in detail later. It can also be observed from the figure that a maximum gain exists at 2 GHz. By sweeping φ from $0°$ to $360°$ at 2 GHz, the phase dependency of the spin-wave gain can be obtained and shown in Figure 6-4(c), where the maximum and minimum gain occur at $348°$ (i.e., $-12°$) and $168°$, marked by blue and green arrows respectively. The phase dependency of the gain also results from the changing phase difference between the SOT wave and the spin waves.

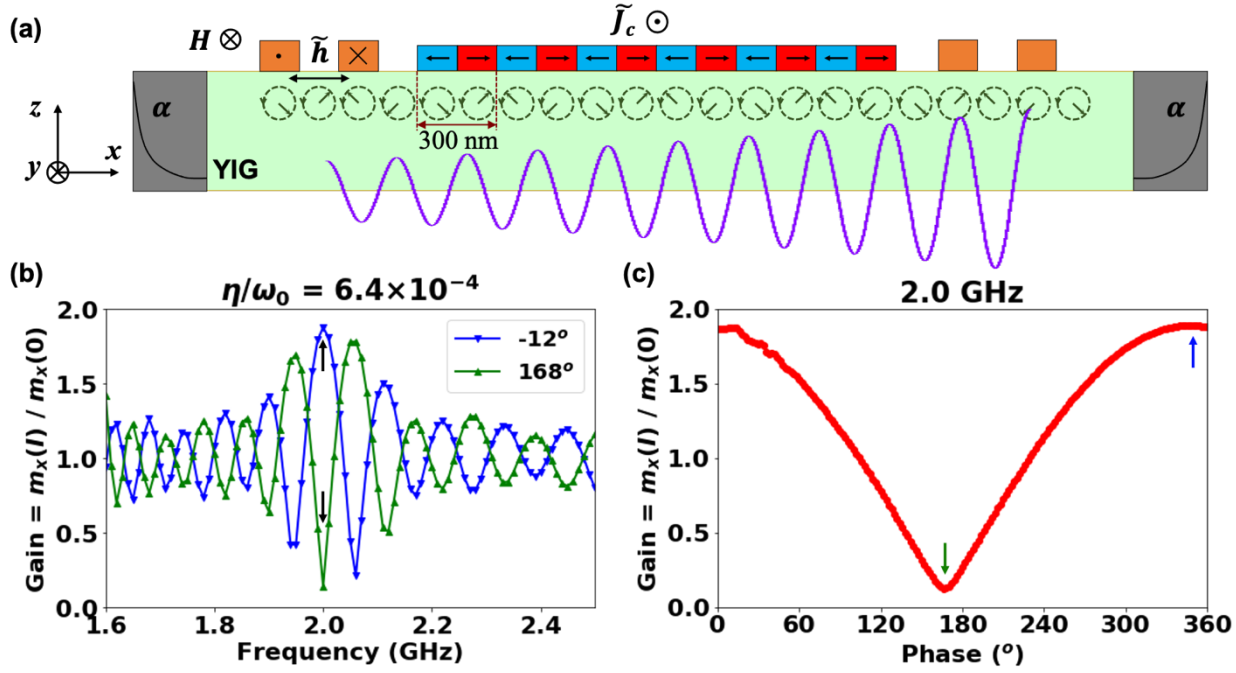

Figure 6-4 Micromagnetic simulation of amplification of spin waves by a SOT wave with a square-wave spatial profile. (a) Schematic of the simulation model (side view). The periodic blue and red rectangles form a "comb" structure and indicate the square-wave spatial profile of spin-polarization. (b) Frequency dependency of spin-wave gain, defined as $m_x(\eta)/m_x(0)$, for $\frac{\eta}{\omega_0} = 6.4 \times 10^{-4}$, $\varphi = -12°$ and 168°. At 2 GHz (marked by the black arrows), spin-wave gain reaches maximum at $\varphi = -12°$ and minimum at $\varphi = (-12 + 180)° = 168°$. (c) Phase dependency of the spin-wave gain for $\frac{\eta}{\omega_0} = 6.4 \times 10^{-4}$ at 2 GHz. The maximum and minimum of gain are marked by blue and green arrows occurring at $\varphi = 348°$ (i.e., $-12°$) and 168°, respectively.

To better understand the frequency and phase dependency of the gain, we plot $m_x(x,t)$ in space and time focused onto the SOT "comb" region for three different frequencies: 1.94 GHz, 2 GHz, 2.06 GHz, and for $\varphi = -12°$ (i.e., 348°) and $\varphi = 168°$ situations, shown in Figure 6-5. At 2 GHz, it can be clearly seen that the SOT wave is in phase with the spin waves at $\varphi = -12°$ and out of phase at $\varphi = 168°$ leading to amplification or attenuation of the spin waves, respectively, which thus explains the phase dependency of spin-wave gain in Figure 6-4(c). Similarly, at 1.94 GHz and 2.06 GHz, the SOT wave is in phase with and thus amplify the spin waves at $\varphi = 168°$; the SOT

wave is out of phase with and thus attenuates the spin waves at $\varphi = -12°$. The reason that at different frequencies the value of φ changes when the SOT waves are in phase with the spin waves is the relative phase difference, $\Delta\varphi$, between the SOT waves and the spin waves at $\varphi = 0°$ changes with frequency. To be more specific, the relative phase difference can be calculated as $\Delta\varphi(x') = \varphi_{SOT}(x') - \varphi_{SW}(x')$, where $\varphi_{SOT}(x') = \omega t - k_{SOT}x' + \varphi$, $\varphi_{SW}(x') = \omega t - k_{SW}(x' + L)$ and k_{SOT}, k_{SW} are the phases and the wavevectors of the SOT wave and the spin waves at x', respectively, L is the separation between the spin-wave emitting antenna and the "comb", and $x' = 0$ counts from the left end of the "comb". Therefore, $\Delta\varphi(x') = (k_{SW} - k_{SOT})x' + k_{SW}L + \varphi$. When k_{SW} and k_{SOT} are close, the $(k_{SW} - k_{SOT})x'$ term is small, but even in this case, $k_{SW}L$ still contributes to the relative phase difference in addition to φ, and since k_{SW} changes with frequency as a result of the spin-wave dispersion, $\Delta\varphi(x')$ changes with frequency accordingly, leading to the oscillations of spin-wave gain for a fixed φ in Figure 6-4(b). When k_{SW} and k_{SOT} are equal at 2 GHz, or equivalently speaking, the spin-wave wavelength matches the period of the "comb" at 300 nm, the SOT wave and spin waves are spatially synchronized, the $(k_{SW} - k_{SOT})x'$ term vanishes and thus $\Delta\varphi(x')$ no longer has no x' dependency, leading to a perfect phase-matching situation and the achievable maximum spin-wave gain when φ is properly tuned.

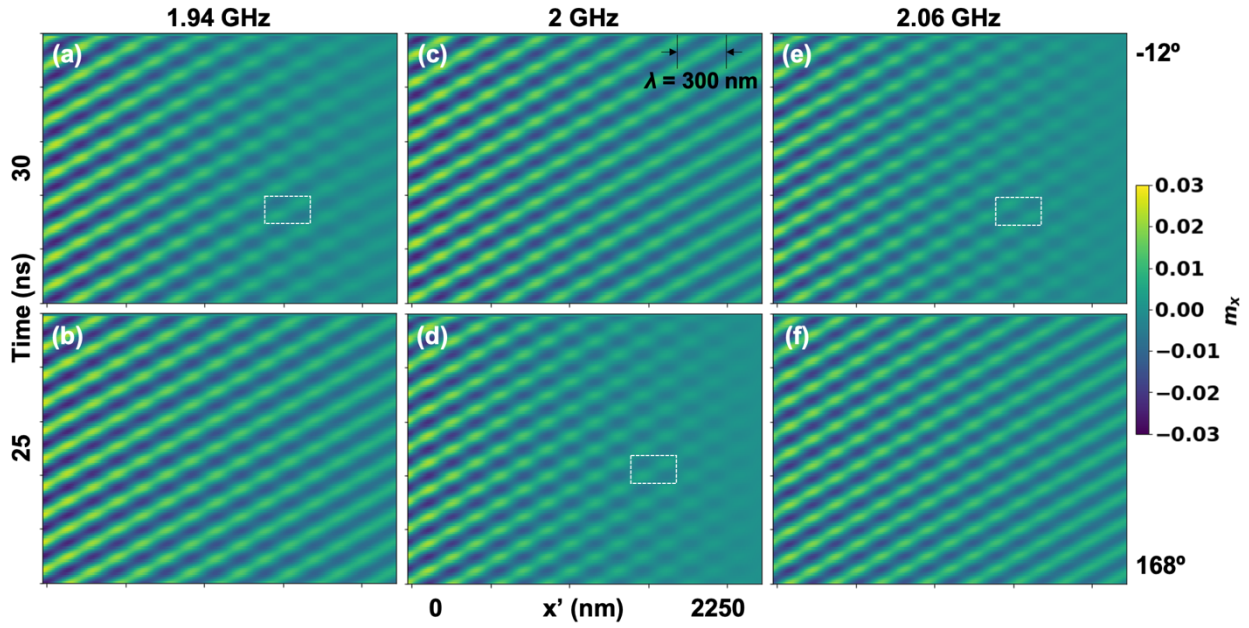

Figure 6-5 Color plots of $m_x(x,t)$ in space and time focused onto the SOT "comb" region at 1.94 GHz (a, b), 2 GHz (c, d) and 2.06 GHz (e, f) for $\varphi = -12°$ (a, c, e) and $\varphi = 168°$ (b, d, f). The SOT waves are in phase with and thus amplify the spin waves in (b, c, f). The SOT waves are out of phase with (shown as the more obvious grid-like features highlighted by the dashed white boxes in the color plots) and thus attenuates the spin waves in (a, d, e).

So far, we have demonstrated numerically that temporal and spatial synchronizations (i.e., phase matching) between the SOT wave and the spin waves leads to a peak gain of spin waves in a narrow frequency range. We shall then investigate this phenomenon experimentally.

6.4 Experimental Results and Discussions

To experimentally implement the square-wave spatial profile of the SOT wave, we use alternating Pt and Ta bars to form the "comb" structure on top of a 1 μm thick LPE grown YIG, with the rf current propagating along the bar length direction (y), shown as the optical microscope image in Figure 6-6(a). Pt and Ta have opposite spin Hall angles and thus lead to the square-wave spatial profile and make the push pull effect of the torque. Under the application of magnetic field H along y direction, our devices observe the DE configuration with spin waves propagating along $+x$

direction, and spin waves are excited and detected with CPSs where the widths of the conductors and their separation all being 10 μm. The spin-wave detector is moved further away from the "comb" to reduce the direct electromagnetic coupling's contribution to the detected signals. Pt and Ta bars of the "comb" are both 20 μm in width, designed to optimally match the spin waves with 40 μm wavelength.

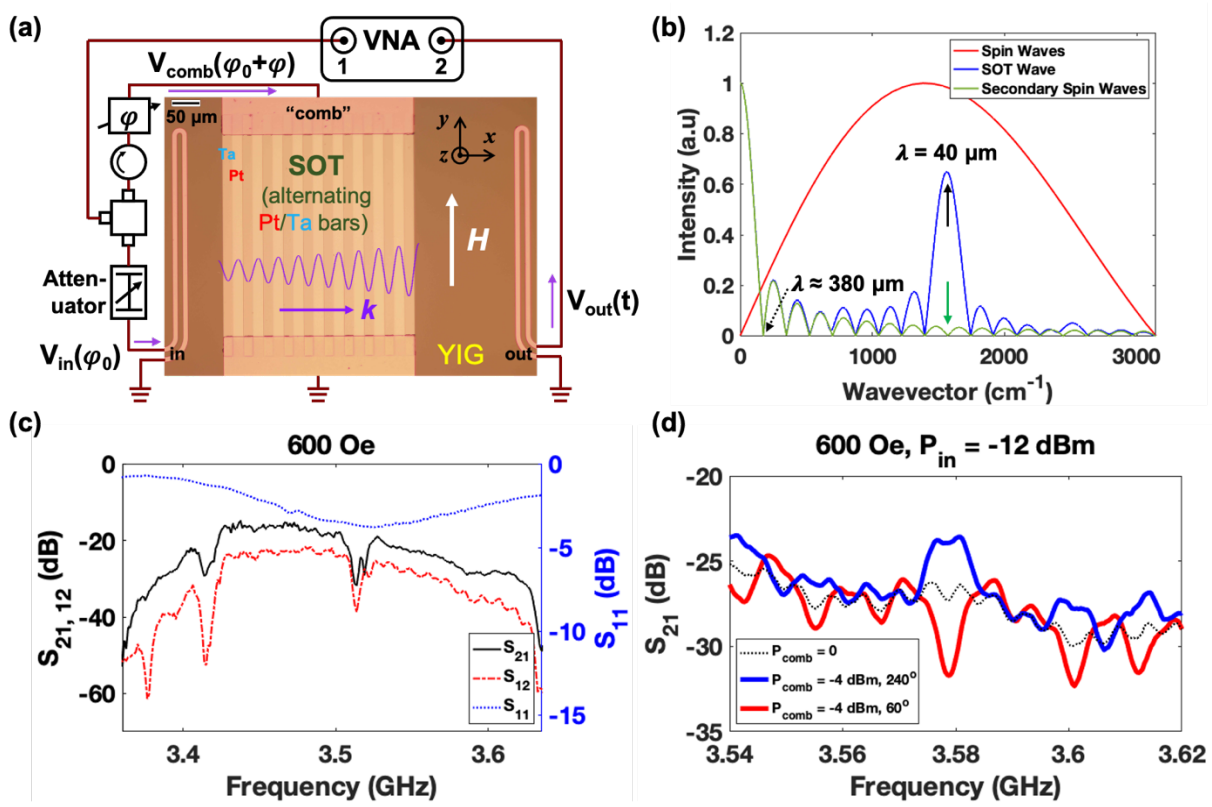

Figure 6-6 (a) Optical microscope image of the spin-wave device with a "comb" consisting of alternating Pt and Ta bars on top of a 1 μm thick LPE YIG (top view). External magnetic field is applied along y direction, and spin waves are excited and detected by the CPSs on the left and right, respectively. For the complete device characterization, the input powers to the spin-wave emitter and the "comb" are both provided by Port 1 of VNA via a power splitter. In the "comb" branch, an isolator is added to reduce signal reflection from the "comb" and the phase shifter is used to tune the SOT wave in phase with the spin waves. In the spin-wave emitter branch, an attenuator is introduced to maintain the spin-wave excitation power in "comb" power dependency measurements. The spin-wave detector is connected to Port 2 of VNA. (b) Calculated wavevector distributions, based on COMSOL simulations, of the spin waves, SOT

waves and the secondary spin waves. The wavevector distribution range has been focused onto that of the spin-wave main passband. The secondary spin waves indicate spin waves excited inductively by the "comb". (c) S parameter characterizations between Port "in" and Port "out" of the spin-wave device in the absence of the SOT wave showing the spin-wave passband and non-reciprocity of the DE spin waves. (d) S_{21}, quantifying the spin-wave transmission, at 600 Oe with P_{in} = -12 dBm and P_{comb} = -4 dBm exciting the SOT wave at $\varphi = 240°$ (blue curve) and $\varphi = 60°$ (red curve). The situation when no SOT wave is excited (black dotted curve) is also plotted for comparison. The frequency range has been focused onto 3.54 – 3.62 GHz highlighting the peak amplification and attenuation at 3.579 GHz.

Considering the resistivity difference between Pt and Ta, their thicknesses (t) need to be designed such that the current distribution inside the "comb" along x direction is uniform (i.e., Jt is constant along x direction, where J is the current density and t is the thickness) to separate the secondary spin-wave generation by the Oersted fields induced by the otherwise non-uniform current distribution [13]. The uniform current distribution requirement is equivalent to Pt bar and Ta bar having same sheet resistance [14], which can be realized with 4 nm Pt and 25 nm Ta. Besides the devices with "comb" structure, we also fabricate control devices replacing the "comb" with the same size Ta layer of 25 nm thickness. The resistance of the rectangular Ta layer and "comb" are both measured to be around 100 Ω, indicating that 4 nm Pt and 25 nm Ta possess same sheet resistance in our devices.

Figure 6-6(b) shows the calculated wavelength distributions based on COMSOL simulations (discussed in Section 3.4) of the spin waves, SOT waves and the secondary spin waves, which are generated by the spin-wave emitting CPS inductively, "comb" structure through spin Hall effect (SHE), and the Oersted fields with rf current along y direction in the "comb", respectively. The

[13] The Oersted field generated from current J passing through a conductor with thickness t can be estimated by $H_{Oe} = \frac{1}{2}Jt$ [114]. Nonuniform Jt or H_{Oe} distribution results in secondary spin waves of the same wavelength as the targeted spin waves for amplification, which has been verified by COMSOL simulations.
[14] Since $J = \sigma E = E/\rho$ (Ohm's law) and E is uniform along x direction in the "comb" structure, uniform Jt is identical to uniform ρ/t, and thus Pt and Ta bars have the same sheet resistance: $\rho_{Pt}/t_{Pt} = \rho_{Ta}/t_{Ta}$.

peak of SOT wave corresponds to 40 μm and locates within in the spin-wave passband. With uniform current distribution along x direction, the "comb" is essentially a MS line and thus couples most efficiently to secondary spin-wave wavelengths longer than its width of 380 μm (as discussed in Section 4.1), which is greater than the targeted spin-wave wavelength of 40 μm; the components of the secondary spin waves above the cutoff wavevector have very small intensities and vanish at the wavevector corresponding to 40 μm marked by the green arrow. Therefore, the spin-wave amplification at the targeted 40 μm wavelength will only have SOT contributions, free from the Oersted fields induced secondary spin waves impact.

The initial Scattering (S-) parameters characterizations are shown in Figure 6-6(c) obtained by directly connecting the spin-wave emitter and detector (i.e., Port "in" and "out" of the spin-wave device in the figure) to Port 1 and 2 of the Vector Network Analyzer (VNA), respectively, with 600 Oe magnetic field applied along y direction. The S_{11} parameter, shown as the dotted blue line, is equal to the S_{22} parameter and is indicative of the power absorbed by the YIG. The S_{21} parameter, shown as the solid black line, indicates the transmitted power, and is larger than the S_{12} parameter, shown as the red dot-dashed line, due to the nonreciprocity of DE spin waves [90]–[92].

The complete device characterization setup is shown in the circuits around the optical microscope image in Figure 6-6(a). The input powers to spin-wave emitter and the "comb" are both provided by Port 1 of VNA via a power splitter to realize temporal synchronization between the SOT wave and the spin waves with low phase noise. In the "comb" branch, an isolator is added to reduce signal reflection from the "comb" and the phase shifter is used to tune the SOT wave in phase with the spin waves. In the spin-wave emitter branch, an attenuator is introduced to maintain the spin-wave excitation power, and hence the input spin-wave amplitudes, in "comb" power dependency

measurements, where "comb" power is changed by varying the output power of VNA. The spin-wave detector is connected to Port 2 of VNA, and thus S_{21} quantifies the transmitted spin-wave amplitudes modified by the SOT wave from the "comb".

Figure 6-6(d) shows S_{21} measured at 600 Oe with -12 dBm power input to the spin-wave emitter and -4 dBm power input to the "comb" exciting the SOT wave at $\varphi = 240°$ (blue curve) and $\varphi = 60°$ (red curve). The situation when no SOT wave is excited (black dotted curve) is also plotted for comparison. The frequency range has been focused onto 3.54 – 3.62 GHz within the spin-wave passband highlighting the peak amplification and attenuation at 3.579 GHz. The gain in dB, shown in Figure 6-7(a), is calculated as $S_{21}(P_{comb}) - S_{21}(0)$, where $S_{21}(P_{comb})$ and $S_{21}(0)$ are S_{21} in dB for "comb" input powers of P_{comb} and 0, respectively. The oscillations of gain with respect to frequency is consistent with the micromagnetics simulation results, due to the change of the relative phase difference, $\Delta\varphi$, between the SOT waves and the spin waves at different frequencies, as discussed in the previous section. Also shown as the inset of the figure is the frequency dependent gain of the control sample with Ta replacing the "comb". The small oscillations (i.e., < 2 dB) of gain in the control sample probably results from the interaction between the spin waves and 1) the small secondary spin-wave components near the targeted 40 μm wavelength [15], and 2) direct electromagnetic coupling between "comb" and the spin-wave detector [16]. At 3.579 GHz for the peak gain of 3.36 dB from the "comb" device, the control sample shows below 0.7 dB gain, which indicates that the peak gain is mainly attributed to the SOT wave transferring energy to the

[15] The small secondary spin-wave components are the components above the cutoff wavevector (i.e., corresponding to 380 μm) in Figure 6-6(b). They can interfere with the spin waves and lead to the oscillations in frequency similarly due to their relative phase difference changes with frequency.

[16] The direct electromagnetic coupling between the "comb" and the spin-wave detector results in electrical signal in the latter. In the range of 3.54 – 3.62 GHz, the phase of this signal is almost constant with respect to frequency. The phase of the signal due to spin waves, on the other hand, changes with frequency. The composition of these two signals thus lead to the oscillations in frequency.

spin waves when they are tuned in phase. By repeating the measurements for different phase φ, the phase dependency gain can be obtained [Figure 6-7(b)] showing the maximum and minimum gain at 240° and 60°, marked by the blue and red arrows, corresponding to the SOT wave and spin waves are in phase and out of phase, respectively.

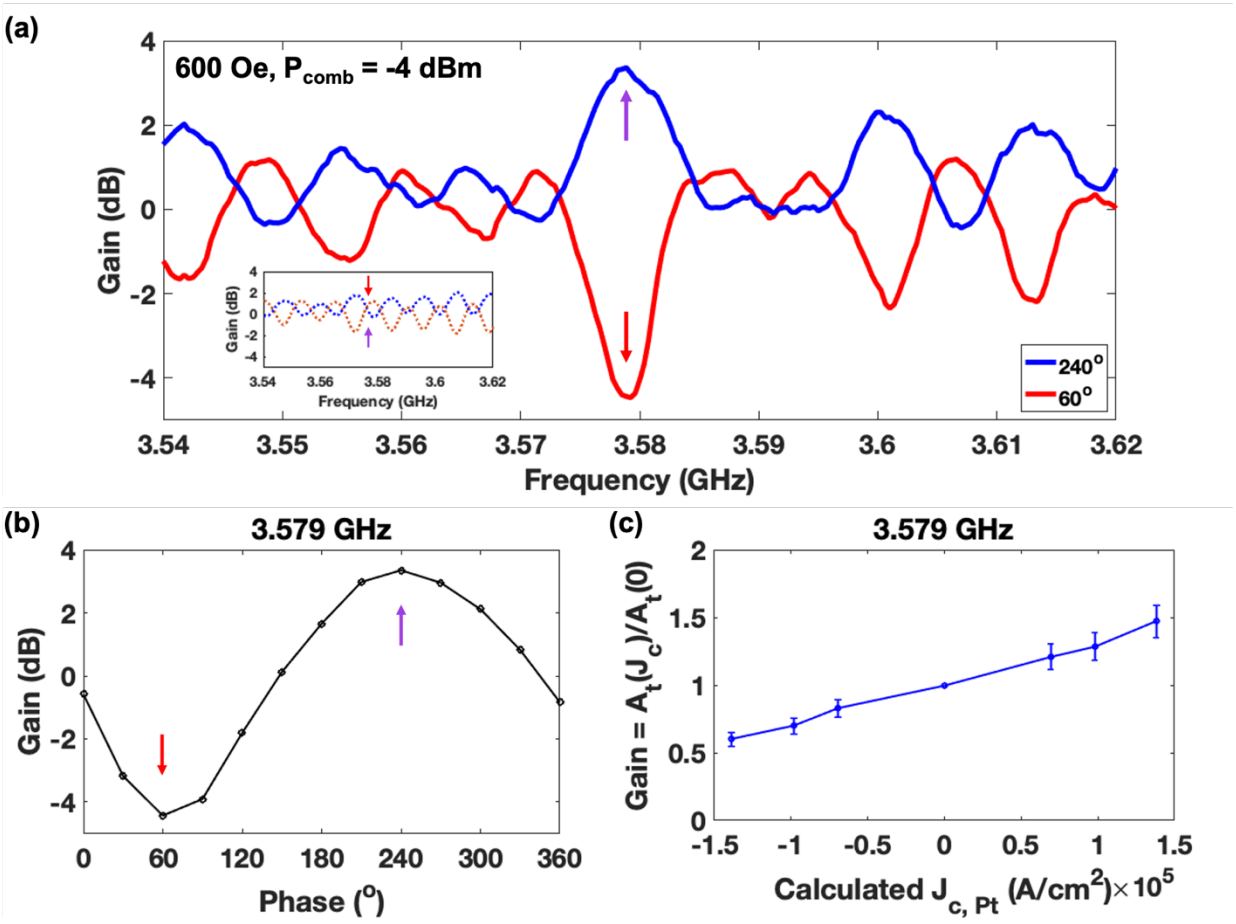

Figure 6-7 (a) Gain in dB calculated as $S_{21}(P_{comb}) - S_{21}(0)$ at 600 Oe, $P_{in} = -12\ dBm$, $P_{comb} = -4\ dBm$ for $\varphi =$ 240° and 60° with the maximum and minimum gain at 3.579 GHz, marked by the arrows. The inset shows the frequency dependent gain in the control sample due to impact from the secondary spin waves and the direct electromagnetic coupling between "comb" and the spin-wave detector. The gain at 3.579 GHz is below 0.7 dB. (b) Phase dependent gain at 3.579 GHz for the same condition of 600 Oe, $P_{in} = -12\ dBm$, $P_{comb} = -4\ dBm$. (c) Dependency of the gain ratio on the current densities in Pt, $J_{c,Pt}$, calculated from the input powers to the "comb". The

positive current densities are calculated from P_{comb} at 240° and the negative current densities are calculated from P_{comb} at 60°.

To investigate the efficiency improvement of the spin-wave amplification compared with the conventional configurations, we perform "comb" power dependency measurements while maintaining the input spin-wave amplitudes with $P_{in} = -12$ dBm. The "comb" powers can be converted into current densities in Pt [17] and the dependency of gain ratio on the calculated current densities [Figure 6-7(c)] shows with a linear dependency in our measurement range. Compared with the similar linear dependency of spin-wave amplification on current density in the conventional configuration on LPE YIG reported in [14] that shows a 10% amplification at around 3.85×10^5 A/cm^2, our devices with the "comb" configuration demonstrates the 10% amplification at 3.27×10^4 A/cm^2, a 12-time enhancement in efficiency. It should be noted that even the maximum P_{comb} in our measurements, -4 dBm (< 0.4 mW), is too small to induce any significant heating effect, which is reflected in the "comb" power dependency measurements that the frequency of maximum gain stays at 3.579 GHz for different P_{comb} at 600 Oe suggesting no heating induced M_S lowering exists in our measurements.

By design, our device is targeted to optimally amplify the spin waves at a specific wavelength (i.e., 40 μm) determined by the period of the "comb". This can be verified by measuring the gain at different fields. Figure 6-8(a-c) show the gain in dB obtained at 575 Oe, 600 Oe [same as Figure 6-7(a)], 625 Oe with $P_{in} = -12$ dBm, $P_{comb} = -4$ dBm when the SOT wave is in phase (i.e.,

[17] Since the frequency of rf currents in the "comb" is below 4 GHz, corresponding to electromagnetic wave (EM) wavelength of above 7.5 cm, and the "comb" dimension is submillimeter, less than 1.3% of the EM wavelength, the "comb" can be viewed as a lumped $R = 100\ \Omega$ resistor and the current density can be calculated as $J_c W = \sqrt{P_{comb}/R}$, where W is the cross section. The negative J_c and their corresponding gain ratio is calculated for the same P_{comb} with 180° phase difference from the positive J_c. Considering the uniform Jt distribution in our device design, the current densities in Pt and Ta bars are different. The calculated J_c is the current density in Pt, for a fair comparison with [14] that also uses SOT from Pt to amplify spin waves in YIG.

240°) and out of phase (i.e., 60°) with the spin waves. The (field, frequency) pairs of the maximum gain, marked by the blue arrows in the figures, are highlighted as white circles in the S_{21} color plot in Figure 6-8(d). The locations of the maximum gain follow along an artificially added black dashed line corresponding to the spin wave with a specific wavevector (as discussed in Section 4.1), and thus shows that spin waves are optimally amplified at a specific wavelength.

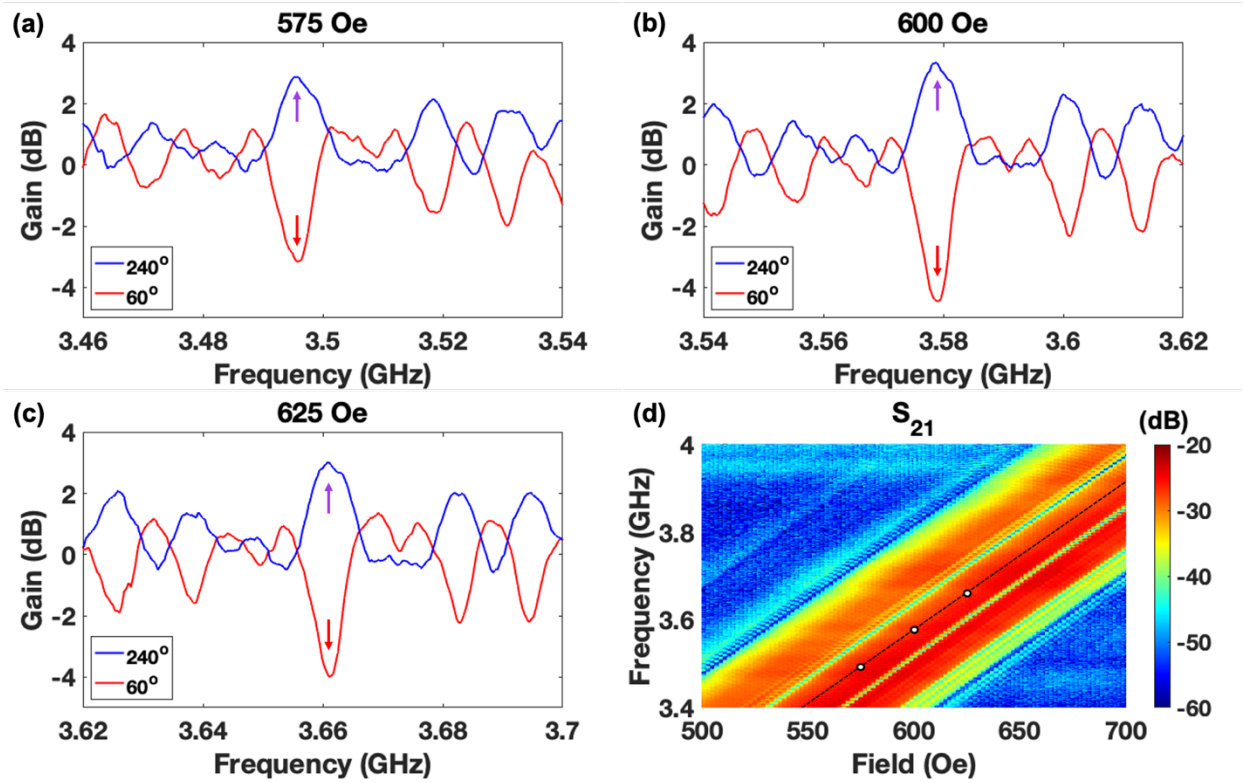

Figure 6-8 Demonstration of the maximum spin-wave amplification at a specific wavelength by design. Gain in dB obtained at 575 Oe, 600 Oe [same as Figure 6-7(a)], 625 Oe with $P_{in} = -12\ dBm$, $P_{comb} = -4\ dBm$ when the SOT wave is in phase (i.e., 240°) and out of phase (i.e., 60°) with the spin waves. (d) Color plot of S_{21} with the (frequency, field) pair of the peak gain [marked by blue arrows in (a-c)] highlighted as white circles, which follow along an artificially added black dashed line corresponding to the spin wave with a specific wavelength.

Finally, we mark that our proposed device can be used as a spin-wave based filter with built-in amplification that has a narrow bandwidth (i.e., ~10 MHz in our device) near a specific frequency

corresponding to the targeted spin-wave wavelength. The passband frequency, however, can be tuned by varying the applied magnetic field strength. On the other hand, the bandwidth can be increased by adopting a pitch modulation as used in an acoustic optical case [115] or generically in superlattice engineering of the "comb" to produce a sequence of sidebands in the wavevector spectrum of the SOT wave. The detail of the pitch modulation is beyond the scope of this work. This pitch modulation engineering can lead to a controllable enhancement of the bandwidth and thus makes our proposed spin-wave device flexible and appealing in practical applications.

6.5 Conclusions

In this chapter, we propose and demonstrate the use of the traveling wave interaction between the SOT wave and the spin waves to amplify the latter, via micromagnetics simulations and experiments, in a YIG spin-wave device with a "comb" structure consisting of alternating Pt and Ta bars. The SOT wave is generated by SHE when rf currents are passing along the bar length direction. When the SOT wave and the spin waves are tuned in phase, the gain is maximized for the spin wave with a specific wavevector corresponding to the periodicity in the "comb", as a result of the temporal and spatial synchronization between the SOT wave and the spin waves. The maximum gain at 600 Oe is 3.36 dB, which can be achieved at current densities 12-time smaller compared with the conventional spin-wave amplification configuration. The improved spin-wave amplification efficiency can be further enhanced by using materials with larger spin Hall angle, such as TIs. Our proposed device can find application as a tunable spin-wave amplifier or a filter with built-in amplification.

7 Non-Local Spin Transport in Magnetic Insulators

7.1 Introduction

Besides coherent excitation by inductive microwave techniques, such as the spin waves discussed in Chapters 5 and 6, spin waves excitation or magnon injection can be induced by spin Hall effect (SHE) to convert charge current to spin. On the detection side, similarly, spin waves detection is via inverse spin Hall effect (ISHE) to convert spin to charge current. Experimentally, this non-local spin transport was first reported in YIG with Pt as the spin injector and detector, where it was claimed that spin orbit torque (SOT) from Pt compensated the magnetic damping to excite the ferromagnetic resonance (FMR) [116]. Later experiments, based on the similar non-local spin transport geometry (shown in Figure 7-1), have demonstrated non-local spin transport via magnon diffusion and relaxation in ferrimagnetic insulators (e.g., YIG) [117]–[119], antiferromagnetic insulators (e.g., α-Fe_2O_3) [120], [121], 2D van der Waals magnets (e.g., $MnPS_3$) [122], etc. On the other hand, in addition to being carried by magnon diffusion and relaxation, non-local spin transport can also be mediated by spin superfluid (see Section 2.4) [19], [20], [123]. Experiments in canted antiferromagnet Cr_2O_3 [22] and graphene [21] have demonstrated some signatures of spin superfluid transport.

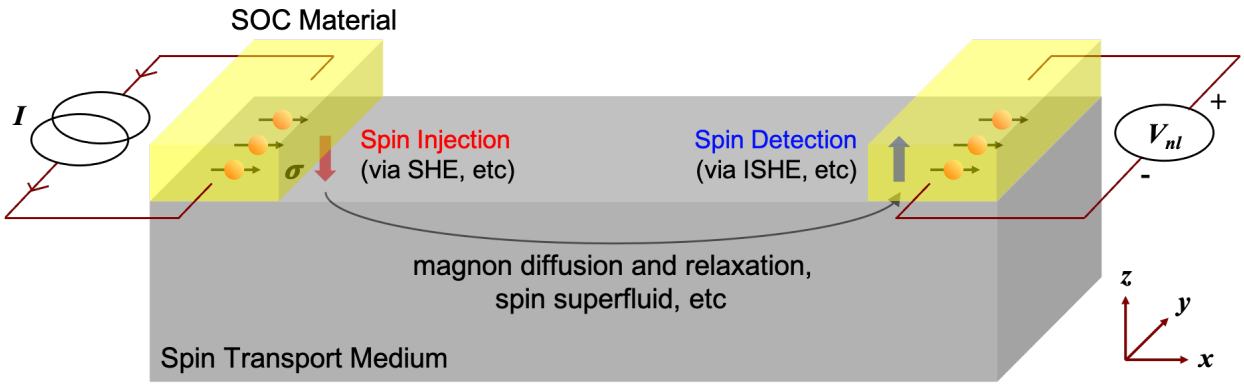

Figure 7-1 Typical non-local spin transport geometry with two parallel bars made from SOC materials on top of a spin transport medium (via magnon diffusion and relaxation, spin superfluid, etc). The two bars are kept separately and function as the spin injector and detector, respectively. The spin-flip scattering process at the SOC material, spin transport medium interface is responsible for spin injection at the spin injector. The reciprocal process occurs at the spin detector.

In this short chapter, we will briefly discuss our research efforts on non-local spin transport in magnetic insulators, where the non-local signals are measured by the delta method described in Section 4.2. In Section 7.2, we will discuss the studies on YIG which yield consistent results with other literature reports. With the same device geometry, dimensions and measurement setup as YIG, we will present our preliminary results on non-local electrical signals in insulating antiferromagnetic $BiFeO_3$ (BFO), with the signals showing a nonlinear dependency of V_{nl} on I with a threshold current in reminiscent of the features in the initial report in YIG, where the detected signals are claimed to be mediated by coherent non-local spin transport [124].

7.2 Non-local spin transport in YIG

Among the non-local spin transport research, the ferrimagnetic insulator YIG is the most studied spin transport medium, due to its extremely low intrinsic magnetic damping and thus long spin diffusion length. In most of these studies, the devices are patterned by e-beam lithography with

spin injector and detector separation in submicron regime, where the non-local voltage signals (on the order of μV) are measured by lock-in techniques. When it comes to small signals with thermoelectric EMF as the major measurement error source, the delta method (see Section 4.2) is a powerful technique, yet less applied in the non-local spin transport studies.

Our devices for studying non-local spin transport in YIG are patterned by the standard photolithography process, and one example of the optical microscope images is shown in Figure 7-2(a). The YIG used in the experiments are 3 μm thick with a Gilbert damping parameter α~0.0003. The Pt bars are 10 nm thick, 80 μm long and 5 μm wide, and the smallest separation (among all devices) between the bars are 2 μm. The non-local signals are measured using the delta technique, with the positive polarity of the current source and voltmeter marked in Figure 7-2(b).

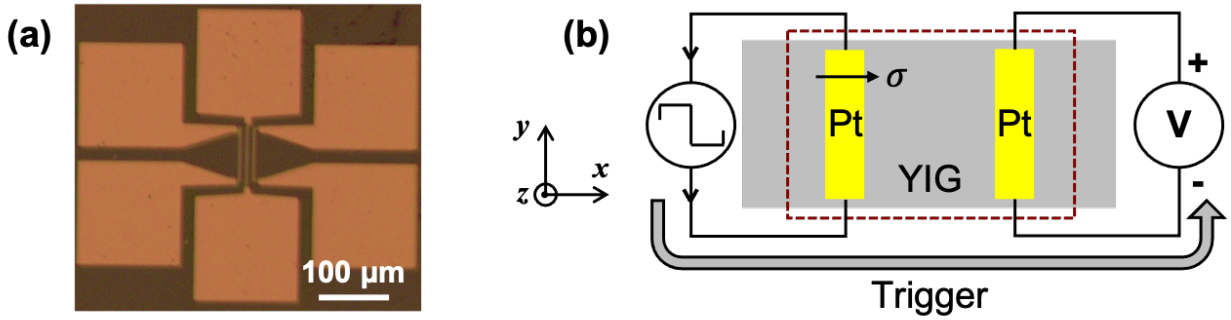

Figure 7-2 (a) Optical microscope image of a non-local spin transport device with 3 parallel Pt bars on top of 3 μm thick YIG. The square pads are Cr/Au for electrical contacts. (b) Measurement setup for non-local measurements (top view) by delta method with magnetic field applied along x or y direction.

Measurements are carried with a magnetic field applied along the spin propagation direction (x) or along the Pt bars direction (y), and the major results for 2 μm Pt bars separation are shown in Figure 7-3 (V_{nl} contains only odd order terms of I as in delta methods). The non-local signals' current dependency is shown in Figure 7-3(a). The magnetic field H is 500 Oe in these measurements enough to saturate the magnetization of YIG. When the magnetic field H is along

x direction, the non-local voltage V_{nl} scales linear with the applied current I; when the magnetic field H is along y direction, the non-local voltage V_{nl} vanishes. This is because the non-local spin transport is mediated by magnons whose excitation and detection result from the spin-flip scattering process at the YIG/Pt interface, which scales linearly with current I before any nonlinear effects (high current regime) kick in [125]. For the same reason, only the σ component collinear to the magnetic field H contributes to the magnon excitation and detection, and thus the non-local voltage V_{nl} is switched off when H is along y direction, orthogonal to σ. Figure 7-3(b) shows the field dependency of the non-local signals with 5 mA current driven in the spin injector Pt bar. Similarly, when H is along y direction and thus orthogonal to σ, V_{nl} is almost 0. When H is along x direction with magnitudes for YIG magnetization to saturate, V_{nl} stays almost constant; V_{nl} being non-zero at $H = 0$ results from the remanence of YIG [18].

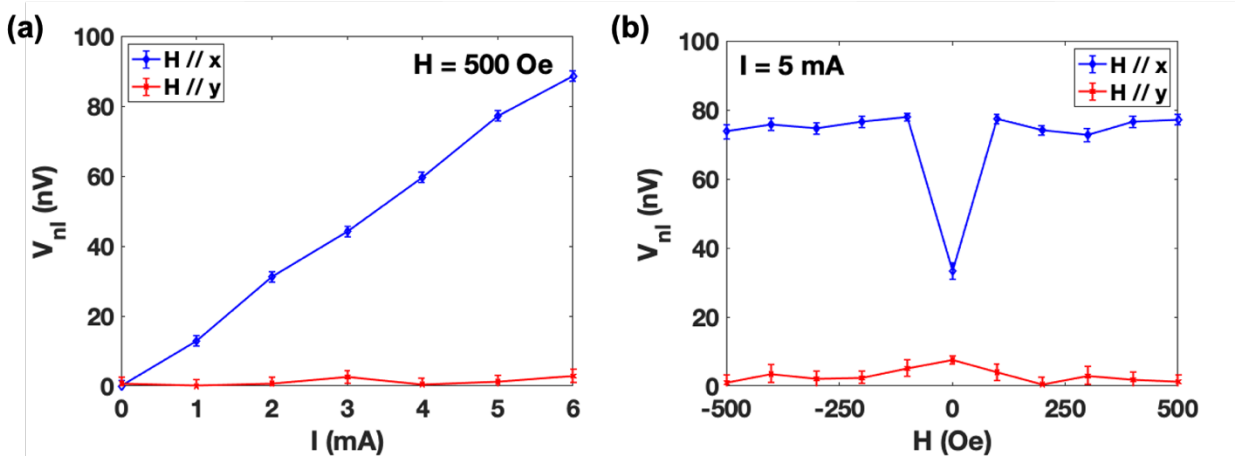

Figure 7-3 Major results of the non-local spin transport in Pt/YIG/Pt devices with 2 μm Pt bar separation. (a) Current dependency of the non-local voltage measured at 500 Oe. (b) Field dependency of the non-local voltage measured with 5 mA current driven in the spin injector Pt bar.

[18] The field step is 100 Oe, which results in the sharp drop in the blue curve in Figure *7-3*(b) from $H = \pm 100$ Oe to $H = 0$.

The current and field dependency features are in agreement with the literature reports on submicron thin YIG [117]–[119] and 3 μm YIG [61]. A 1D spin diffusion-relaxation model was derived in [117] that $V_{nl} = \frac{C}{\lambda} \frac{\exp(d/\lambda)}{1-\exp(2d/\lambda)}$, where d is the separation between the Pt bars, λ is the magnon spin diffusion length and C is a distance independent coefficient. λ is dependent on the Gilbert damping parameter α and also the surface condition of YIG in between the Pt bars, and C scales with the current density and is dependent of the YIG/Pt interface condition. Based on this argument, we can have a brief quantitative comparison between our results and the results in [117], which shows good consistency and is summarized in Table 7-1. The non-local voltages V_{nl} are at the same level with same Pt bar separations. This is because α and J_c are similar between the two studies, and thus λ and C are similar. However, our V_{nl} decreases faster from 2 μm to 9 μm Pt bars separation. This is probably because 1) our 9 μm separation result is obtained between the left and right Pt bars (Figure 7-2), and the third Pt bar in between them may induce additional magnon loss; 2) our YIG thickness is 3 μm, which is on the same order of d, and thus the magnon diffusion is probably more than one dimensional. As also has been demonstrated in [126], the results measured using delta method and lock-in technique are consistent.

Table 7-1 Comparison between our experimental parameters and results with literature reports.

	Our results	**Results in [117]**
YIG thickness	3 μm	200 nm
$\boldsymbol{\alpha}$	0.0003	0.0002
Measurement Method	Delta method	Lock-in technique
$\boldsymbol{J_c}$ **(A/cm^2)**	10^7	6×10^6

V_{nl} **(nV)**	~80 nV (d = 2 μm)	~62.5 nV (d = 2 μm)
	~15 nV (d = 9 μm *)	~25 nV (d = 9 μm)

* Our device structure has 3 parallel Pt bars patterned within one device, as shown in Figure 7-2(a). The left and right Pt bars have a 9 μm separation. V_{nl} in our results is obtained between these 2 Pt bars.

Our experimental efforts on demonstrating magnon diffusion-relaxation transport in YIG sets a measurement platform (i.e., device geometry, configuration, and measurement with the delta method, etc) to study non-local spin transport, which we apply to study possible non-local spin transport in BFO as will be discussed in the next section.

7.3 Non-local Electrical Signals in BFO

Antiferromagnetic insulators are promising for spintronic applications due to their ultrafast magnetic dynamics and robustness to stray fields, and accordingly, non-local spin transport in insulating antiferromagnet is of high research interest. Experimentally, non-local spin transport has been demonstrated in α-Fe_2O_3 [120], [121] with mechanism of antiferromagnetic magnon diffusion and relaxation, and in Cr_2O_3 [22] and graphene [21] showing signature of spin superfluid. In this section, we shall discuss our research efforts on non-local measurements in the Pt/BFO/Pt system, with some preliminary non-local electrical signals possible resulting from spin transport in BFO.

$BiFeO_3$ (BFO) is an insulating multiferroic material with coupled ferroelectric and antiferromagnetic orders [127]. Its local magnetic ordering is G-type antiferromagnetic with a weak canting moment as a result of the magnetoelectric (ME) coupling to the polarization P. This ME coupling also induces a spin cycloid with propagation vector k and a period of around 64 nm, as shown in Figure 7-4. The plane formed by P and k, where the spins rotate, is referred to the

magnetic easy plane of BFO. For a fixed P (i.e., single ferroelectric domain) along [1 1 1] direction, there exist three symmetry equivalent k directions: [1 0 -1], [0 1 -1] and [-1 1 0] [128], each corresponds to a magnetic domain of size up to several hundred microns for a single crystal BFO [129].

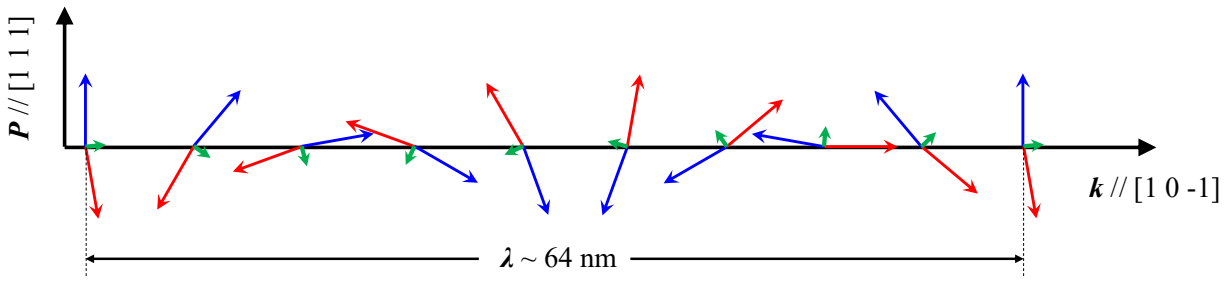

Figure 7-4 Schematic of the spin cycloid in BFO with polarization P along [1 1 1] direction and k along one of the three symmetry directions. Blue and red arrows indicate the canted antiferromagnetic spins. They result in the net magnetic moments indicated by the green arrows, which average to zero within a spin cycloid period.

In our experiments, we use a single crystal BFO sample cut at (1 1 1) face with a single ferroelectric domain as shown in the polarized optical microscope image [130] in Figure 7-5(a). The surface of the sample is polished by a handheld lapping fixture, shown in Figure 7-5(b), and the surface roughness is measured to be around 1 nm by AFM, shown in Figure 7-5(c, d).

We pattern non-local devices as the microscope image shown in Figure 7-6(a), where the orientations of the devices (i.e., Pt bars length direction) are along three directions 120° apart taking into account the three symmetry equivalent magnetic easy-plane orientations. Figure 7-6(b) shows the non-local measurement setup, where we inject current in the left or right Pt bar and measure the non-local voltage in the middle Pt bar by the delta method. Similar to our Pt/YIG/Pt experiments, the Pt bars are 10 nm thick, 80 μm long and 5 μm wide, and the smallest separation between the bars are 2 μm.

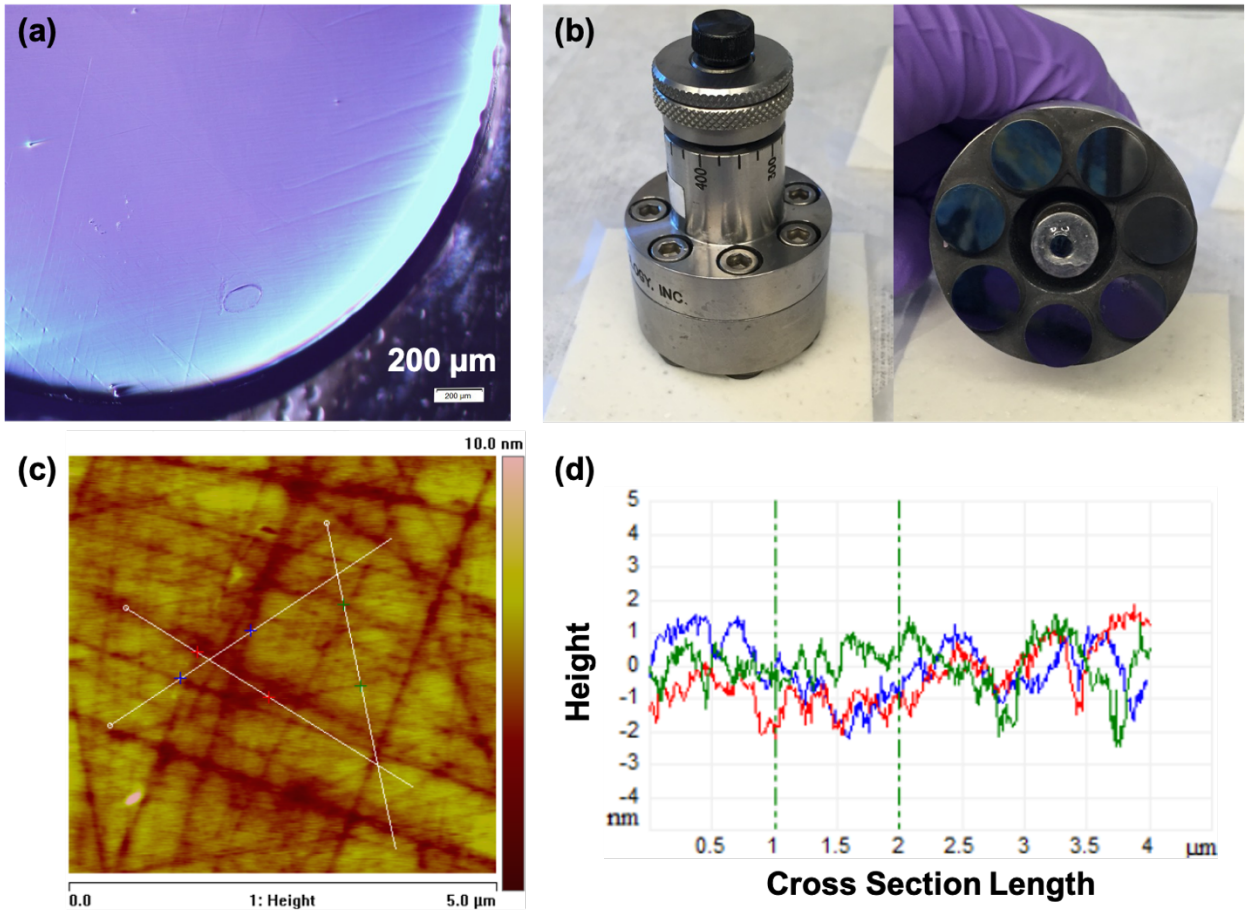

Figure 7-5 (a) Polarized optical microscope image showing one single ferroelectric domain of the (1 1 1) single crystal BFO sample. (b) Lapping fixture to polish the BFO surface. Sample is mounted to the fixture by wax. (c) AFM image of the polished BFO surface with white solid lines drawn on top, corresponding to (d) the cross-section surface profiles that show ~1 nm rms surface roughness.

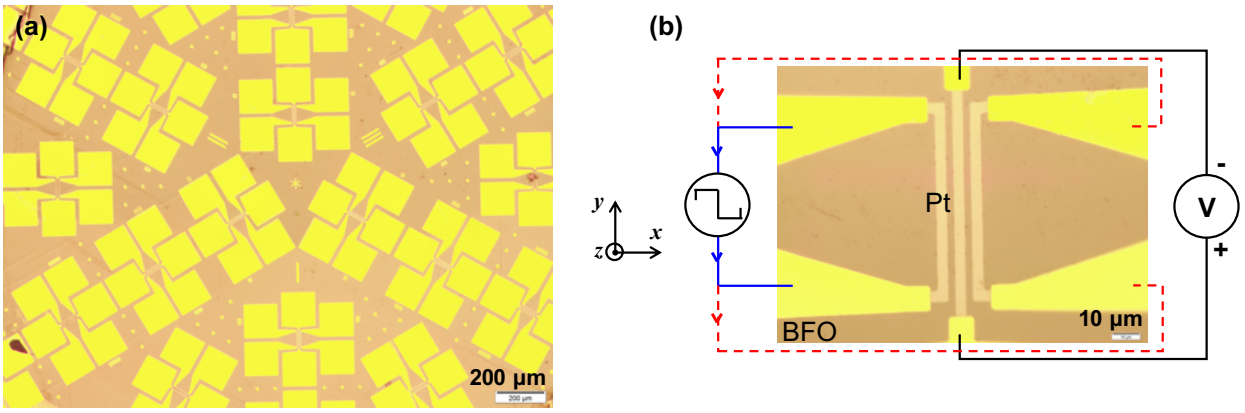

Figure 7-6 (a) Microscope image of the devices for non-local experiments in Pt/BFO/Pt. (b) Measurement setup for the non-local measurements. The current source is connected to the left or right Pt bar, and the nanovoltmeter measures the non-local voltage at the middle Pt bar.

Measurements are first carried in the absence of applied magnetic field, and the typical current dependency of non-local signal V_{nl} for 2 μm Pt bars separation are shown in Figure 7-7(a). The current dependency shows a non-linear "turn on" feature with an onset current in reminiscent of the features in the initial report in YIG [116].

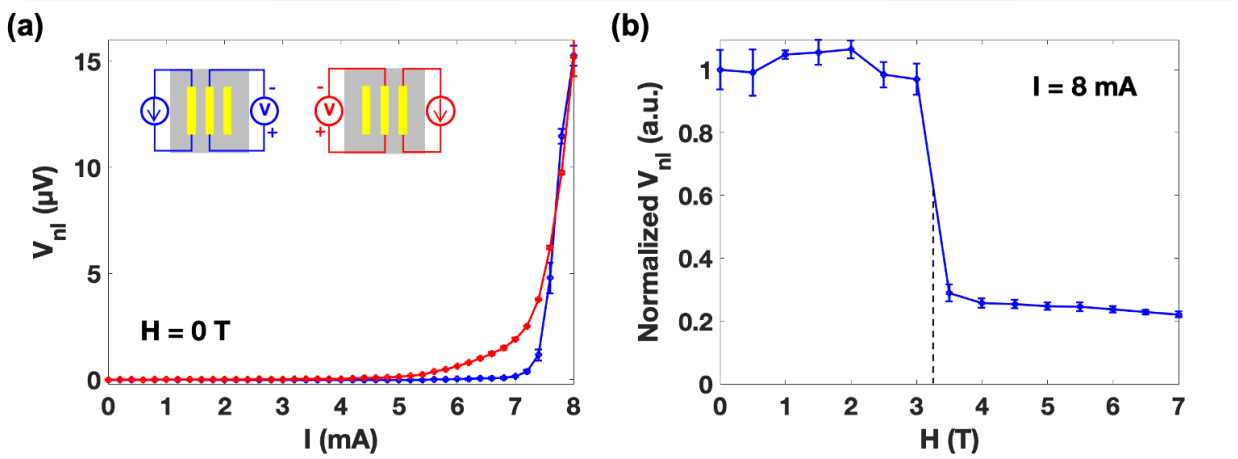

Figure 7-7 (a) Typical results of non-local signals' current dependency in the absence of applied magnetic field. Current is injected in the left Pt bar (blue curve) or the right Pt bar (red curve), and voltage is measured in the middle Pt bar. The Pt bars separation is 2 μm. The non-local signals show a non-linear "turn on" feature with an onset current. (b) Magnetic field dependency of the normalized non-local signal measured with 8 mA injected current. The magnetic field is applied along the sample normal direction [z in Figure 7-6(b)]. Measurements are performed at 300 K. The non-local signal is almost constant up to around 3 T, followed by a clear drop.

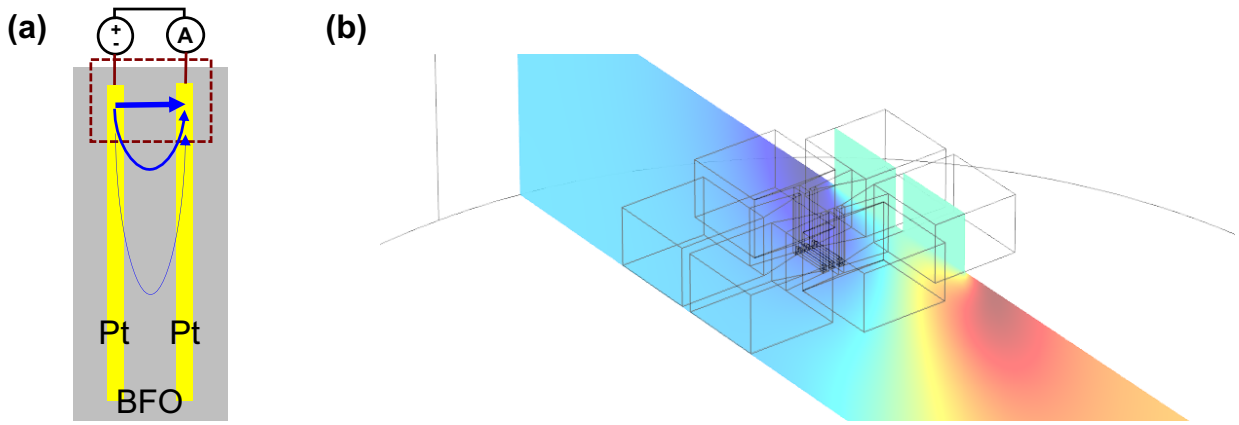

Figure 7-8 Investigation of the leakage as a possible trivial cause for the measured non-local signal. (a) Schematic top view of the measurement setup for leakage measurements [different from the non-local measurement setup in Figure 7-6(b)], with a voltage applied in between the Pt bars and the current in the circuit measured by an ammeter. The blue arrows in indicate the leakage current flow in BFO in the measurements. (b) Simulation in COMSOL to calculate non-local voltage resulting from the leakage current.

Considering non-local electrical signals may result from the trivial leakage current in studies of non-local spin transport in magnetic insulators [131], we perform leakage measurements with the setup in Figure 7-8(a), where a voltage is applied in between the Pt bars and the current in the circuit is measured by an ammeter. The leakage measurements are only carried out after the completion of all non-local measurements to avoid the electric field induced reorientation of the ME domains [132]. In these measurements, a 10 V applied voltage results in less than 0.6 nA measured current. We then use COMSOL to calculate the non-local voltage resulting from the leakage current, shown in Figure 7-8(b). In the COMSOL simulations, we first figure out the resistivity of BFO by simulating the leakage measurement setup [Figure 7-8(a)] to match the leakage current measured in the experiments; we then simulate the non-local measurement setup [Figure 7-6(b)] using the obtained resistivity of BFO to calculate the non-local voltage between the 2 DC contacts induced by the leakage current, which is below 100 nV for 8 mA applied current,

more than 2 orders of magnitudes smaller than our measured non-local signal. Still, more comprehensive experiments should be performed to investigate the Joule heating induced resistance reduction of the single crystal BFO to exclude the leakage current contribution to the non-local signal.

To investigate if the non-local signal is related to spin transport, we perform the magnetic field dependency measurement, as shown in Figure 7-7(b). The field is applied along the sample normal direction (i.e., [1 1 1] direction of BFO). The normalized V_{nl} is almost constant up to 3 T, and then with a clear drop at around 3 T, the signal gradually decreases with further increasing magnetic field. Interestingly, the transition field is close to the transition field from the circular cycloid phase to the anharmonic cycloid phase at around 300 K for BFO [133]. This may indicate that the detected non-local signal is related to the spin transport carried by the spin cycloid in BFO. On the other hand, different devices with the same Pt bars separation show different V_{nl} values, which in the case of spin transport may be due to different devices sitting on different magnetic domains. For this reason, the distance dependency measurement is not meaningful.

It should be noted that the polarity of voltmeter in the non-local measurement setup for BFO [Figure 7-6(b)] is different from that of the conventional non-local spin transport, and the limited devices that we measure result in positive V_{nl}. This may either 1) suggest different spin injection and detection mechanisms from the typical non-local spin transport experiments, or 2) result from the magnetic domain configurations where the devices locate. More measurements and comprehensive analysis of more devices with different configurations are needed to understand the non-local signal measured in Pt/BFO/Pt and, if spin transport based, the underlying mechanism.

7.4 Conclusion and perspectives

In this chapter, we discuss our research efforts on non-local spin transport in magnetic insulators. We first use delta method to measure and demonstrate non-local spin transport in Pt/YIG/Pt. The results are consistent with the literature reports. We then apply the delta method to measure non-local signals in Pt/BFO/Pt and observe a non-linear current dependency of the non-local voltages and a field dependency which may be related to the transition from circular to anharmonic spin cycloid phase in BFO. These results, however, are preliminary based on our limited devices and samples. More experiments (e.g., non-local measurements on Pt/BFO/Cu and Pt/BFO/Ta, comprehensive temperature dependent resistance measurements, etc) and analysis are necessary to exclude trivial causes for the non-local signals and to understanding the underlying mechanism.

8 Voltage Control of Superfluid Spin Transport in Magnetic Josephson Junction

As discussed in Section 2.4, spin superfluidity refers to an ability of a magnetic system with U(1) spin-rotational symmetry to support dissipationless spin transport. Recent theoretical and experimental progress focus on electrical generation and detection of the spin superfluid. In this chapter, we propose electrical control of such superfluid spin transport in a gated easy-plane magnet. In particular, we demonstrate that the system can be tuned between two regimes, a DC regime and an AC regime: the DC regime features a time independent superfluid-like spin current, while in the AC regime an oscillatory spin current flows, which is marked by a periodic appearance of phase slips in the gated region. These results are analogous to the current-induced transition between the "superconducting" state and the "voltage" state of one-dimensional superconducting Josephson Junctions. Our findings lead to practical applications, including low dissipative spin transistor and tunable spintronic oscillators.

8.1 Introduction

As introduced in Chapter 1, magnons have attracted significant interest due to the promise of transporting spin in the absence of Ohmic loss [10]. Particularly, experimental schemes for generation, detection, and control of magnon spin currents by electrical [116]–[120] and thermal [134]–[137] means have been developed. However, as mentioned in Chapter 7, these experiments have primarily explored the regime where the spin current is carried by the exponentially decaying

incoherent magnons. More recently, magnets with easy-plane anisotropy have emerged as alternate candidates for long-distance transport of spin. This regime is inspired from superfluids, where a long-distance coherent spin current is carried by the gradient of the U(1) order parameter [19], [20], [138]–[147]. While the identification of easy-plane magnetic systems as spin superfluids (see Section 2.4) was done as early as in 1969 [28], [148], the recent renewed interest originates from the experimental ability to interconvert spin currents into electrical signals in generic magnetic systems by engineering the spin-orbit interaction [17], [149]–[154]. Theoretical works have proposed the realization of spin superfluids in nonlocal spin injection and detection geometry, where spin current with spin polarization perpendicular to the easy-plane is injected to and detected from the spin-superfluid medium, via magnetic tunnel junction [138], [139], spin valve [141], or by spin Hall effect (SHE) and inverse spin Hall effect (ISHE) such as in heavy metals [19], [20], [142], [143]. As previously mentioned in Chapter 7, experimental signatures of spin superfluidity have been observed in antiferromagnetic insulators via nonlocal spin transport measurements [21], [22].

While the above theoretical and experimental progress provide schemes to electrically generate and detect superfluid-like spin currents, the ability to control the flow of such spin currents via electrical knobs is largely missing. The central goal of this work is to fill this gap. For this purpose, we combine the well-established ability to control the superflow of charges in superconducting wires via defining weaker superfluid regions (the so-called weak links [19]) [155]–[157] with the capability of electrically tuning easy-plane anisotropy via spin-orbit interaction.

[19] In addition to a region with weakened superconductivity, the weak link can also be a thin insulating or even a normal metal.

The proposed system is depicted in Figure 8-1(a), where an easy-xy-plane magnet is gated so that by applying a gate voltage, the magnetic anisotropy can be lowered inside the gate region. Such magnetic anisotropy tuning can be realized via the voltage-controlled magnetic anisotropy (VCMA) effect [158]. The magnet is thus divided into three regions, with the two strong easy-plane regions (referred to as Region I and III) as the spin superfluid banks, and the weak easy-plane region (referred to as Region II) as the "weak link". A superfluid spin current is injected into the system from the left side and is ejected from the system on the right side. This spin supercurrent gets modified in the gate region, and therefore its decay deviates from the normal algebraic fashion.

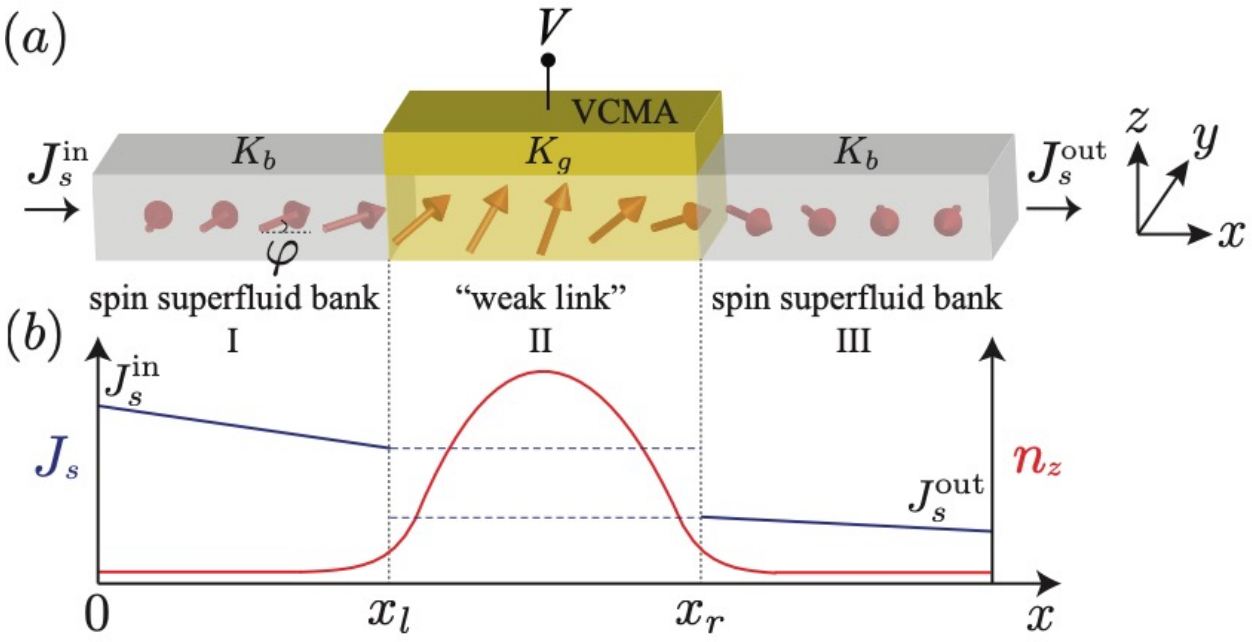

Figure 8-1. A gated easy-xy-plane magnet with gate region magnetic anisotropy K_g lowered from its uniform background value K_b through the VCMA effect. The subscripts "g" and "b" indicate the gate region and the background region, respectively. A superfluid spin current ($\propto \nabla\varphi$), featuring a global in-plane precession of magnetic texture, enters the magnet with value J_s^{in} and exits the magnet with value J_s^{out}. This spin current gets modified by canted spins ($n_z > 0$) in the gate region due to lowered easy-plane magnetic anisotropy, and therefore its decay deviates from the normal algebraic fashion, such that the output spin current J_s^{out} can be tuned by the gate.

8.2 Model

Without loss of generality, we focus our discussions on a ferromagnet, with the background easy-plane anisotropy K_b (in Region I and III), and a lowered gate region magnetic anisotropy K_g (in Region II). Similar to the treatment for a spatially homogeneous easy-plane ferromagnet discussed in Section 2.4, the free energy of the system can be written as $F = \int d^3\boldsymbol{x}[A\left(\nabla \boldsymbol{n}(\boldsymbol{x})\right)^2 + K(\boldsymbol{x})n_z(\boldsymbol{x})^2]/2$, where A, $K(\boldsymbol{x})$, $\boldsymbol{n}$ represent the magnetic exchange stiffness, the spatially varying uniaxial anisotropy coefficient, and the unit vector along the U(1) order parameter direction. Here, $K(\boldsymbol{x})$ takes the value of K_b inside the Region II and K_g inside Region I and III, with $K_b > 0$ ensuring the easy-plane anisotropy for the spin superfluid banks. The subscripts "g" and "b" indicate the gate region and the background region, respectively.

8.3 Spin Dynamics

The magnetic dynamics is governed by the Landau-Lifshitz-Gilbert (LLG) equation $(1 + \alpha \boldsymbol{n} \times)\dot{\boldsymbol{n}} = -\boldsymbol{n} \times \partial_s F$, where α is the dimensionless Gilbert damping constant, $s(=\frac{M_S}{\gamma})$ is the saturated spin density and $\boldsymbol{n}$ can be parameterized by its azimuthal angle φ and its out-of-plane projection n_z as $\boldsymbol{n} = (\sqrt{1 - n_z^2}\cos\varphi, \sqrt{1 - n_z^2}\sin\varphi, n_z)$. As discussed in [20], [159] and in Section 2.4, the LLG equation can be linearized and solved analytically in the strong-anisotropy and long-wavelength limit. The collective spin current $\boldsymbol{J_s}(\boldsymbol{x}) \equiv -A\nabla\varphi(\boldsymbol{x})$ carries spin angular momentum along z-axis. As discussed in Section 2.4, in a ferromagnet with homogeneous anisotropy, namely $K_g = K_b \equiv K$, the steady-state solutions feature superfluid spin transport with a uniform small canting of the order parameter out of the easy plane (i.e., $n_z(\boldsymbol{x}) = \text{const} \equiv n_z$ [20])

[20] In the linear regime following the linearization process of the LLG equation, $n_z \approx 0$.

and a global precession of a spiraling magnetic texture in the easy plane (i.e., $\varphi(\boldsymbol{x}, t) = \varphi(\boldsymbol{x}) + Kn_z t/s$). The Gilbert damping dissipates the spin angular momentum at a rate of $\alpha\partial_t\varphi$ per unit length, leading to a linearly decaying spin current along x-axis.

In situations where K becomes inhomogeneous, as K_g is lowered from the uniform background value K_b, the system gradually deviates from the strong-anisotropy limit, which eventually invalidates the results obtained by direct linearization of the LLG equation as discussed above. According to the Landau criterion [28], the spin superfluid state becomes unstable when $K < J_s^2/A$, and thus we would expect the system to evolve into a new dynamic phase. Considering the nonlinear nature of the LLG equation and the consequent difficulties in finding the solutions analytically, we carry out micromagnetic simulations using the LLG Micromagnetics Simulator [45] (discussed in Section 3.2) to solve the LLG equation numerically, which will be discussed in the following section.

8.4 Micromagnetic Simulations

As shown schematically in Figure 8-1, we implement in the simulations a structure with a one-dimensional ferromagnetic spin chain of length 900 nm and saturation magnetization M_s = 800 emu/cm^3. The exchange stiffness A is set to be 2.1 μerg/cm uniformly along the spin chain, and the background uniaxial magnetic anisotropy coefficient K_b is set as 2×10^6 erg/cm^3, with the easy plane set to be xy-plane such that spin superfluid can be realized with z-polarized spin injection. For simplicity, the thermal magnon contributions are excluded by setting the temperature to zero in the simulations. The leftmost spin is set as the spin injector by specifying a Slonczewski-type spin-torque [46] to realize the z-polarized spin injection. The boundary condition on the right end is set to be the exchange boundary condition. The center of the spin chain from x_l = 400 nm to x_r

= 500 nm is set as the gate region, with the magnetic anisotropy K_g set to be different values from $-K_b$ to K_b, mimicing the magnetic anisotropy tuning through the VCMA effect. For fast relaxation to steady state, the damping parameter α is chosen to be 0.1. Based on these configurations, spatial distribution and time evolution of the magnetization and thus $\boldsymbol{n}$ can be calculated in the micromagnetic simulations as $\boldsymbol{n}(\boldsymbol{x}, t)$, whose azimuthal angle $\varphi(\boldsymbol{x}, t)$ can be extracted and used to calculate the spin super current $\boldsymbol{J_s}(\boldsymbol{x}, t)$.

8.5 Phase Diagram

From the time-domain characteristics of spin dynamics, we can identify two distinct phases, DC phase and AC phase, by tuning the gate region magnetic anisotropy under different input spin current. The phase diagram is plotted in Figure 8-2 as a function of normalized unitless gate region anisotropy $\widetilde{K} \equiv K_g/K_b$ and input spin current $\tilde{J}_s^{\text{in}} \equiv J_s^{\text{in}}/\sqrt{K_b A}$, respectively.

The DC phase is superfluid-like, with similar signatures to that of the normal spin superfluid discussed in the previous sections, featuring a time independent globally uniform precession of the order parameter within the easy plane in Region I and III, which supports an algebraically decaying spin current. Due to the lowered gate region easy-plane magnetic anisotropy, however, the order parameter in Region II slightly cants out of the easy plane.

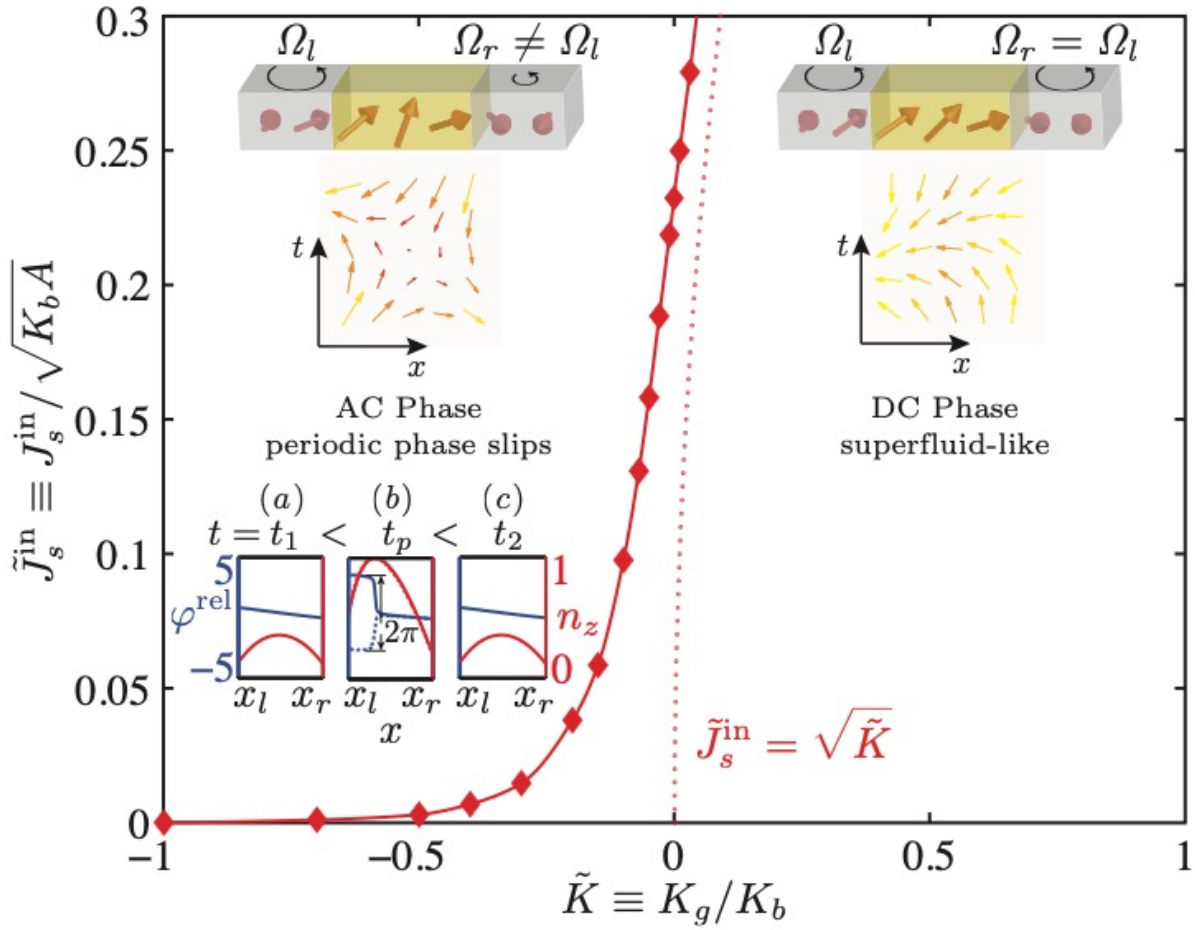

Figure 8-2. Dynamic phase diagram, with the red solid curve indicating the boundary between two distinct phases. The DC phase is superfluid-like, featuring a globally uniform precession (i.e., $\Omega_r = \Omega_l$, as shown in the top right inset) of the spiraling magnetic texture. With weakening gate region easy-plane anisotropy, at fixed $\tilde{J}_s^{in}$, the system evolves into the AC phase, where the magnetic texture precessions on two sides of the gate region are out of synchronization (i.e., $\Omega_r \neq \Omega_l$, as shown in the top left inset), which leads to the buildup of the magnetic texture winding in the gate region. Periodic phase slip events occur to relax the winding, with the gate region order parameter periodically canting out of the plane completely, creating vortices in Euclidean spacetime of magnetic order parameters. The inset (a-c) shows the evolution of gate region $\varphi^{rel}(x) \equiv \varphi(x) - \varphi(x_l)$ and n_z in the dynamic sequence of a phase slip event

[based on simulation results with $\tilde{J}_s^{in} = 0.05$, $\widetilde{K} = -0.2$, t_1(= 25.2 ns) < t_p(= 41.7 ns) < t_2(= 46.5 ns)]. The red dotted line corresponds to the calculated critical condition based on the "local" Landau criterion applying to the gate region[21].

In the AC phase, the system undergoes a sequence of dynamic events, as captured from simulation results shown in inset (a-c) of Figure 8-2. In all of the figures, both $\varphi^{\mathrm{rel}}(x) \equiv \varphi(x) - \varphi(x_l)$ and n_z across the gate region are plotted. In the presence of the gate region with lowered magnetic anisotropy, the magnetic texture precessions on two sides of the gate region are out of synchronization, and the precession rate (Ω_r) in Region III is slower than that in Region I (Ω_l)[22]. The system starts from an equilibrium state, where the difference of φ^{rel} across the gate $\Delta\varphi \equiv \varphi^{\mathrm{rel}}(x_r) - \varphi^{\mathrm{rel}}(x_l)$ is small [shown in inset (a) of Figure 8-2]. Then $\Delta\varphi$ builds up as a result of different precession rates of the magnetic textures, and n_z deviates from its equilibrium value as the order parameter in the gate region further cants out of the easy plane. At the instance of $|n_z|$ reaching 1, $\Delta\varphi$ reaches its maximum, which is immediately followed by the phase φ^{rel} bending back upon itself with $\Delta\varphi$ slipping by 2π, as shown in inset (b) of Figure 8-2. This instance is a phase slip event, after which n_z gradually reduces to the equilibrium value again, as $\Delta\varphi$ smooths out (inset (c) of Figure 8-2). The system finally recovers the initial configurations, from where the above dynamic events will repeat themselves. This phenomenon resembles the AC Josephson effects in superconductors coupled by a "weak link" [155], [156]. Similar to superconducting wires, the phase slips in easy-plane magnetic wires correspond to vortices of the magnetic order parameter in Euclidean spacetime, as shown in the inset in Figure 8-2.

[21] Here, "local" Landau criterion means that we take only the local gate region anisotropy to calculate the critical current, even if the magnetic anisotropy is spatially inhomogeneous.
[22] The precession rates in Region III and Region I can be parametrized as Ω_r and Ω_l, respectively, as will be discussed in Section 8.6.

The phase transition can be interpreted in terms of the system stability. Starting from the normal spin superfluid with homogeneous magnetic anisotropy (i.e., $\widetilde{K} = 1$), the gate region spins gradually cant out of the easy plane, with increasing input spin current or weakening gate region easy-plane anisotropy, to maintain the system metastable in the DC phase. As the system transits into the AC phase, the system is unstable even with fully canted gate region spins, and consequently it evolves into a lower-energy state through introduction of periodic singularities in the order parameter (i.e., phase slip events), which also relaxes the winding of magnetic texture in the gate region.

The Landau criterion provides a measure of the DC and AC phase transition boundary. The critical condition, corresponding to the "local" Landau criterion in the critical spin supercurrent in Region II, $J_s^{\mathrm{critical}} \equiv J_s^{\mathrm{in}} = \sqrt{K_g A}$ is plotted as a red dotted line in the phase diagram in its normalized unitless form $\tilde{J}_s^{\mathrm{critical}} \equiv \tilde{J}_s^{\mathrm{in}} = \sqrt{\widetilde{K}}$. The "local" Landau criterion dictates the critical supercurrent of the "weak link" [23]. It should be noted that this "local" Landau criterion boundary is on the right side of the actual boundary between the DC and AC phase, indicating the critical supercurrent of entire system is higher than that of the "weak link". This can be explained by the fact that the superfluid banks coupling to the "weak link" on both sides help relieve the canting of the gate region spins out of the easy plane, and thus results in the enhanced critical current.

[23] Here, we discuss the critical condition in terms of the critical current, that is, for a fixed $\widetilde{K}$, the system changes from the DC regime to the AC regime when $\tilde{J}_s^{in}$ is above the critical value, as shown in the phase diagram Figure 8-2. Similar argument can be made for the critical magnetic anisotropy, that is, for a fixed $\tilde{J}_s^{in}$, the system transforms from the DC regime to the AC regime when $\widetilde{K}$ is below the critical value.

8.6 Phenomenological Model

To interpret the results from micromagnetic simulations, we derive a phenomenological model based on the conservation laws of angular momentum and energy. As discussed in the previous section, the precession of the spiraling magnetic texture is uniform within Region I and Region III, and the precession frequencies can be parameterized as Ω_l and Ω_r in Region I and III, respectively. Assuming phase slips dissipate the angular momentum and energy of the entire system at a frequency f (i.e., frequency of the phase slip events), and each phase slip event is associated with angular momentum loss of γ_{ps} and energy loss of E_{ps}. The conservation laws of angular momentum and energy lead to the following equations, respectively:

$$J_s^{\text{in}} - J_s^{\text{out}} = \gamma_{ps} f + \gamma_l \langle \Omega_l \rangle + \gamma_r \langle \Omega_r \rangle \tag{8.1}$$

$$J_s^{\text{in}} \langle \Omega_l \rangle - J_s^{\text{out}} \langle \Omega_r \rangle = E_{ps} f + \gamma_l \langle \Omega_l \rangle^2 + \gamma_r \langle \Omega_r \rangle^2 \tag{8.2}$$

where $\gamma_l \doteq \alpha s L_l$ and $\gamma_r \doteq \alpha s L_r$ are the loss coefficients in Region I and III [24], and $\langle \Omega_l \rangle$ and $\langle \Omega_r \rangle$ represent the time-averaged precession frequencies at the left Region I and the right Region III for one phase slip cycle, respectively. The terms on the left-hand side of Equation (8.1) and (8.2) correspond to the net angular momentum/energy injections into the system, while the terms on the right hand side correspond to the dissipations. To be more specific, the first dissipation terms on the right hand side of Equation (8.1) and (8.2) indicate the loss due to phase slip events, and the last two dissipation terms indicate the ordinary loss due to Gilbert damping. As discussed previously, the phase slip events occur when the built-up relative phase difference across Region

[24] The exact expressions of the loss coefficient are $\gamma_l = \alpha s(1 - n_{l,z}^2) L_l$ and $\gamma_r = \alpha s(1 - n_{r,z}^2) L_r$, with $n_{l,z}$ and $n_{r,z}$ parameterizing the z-projection of $\boldsymbol{n}$ in Region I and III. In case of the strong background easy-plane anisotropy supporting the spin superfluid banks, it follows that $n_{l,z} \doteq 0$ and $n_{r,z} \doteq 0$ (i.e., only a small canting of the order parameter out of the easy-plane), which leads to the approximate expressions.

I and III reaches a maximum value, then one phase slip event relaxes the phase difference by 2π, or equivalently, the relative phase difference buildup within one phase slip is 2π. This can be enforced by the following equation [25]:

$$\langle \Omega_l \rangle - \langle \Omega_r \rangle = 2\pi f \tag{8.3}$$

In the DC phase, no phase slip event occurs, and thus $f = 0$, which leads to $\langle \Omega_l \rangle = \langle \Omega_r \rangle \equiv \Omega$. As a result, Equation (8.1) and (8.2) can be reduced to $J_s^{\text{in}} - J_s^{\text{out}} = (\gamma_l + \gamma_r)\Omega_r \equiv \gamma\Omega$, with $\gamma \doteq \alpha s(L_l + L_r)$. This leads to $\Omega = (J_s^{\text{in}} - J_s^{\text{out}})/[\alpha s(L_l + L_r)]$, which is consistent with the results in [19], [20], [159].

In the phase harboring periodic phase slip events, f is greater than 0, which can be solved from Equation (8.1) and (8.2). For simplicity, we assume $J_s^{\text{out}} = 0$, which is consistent with the exchange boundary at the right end in the simulations, and $L_l = L_r \equiv L/2$, which results in $\gamma_l = \gamma_r \equiv \gamma/2$. From Equation (8.1), (8.2) and (8.3), we can calculate the phase slip rate and precession frequencies to be $f = (\eta J_s^{\text{in}} - E_{ps})/\tilde{\gamma}$ and $\langle \Omega_r \rangle = [\eta E_{ps} - 2\pi(\eta - \pi)J_s^{\text{in}}]/\tilde{\gamma}$ (with $\langle \Omega_l \rangle = \langle \Omega_r \rangle + 2\pi f$), where $\eta = \frac{\gamma_{ps}}{\gamma} + \pi^2\gamma$. We consider γ_{ps} and E_{ps} as intrinsic characteristics of phase slips. The onset of phase slip events occurs at $f > 0$, which leads to the critical condition of $J_s^{\text{in}} = E_{ps}/\eta \equiv J_c$. Thus, we obtain the expressions of phase slip frequency and time-averaged precession frequencies of the spin texture as follows [26]:

$$f = \begin{cases} \eta(J_s^{\text{in}} - J_c)/\tilde{\gamma}, & J_s^{\text{in}} > J_c \\ 0, & J_s^{\text{in}} \le J_c \end{cases} \tag{8.4}$$

[25] We do not consider the spin pumping on two ends in our phenomenological model to keep it consistent with our simulation model. The inclusion of these effects would not jeopardize the central results from our model.
[26] We enforce $f = 0$ below J_c, in the superfluid-like phase, where phase slip events are absent.

$$\langle \Omega_r \rangle = \begin{cases} [\eta^2 J_c - 2\pi(\eta - \pi) J_s^{\text{in}}]/\tilde{\gamma}, & J_s^{\text{in}} > J_c \\ J_s^{\text{in}}/(2\gamma), & J_s^{\text{in}} \leq J_c \end{cases} \tag{8.5}$$

Based on the conventional detection schemes via spin pumping and ISHE, the time-averaged output signal as well as spin current is proportional to the precession frequencies (i.e., $\langle \tilde{J}^{\text{out}} \rangle \propto \langle \Omega_r \rangle$). In micromagnetic simulations, $\langle \tilde{J}_s^{\text{out}} \rangle$ is calculated as the time-averaged spin current in Region III at x = 800 nm [27]. The critical current J_c (for each given magnetic anisotropy) can be extracted from the critical boundary curve in the phase diagram (Figure 8-2), then applied to Equation (8.4) and fit with the phase slip rates $\hat{f}$ and the time-averaged spin current $\langle \tilde{J}_s^{\text{out}} \rangle$ from simulations to obtain γ_{ps} and γ [28].

As shown in Figure 8-3, the results from our analytical expressions agree well with the numerical results: the phase slip events turn on below certain normalized gate anisotropy $\widetilde{K}$ for different $\tilde{J}_s^{\text{in}}$, $\hat{f}$ increases and saturates with further reduced $\widetilde{K}$. From the fittings, $\gamma \sim 0.43 - 0.45$ nerg·s/cm^2 and $\gamma_{ps} \approx 0.02$ nerg·s/cm^2 for different spin current drive $\tilde{J}_s^{\text{in}}$. We note that γ calculated from $\alpha s L$ yields 0.41 nerg·s/cm^2, with L = 900 nm (i.e., the entire length of the ferromagnet), which is close to the fitting results. The independence of γ_{ps} on $\tilde{J}_s^{\text{in}}$ justifies that γ_{ps} is an intrinsic characteristics of the phase slips.

[27] Such implementation of detection in micromagnetic simulations is reasonable as discussed in [160], where the spin current reaching the ends are drained by the spin sinks.

[28] Here, $\hat{f}$ is the dominant frequency of the phase slip events, obtained from Fourier analysis of the simulation results. We introduce universal proportionality coefficients for different $\tilde{J}_s^{\text{in}}$ in fitting of $\langle \Omega_r \rangle$ with $\langle \tilde{J}_s^{\text{out}} \rangle$.

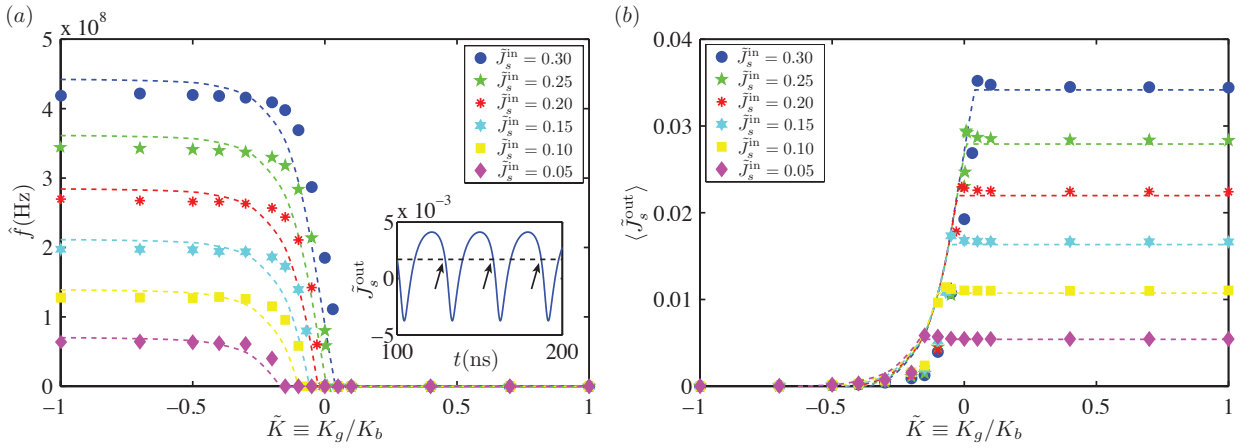

Figure 8-3 (a) Dominant frequency $\hat{f}$ of the oscillating output spin current $\tilde{J}_s^{out}$. For a given $\tilde{J}_s^{in}$, $\hat{f}$ remains zero in the DC phase until $\widetilde{K}$ lowers below the critical value, where the system transits into the AC phase. With further lowering $\widetilde{K}$, $\hat{f}$ rapidly increases to a saturation value. Dashed lines plot the fitted analytical expression [Equation (8.4)]. Inset shows the time-varying output spin current with the arrows denoting the instances of phase slip events (based on simulation results with $\tilde{J}_s^{in} = 0.05$, $\widetilde{K} = -0.2$). (b) Transfer characteristics of the voltage-controlled magnetic Josephson junction. For a given $\tilde{J}_s^{in}$, the time-averaged output spin current $\langle \tilde{J}_s^{out} \rangle$ remains almost constant in the DC phase, until $\widetilde{K}$ lowers below the critical value. In the AC phase, $\langle \tilde{J}_s^{out} \rangle$ rapidly drops to zero. Dashed lines plot the fitted analytical expression [Equation (8.5)]. In these two figures, the fitting parameters γ (i.e., the ordinary loss due to Gilbert damping) are 0.45 nerg·s/cm^2, 0.45 nerg·s/cm^2, 0.45 nerg·s/cm^2, 0.44 nerg·s/cm^2, 0.44 nerg·s/cm^2, 0.43 nerg·s/cm^2 for unitless input spin current $\tilde{J}_s^{in}$ of 0.05, 0.10, 0.15, 0.20, 0.25, 0.30, respectively, and γ_{ps} (i.e., the angular momentum loss during a single phase slip event) are 0.02 nerg·s/cm^2 for different $\tilde{J}_s^{in}$.

These results are analogous to the current-induced transition between the "superconducting" state and the "voltage" state in one dimensional superconducting Josephson Junctions [29] [156], [157]. Such characteristics of our spin superfluid Josephson junction combined with the tunability

[29] In the current-induced transition of superconducting Josephson junctions, when the current exceeds the critical value, the voltage developed resistively across the weak link, accompanied by the periodic phase-slip events with time-domain oscillating supercurrent.

enabled by the VCMA effect renders potential device applications as discussed in the following section.

8.7 Device Application

By adding the spin injector and detector, such as in the non-local spin transport geometry shown in Figure 7-1, to two ends of the proposed structure (Figure 8-1) functioning as the source and the drain, respectively, the magnetic Josephson junction can be made into a low dissipative spin transistor. Spin injection is realized through SHE at the source and spin detection through ISHE at the drain.

As shown in Figure 8-3(b), spin transport is efficient in the superfluid-like phase, while output current is almost zero deep in the AC phase due to dissipation via the phase slip events. For a fixed input spin current, the spin transistor operates between $K_g = K_b$ and $K_g = -K_b$ (near the spin transport cutoff), whose values may be controlled electrically through the gate voltage via the VCMA effect.

Additionally, as shown in inset of Figure 8-3(a), the output spin current oscillates in the AC phase. In the simulations, this time-domain oscillation becomes more sinusoidal with increasing $\tilde{J}_s^{\text{in}}$ or decreasing $\widetilde{K}$. Operating in the AC phase, the magnetic Josephson junction can be implemented as a spintronic oscillator in close analogy to superconducting Josephson Junction-based oscillators. Similar spin oscillators based on spin-Josephson effects have been proposed [161], [162]. The frequency of our magnetic Josephson junction is tunable by the gate voltage for fixed input spin current.

On another note, spin oscillators have been proposed based on spin-Josephson effects [161], [162]. Operating in the AC phase, the spin superfluid Josephson junction can be implemented as a tunable

low dissipation spintronic oscillator in close analogy with the superconducting Josephson Junction-based oscillator.

8.8 Conclusion

In this chapter, we discuss our proposed tunable magnetic analogy of Josephson Junctions based on spin superfluid in a gated easy-plane magnet. We investigate by numerical simulations and demonstrate that by tuning the gate region anisotropy via VCMA, the system can be tuned between a DC regime, featuring a time independent superfluid-like spin current, and an AC regime with an oscillatory spin current accompanied by periodic phase slip events in the gated region. These phenomena are analogous to the current-induced transition between the "superconducting" state and the "voltage" state of one-dimensional superconducting Josephson Junctions. The characteristics of the magnetic Josephson Junctions can be quantitatively explained by our phenomenological model based on conservation laws. Our proposed system may lead to practical applications, such as low dissipative spin transistor and tunable spintronic oscillators.

9 Conclusion

In conclusion, we first introduce spin waves as the information carrier free from Ohmic losses in the energy-efficient technologies based on magnon spintronics and the need to reduce losses due to magnetic damping for practical applications, which are the motivations behind the research conducted for this dissertation. We then describe relevant fundamental theory to help understand this dissertation, including basic magnetism, magnetic dynamics and its governing equation, LLG equation, which lay the foundations for classical theory on spin waves (magnons), as well as spin superfluid in easy-plane magnets, and SHE as the source of spin currents for amplification of spin waves and excitation of incoherent magnons or spin superfluid. The relevant numerical methods and experimental methods used for the studies are also discussed.

For spin waves inductively excited, we present the work on SOT induced damping compensation in YIG based on 1) the conventional spin-wave amplification configuration, where TI replaces 5d transition metals to provide the SOT with an improved efficiency, and 2) the "comb" configuration generating a SOT wave to more efficiently transfer energy to the spin waves to amplify them. Future research efforts may include further optimizations of the interface between magnetic insulators and SOC material, including maximizing the surface state contribution in YIG/TI systems by gating [163] or TI composition tuning [164], insertion of antiferromagnetic layer to enhance spin transparency [165], [166], etc, to enhance the SOT efficiency. Specifically, for the "comb" configuration, a comprehensive theory for the coupled-wave interaction between the SOT wave and spin waves, with the combined effect of SOT and spin pumping as the source of the interaction, can be developed to guide the design optimizations. Furthermore, optimizations of the

"comb" structure, including the introduction of the pitch modulation to broaden or to customize the operating bandwidth, and careful design of the matching networks to improve efficiency of rf current injection to the "comb", etc, may greatly enhance the device performance.

We then present our results on non-local spin transport experiments in magnetic insulators, where spin injection and detection are based on SHE and ISHE. The spin carrying medium in the non-local spin transport scheme can be spin superfluid, which has minimal dissipation compared with the exponentially decaying magnons. We finally present the work on electrical control of the spin superfluid transport for practical device applications. Future research efforts may emphasize on realizing superfluid non-local spin transport at room temperature. Specifically, for the non-local experiments in BFO/Pt system, additional experiments (e.g., temperature dependent measurements, magnetic field dependent measurements with fine H-field steps, etc) and comprehensive analysis are necessary to understand the underlying mechanism for the non-local signal. Additionally, different easy-plane magnetic insulators as well as engineered easy-plane magnetic structures [167] that can support the spin superfluid can be explored to demonstrate spin superfluid at room temperature.

References

[1] F. Bloch, “Zur Theorie des Ferromagnetismus,” *Z. Für Phys.*, vol. 61, no. 3, pp. 206–219, Mar. 1930, doi: 10.1007/BF01339661.

[2] J. M. Owens, J. H. Collins, and R. L. Carter, “System applications of magnetostatic wave devices,” *Circuits Syst. Signal Process.*, vol. 4, no. 1, pp. 317–334, Mar. 1985, doi: 10.1007/BF01600088.

[3] J. D. Adam, “Analog signal processing with microwave magnetics,” *Proc. IEEE*, vol. 76, no. 2, pp. 159–170, Feb. 1988, doi: 10.1109/5.4392.

[4] S.-K. Kim, K.-S. Lee, and D.-S. Han, “A gigahertz-range spin-wave filter composed of width-modulated nanostrip magnonic-crystal waveguides,” *Appl. Phys. Lett.*, vol. 95, no. 8, p. 082507, Aug. 2009, doi: 10.1063/1.3186782.

[5] J. D. Adam and S. N. Stitzer, “A magnetostatic wave signal-to-noise enhancer,” *Appl. Phys. Lett.*, vol. 36, no. 6, pp. 485–487, Mar. 1980, doi: 10.1063/1.91516.

[6] J. D. Adam and S. N. Stitzer, “Frequency selective limiters for high dynamic range microwave receivers,” *IEEE Trans. Microw. Theory Tech.*, vol. 41, no. 12, pp. 2227–2231, Dec. 1993, doi: 10.1109/22.260710.

[7] V. V. Kruglyak, S. O. Demokritov, and D. Grundler, “Magnonics,” *J. Phys. Appl. Phys.*, vol. 43, no. 26, p. 264001, Jul. 2010, doi: 10.1088/0022-3727/43/26/264001.

[8] S. A. Wolf *et al.*, “Spintronics: A Spin-Based Electronics Vision for the Future,” *Science*, vol. 294, no. 5546, pp. 1488–1495, Nov. 2001, doi: 10.1126/science.1065389.

[9] I. Žutić, J. Fabian, and S. Das Sarma, “Spintronics: Fundamentals and applications,” *Rev. Mod. Phys.*, vol. 76, no. 2, pp. 323–410, Apr. 2004, doi: 10.1103/RevModPhys.76.323.

[10] A. V. Chumak, V. I. Vasyuchka, A. A. Serga, and B. Hillebrands, “Magnon spintronics,” *Nat. Phys.*, vol. 11, no. 6, Art. no. 6, Jun. 2015, doi: 10.1038/nphys3347.

[11] S. O. Demokritov *et al.*, “Bose–Einstein condensation of quasi-equilibrium magnons at room temperature under pumping,” *Nature*, vol. 443, no. 7110, Art. no. 7110, Sep. 2006, doi: 10.1038/nature05117.

[12] A. A. Serga *et al.*, “Bose–Einstein condensation in an ultra-hot gas of pumped magnons,” *Nat. Commun.*, vol. 5, no. 1, Art. no. 1, Mar. 2014, doi: 10.1038/ncomms4452.

[13] P. Gambardella and I. M. Miron, “Current-induced spin–orbit torques,” *Philos. Trans. R. Soc. Math. Phys. Eng. Sci.*, vol. 369, no. 1948, pp. 3175–3197, Aug. 2011, doi: 10.1098/rsta.2010.0336.

[14] Z. Wang, Y. Sun, M. Wu, V. Tiberkevich, and A. Slavin, “Control of spin waves in a thin film ferromagnetic insulator through interfacial spin scattering,” *Phys. Rev. Lett.*, vol. 107, no. 14, p. 146602, 2011, doi: 10.1103/PhysRevLett.107.146602.

[15] E. Padrón-Hernández, A. Azevedo, and S. M. Rezende, “Amplification of spin waves in yttrium iron garnet films through the spin Hall effect,” *Appl. Phys. Lett.*, vol. 99, no. 19, p. 192511, 2011, doi: 10.1063/1.3660586.

[16] A. Hamadeh *et al.*, “Full control of the spin-wave damping in a magnetic insulator using spin-orbit torque,” *Phys. Rev. Lett.*, vol. 113, no. 19, p. 197203, 2014, doi: 10.1103/PhysRevLett.113.197203.

[17] L. Liu, C.-F. Pai, Y. Li, H. W. Tseng, D. C. Ralph, and R. A. Buhrman, “Spin-Torque Switching with the Giant Spin Hall Effect of Tantalum,” *Science*, vol. 336, no. 6081, pp. 555–558, May 2012, doi: 10.1126/science.1218197.

[18] Y. Fan *et al.*, “Magnetization switching through giant spin–orbit torque in a magnetically doped topological insulator heterostructure,” *Nat. Mater.*, vol. 13, no. 7, Art. no. 7, Jul. 2014, doi: 10.1038/nmat3973.

[19] S. Takei, B. I. Halperin, A. Yacoby, and Y. Tserkovnyak, “Superfluid spin transport through antiferromagnetic insulators,” *Phys. Rev. B*, vol. 90, no. 9, p. 094408, Sep. 2014, doi: 10.1103/PhysRevB.90.094408.

[20] S. Takei and Y. Tserkovnyak, “Superfluid Spin Transport Through Easy-Plane Ferromagnetic Insulators,” *Phys. Rev. Lett.*, vol. 112, no. 22, p. 227201, Jun. 2014, doi: 10.1103/PhysRevLett.112.227201.

[21] P. Stepanov *et al.*, “Long-distance spin transport through a graphene quantum Hall antiferromagnet,” *Nat. Phys.*, vol. 14, no. 9, Art. no. 9, Sep. 2018, doi: 10.1038/s41567-018-0161-5.

[22] W. Yuan *et al.*, “Experimental signatures of spin superfluid ground state in canted antiferromagnet Cr2O3 via nonlocal spin transport,” *Sci. Adv.*, vol. 4, no. 4, p. eaat1098, Apr. 2018, doi: 10.1126/sciadv.aat1098.

[23] D. D. Stancil and A. Prabhakar, *Spin Waves: Theory and Applications*. Springer US, 2009.

[24] M. Daquino, “Nonlinear Magnetization Dynamics in Thin-Films and Nanoparticles,” 2005, doi: 10.6092/UNINA/FEDOA/148.

[25] A. G. Gurevich and G. A. Melkov, *Magnetization Oscillations and Waves*. CRC Press, 1996.

[26] R. W. Damon and J. R. Eshbach, “Magnetostatic modes of a ferromagnet slab,” *J. Phys. Chem. Solids*, vol. 19, no. 3, pp. 308–320, May 1961, doi: 10.1016/0022-3697(61)90041-5.

[27] B. A. Kalinikos and A. N. Slavin, “Theory of dipole-exchange spin wave spectrum for ferromagnetic films with mixed exchange boundary conditions,” *J. Phys. C Solid State Phys.*, vol. 19, no. 35, pp. 7013–7033, Dec. 1986, doi: 10.1088/0022-3719/19/35/014.

[28] E. B. Sonin, “Spin currents and spin superfluidity,” *Adv. Phys.*, vol. 59, no. 3, pp. 181–255, May 2010, doi: 10.1080/00018731003739943.

[29] L. Landau and E. Lifshits, “ON THE THEORY OF THE DISPERSION OF MAGNETIC PERMEABILITY IN FERROMAGNETIC BODIES,” vol. 53, p. 9.

[30] W. F. Brown, *Micromagnetics*. New York; London: J. Wiley, 1963.

[31] T. L. Gilbert, “A phenomenological theory of damping in ferromagnetic materials,” *IEEE Trans. Magn.*, vol. 40, no. 6, pp. 3443–3449, Nov. 2004, doi: 10.1109/TMAG.2004.836740.

[32] A. Vansteenkiste, J. Leliaert, M. Dvornik, M. Helsen, F. Garcia-Sanchez, and B. Van Waeyenberge, “The design and verification of MuMax3,” *AIP Adv.*, vol. 4, no. 10, p. 107133, Oct. 2014, doi: 10.1063/1.4899186.

[33] O. Gladii, M. Haidar, Y. Henry, M. Kostylev, and M. Bailleul, “Frequency nonreciprocity of surface spin wave in permalloy thin films,” *Phys. Rev. B*, vol. 93, no. 5, p. 054430, Feb. 2016, doi: 10.1103/PhysRevB.93.054430.

[34] O. Dzyapko, “Magnon Kinetics in Quasi-Equilibrium under Parametric Pumping Leading to Bose-Einstein Condensation,” p. 128.

[35] R. M. White, *Quantum Theory of Magnetism: Magnetic Properties of Materials*, 3rd ed. Berlin Heidelberg: Springer-Verlag, 2007.

[36] J. E. Hirsch, “Spin Hall Effect,” *Phys. Rev. Lett.*, vol. 83, no. 9, pp. 1834–1837, Aug. 1999, doi: 10.1103/PhysRevLett.83.1834.

[37] J. Smit, “The spontaneous hall effect in ferromagnetics I,” *Physica*, vol. 21, no. 6, pp. 877–887, Jan. 1955, doi: 10.1016/S0031-8914(55)92596-9.

[38] J. Smit, “The spontaneous hall effect in ferromagnetics II,” *Physica*, vol. 24, no. 1, pp. 39–51, Jan. 1958, doi: 10.1016/S0031-8914(58)93541-9.

[39] L. Berger, “Emission of spin waves by a magnetic multilayer traversed by a current,” *Phys. Rev. B*, vol. 54, no. 13, pp. 9353–9358, Oct. 1996, doi: 10.1103/PhysRevB.54.9353.

[40] X.-L. Qi and S.-C. Zhang, “Topological insulators and superconductors,” *Rev. Mod. Phys.*, vol. 83, no. 4, pp. 1057–1110, Oct. 2011, doi: 10.1103/RevModPhys.83.1057.

[41] J. R. Dormand and P. J. Prince, “A family of embedded Runge-Kutta formulae,” *J. Comput. Appl. Math.*, vol. 6, no. 1, pp. 19–26, Mar. 1980, doi: 10.1016/0771-050X(80)90013-3.

[42] “scipy.integrate.solve_ivp — SciPy v1.5.4 Reference Guide.” https://docs.scipy.org/doc/scipy/reference/generated/scipy.integrate.solve_ivp.html (accessed Dec. 18, 2020).

[43] “Solve nonstiff differential equations — medium order method - MATLAB ode45.” https://www.mathworks.com/help/matlab/ref/ode45.html (accessed Dec. 18, 2020).

[44] E. Schlömann, “A Sum Rule Concerning the Inhomogeneous Demagnetizing Field in Nonellipsoidal Samples,” *J. Appl. Phys.*, vol. 33, no. 9, pp. 2825–2826, Sep. 1962, doi: 10.1063/1.1702557.

[45] “LLG Micromagnetics Simulator.” [Online]. Available: http://llgmicro.home.mindspring.com/.

[46] J. C. Slonczewski, “Current-driven excitation of magnetic multilayers,” *J. Magn. Magn. Mater.*, vol. 159, no. 1–2, pp. L1–L7, Jun. 1996, doi: 10.1016/0304-8853(96)00062-5.

[47] “The Go Programming Language.” https://golang.org/ (accessed Dec. 20, 2020).

[48] "mumax3." https://mumax.github.io/api.html (accessed Dec. 20, 2020).

[49] *mumax/3*. mumax, 2020.

[50] I. Dzyaloshinsky, "A thermodynamic theory of 'weak' ferromagnetism of antiferromagnetics," *J. Phys. Chem. Solids*, vol. 4, no. 4, pp. 241–255, Jan. 1958, doi: 10.1016/0022-3697(58)90076-3.

[51] T. Moriya, "Anisotropic Superexchange Interaction and Weak Ferromagnetism," *Phys. Rev.*, vol. 120, no. 1, pp. 91–98, Oct. 1960, doi: 10.1103/PhysRev.120.91.

[52] J. Xiao, A. Zangwill, and M. D. Stiles, "Boltzmann test of Slonczewski's theory of spin-transfer torque," *Phys. Rev. B*, vol. 70, no. 17, p. 172405, Nov. 2004, doi: 10.1103/PhysRevB.70.172405.

[53] "COMSOL Multiphysics Reference Manual," p. 1742.

[54] L. K. Brundle and N. J. Freedman, "Magnetostatic surface waves on a y.i.g. slab," *Electron. Lett.*, vol. 4, no. 7, pp. 132–134, Apr. 1968, doi: 10.1049/el:19680102.

[55] D. D. Stancil, *Theory of Magnetostatic Waves*. New York: Springer-Verlag, 1993.

[56] M. Bailleul, D. Olligs, and C. Fermon, "Propagating spin wave spectroscopy in a permalloy film: A quantitative analysis," *Appl. Phys. Lett.*, vol. 83, no. 5, pp. 972–974, Aug. 2003, doi: 10.1063/1.1597745.

[57] V. Vlaminck and M. Bailleul, "Current-Induced Spin-Wave Doppler Shift," *Science*, vol. 322, no. 5900, pp. 410–413, Oct. 2008, doi: 10.1126/science.1162843.

[58] V. Vlaminck and M. Bailleul, "Spin-wave transduction at the submicrometer scale: Experiment and modeling," *Phys. Rev. B*, vol. 81, no. 1, p. 014425, Jan. 2010, doi: 10.1103/PhysRevB.81.014425.

[59] S. Neusser *et al.*, "Anisotropic Propagation and Damping of Spin Waves in a Nanopatterned Antidot Lattice," *Phys. Rev. Lett.*, vol. 105, no. 6, p. 067208, Aug. 2010, doi: 10.1103/PhysRevLett.105.067208.

[60] "Low Level Measurements Handbook - 7th Edition | Tektronix." https://www.tek.com/document/handbook/low-level-measurements-handbook.

[61] S. T. B. Goennenwein *et al.*, "Non-local magnetoresistance in YIG/Pt nanostructures," *Appl. Phys. Lett.*, vol. 107, no. 17, p. 172405, Oct. 2015, doi: 10.1063/1.4935074.

[62] F. R. Aramst, M. Grace, and S. Okwit, "Low-Level Garnet Limiters," *Proc. IRE*, vol. 49, no. 8, p. 1308, 1961.

[63] K. L. Kotzebue, "Frequency-Selective Limiting," *IRE Trans. Microw. Theory Tech.*, vol. 10, no. 6, pp. 516–520, 1962.

[64] S. Carter, "Magnetically . Tunable Single-Crystal Microwave Filters Using Yttrium-Iron-Garnet Resonators," *IRE Trans. Microw. Theory Tech.*, vol. 30, pp. 252–260, 1961.

[65] R. W. Degrasse, "Low-Loss Gyromagnetic Coupling through Single Crystal Garnets," *J. Appl. Phys.*, vol. 30, no. 4, pp. 155S-156S, 1959, doi: 10.1063/1.2185865.

[66] E. Bankowski, T. Meitzler, R. S. Khymyn, V. S. Tiberkevich, A. N. Slavin, and H. X. Tang, "Magnonic crystal as a delay line for low-noise auto-oscillators," *Appl. Phys. Lett.*, vol. 107, no. 12, 2015, doi: 10.1063/1.4931758.

[67] J. D. Adam and S. N. Stitzer, "A magnetostatic wave signal-to-noise enhancer," *Appl. Phys. Lett.*, vol. 36, no. 6, pp. 485–487, 1980, doi: 10.1063/1.91516.

[68] M. P. Kostylev, A. A. Serga, T. Schneider, B. Leven, and B. Hillebrands, "Spin-wave logical gates," *Appl. Phys. Lett.*, vol. 87, no. 15, pp. 1–3, 2005, doi: 10.1063/1.2089147.

[69] R. C. Linares and E. L. Sloan III, “Epitaxial Growth of Narrow Linewidth Yttrium Iron Garnet Films,” *J. Cryst. Growth*, vol. 27, pp. 249–252, 1974.

[70] H. J. Levinstein, S. Licht, R. W. Landorf, and S. L. Blank, “Growth of HighQuality Garnet Thin Films from Supercooled Melts Growth of High-Quality Garnet Thin Films from Supercooled Melts,” *Appl. Phys. Lett.*, vol. 19, no. 11, p. 486, 1971, doi: 10.1063/1.1653784.

[71] M. Evelt, V. E. Demidov, V. Bessonov, S. O. Demokritov, J. L. Prieto, and M. Muñoz, “High-efficiency control of spin-wave propagation in ultra-thin Yttrium Iron Garnet by the spin-orbit torque,” *Appl. Phys. Lett.*, vol. 108, p. 172406, 2016, doi: 10.1063/1.4948252.

[72] V. E. Demidov, S. Urazhdin, A. B. Rinkevich, G. Reiss, and S. O. Demokritov, “Spin Hall controlled magnonic microwaveguides,” *Appl. Phys. Lett.*, vol. 104, no. 15, p. 152402, 2014, doi: 10.1063/1.4871519.

[73] K. An *et al.*, “Control of propagating spin waves via spin transfer torque in a metallic bilayer waveguide,” *Phys. Rev. B - Condens. Matter Mater. Phys.*, vol. 89, no. 14, p. 140405, 2014, doi: 10.1103/PhysRevB.89.140405.

[74] E. Padrón-Hernández, A. Azevedo, and S. M. Rezende, “Amplification of spin waves by the spin Seebeck effect,” *J. Appl. Phys.*, vol. 111, no. 7, p. 07D504, 2012, doi: 10.1063/1.3673419.

[75] M. Z. Hasan and C. L. Kane, “Colloquium: Topological insulators,” *Rev. Mod. Phys.*, vol. 82, no. 4, pp. 3045–3067, 2010, doi: 10.1103/RevModPhys.82.3045.

[76] Y. Fan and K. L. Wang, “Spintronics Based on Topological Insulators,” *Spin*, vol. 06, no. 02, p. 1640001, 2016, doi: 10.1142/S2010324716400014.

[77] J. E. Moore, “The birth of topological insulators,” *Nature*, vol. 464, pp. 194–198, 2010, doi: 10.1038/nature08916.

[78] X. L. Qi, T. L. Hughes, and S. C. Zhang, "Topological field theory of time-reversal invariant insulators," *Phys. Rev. B - Condens. Matter Mater. Phys.*, vol. 78, no. 19, p. 195424, 2008, doi: 10.1103/PhysRevB.78.195424.

[79] X. L. Qi and S. C. Zhang, "Topological insulators and superconductors," *Rev. Mod. Phys.*, vol. 83, no. 4, p. 1057, 2011, doi: 10.1103/RevModPhys.83.1057.

[80] H. Zhang, C.-X. Liu, X.-L. Qi, X. Dai, Z. Fang, and S.-C. Zhang, "Topological insulators in Bi2Se3, Bi2Te3 and Sb2Te3 with a single Dirac cone on the surface," *Nat. Phys.*, vol. 5, pp. 438–442, 2009, doi: 10.1038/nphys1270.

[81] J. E. Moore and L. Balents, "Topological invariants of time-reversal-invariant band structures," *Phys. Rev. B - Condens. Matter Mater. Phys.*, vol. 75, no. 12, p. 121306, 2007, doi: 10.1103/PhysRevB.75.121306.

[82] C. L. Kane and E. J. Mele, "Z2 topological order and the quantum spin hall effect," *Phys. Rev. Lett.*, vol. 95, no. 14, p. 146802, 2005, doi: 10.1103/PhysRevLett.95.146802.

[83] M. Jamali *et al.*, "Giant Spin Pumping and Inverse Spin Hall Effect in the Presence of Surface and Bulk Spin-Orbit Coupling of Topological Insulator Bi2Se3," *Nano Lett.*, vol. 15, no. 10, pp. 7126–7132, 2015, doi: 10.1021/acs.nanolett.5b03274.

[84] J. Han, A. Richardella, S. A. Siddiqui, J. Finley, N. Samarth, and L. Liu, "Roomerature Spin-Orbit Torque Switching Induced by a Topological Insulator," *Phys. Rev. Lett.*, vol. 119, no. 7, p. 077702, 2017, doi: 10.1103/PhysRevLett.119.077702.

[85] a a Baker, a I. Figueroa, L. J. Collins-McIntyre, G. van der Laan, and T. Hesjedal, "Spin pumping in Ferromagnet-Topological Insulator-Ferromagnet Heterostructures.," *Sci. Rep.*, vol. 5, p. 7907, 2015, doi: 10.1038/srep07907.

[86] A. R. Mellnik *et al.*, "Spin-transfer torque generated by a topological insulator," *Nature*, vol. 511, pp. 449–451, 2014, doi: 10.1038/nature13534.

[87] M. Lang *et al.*, "Proximity induced high-temperature magnetic order in topological insulator - Ferrimagnetic insulator heterostructure," *Nano Lett.*, vol. 14, no. 6, pp. 3459–3465, 2014, doi: 10.1021/nl500973k.

[88] Z. Jiang, C. Z. Chang, C. Tang, P. Wei, J. S. Moodera, and J. Shi, "Independent Tuning of Electronic Properties and Induced Ferromagnetism in Topological Insulators with Heterostructure Approach," *Nano Lett.*, vol. 15, no. 9, pp. 5835–5840, 2015, doi: 10.1021/acs.nanolett.5b01905.

[89] C. W. Sandweg, Y. Kajiwara, K. Ando, E. Saitoh, and B. Hillebrands, "Enhancement of the spin pumping efficiency by spin wave mode selection," *Appl. Phys. Lett.*, vol. 97, p. 252504, 2010, doi: 10.1063/1.3528207.

[90] S. O. Demokritov, B. Hillebrands, and A. N. Slavin, "Brillouin light scattering studies of confined spin waves: linear and nonlinear confinement," *Phys. Rep.*, vol. 348, no. 6, pp. 441–489, 2001, doi: http://dx.doi.org/10.1016/S0370-1573(00)00116-2.

[91] T. Schneider, A. A. Serga, B. Leven, B. Hillebrands, R. L. Stamps, and M. P. Kostylev, "Realization of spin-wave logic gates," *Appl. Phys. Lett.*, vol. 92, p. 022505, 2008, doi: 10.1063/1.2834714.

[92] D. D. Stancil and A. Prabnakar, *Spin Waves*. New York, NY: Springer, 2009.

[93] A. A. Serga, A. B. Chumak, and B. Hillebrands, "YIG magnonics," *J. Phys. Appl. Phys.*, vol. 43, p. 264002, 2010, doi: 10.1088/0022-3727/43/26/264002.

[94] E. Padrón-Hernández, A. Azevedo, and S. M. Rezende, "Amplification of spin waves in yttrium iron garnet films through the spin Hall effect," *Appl. Phys. Lett.*, vol. 99, no. 19, p. 192511, Nov. 2011, doi: 10.1063/1.3660586.

[95] A. Slavin and V. Tiberkevich, "Nonlinear Auto-Oscillator Theory of Microwave Generation by Spin-Polarized Current," *Adv. Magn.*, vol. 45, no. 4, pp. 1875–1918, 2009.

[96] V. E. Demidov, S. Urazhdin, E. R. J. Edwards, M. D. Stiles, R. D. McMichael, and S. O. Demokritov, "Control of magnetic fluctuations by spin current," *Phys. Rev. Lett.*, vol. 107, no. 10, p. 107204, 2011, doi: 10.1103/PhysRevLett.107.107204.

[97] M. Collet *et al.*, "Generation of coherent spin-wave modes in yttrium iron garnet microdiscs by spin-orbit torque.," *Nat. Commun.*, vol. 7, p. 10377, 2016, doi: 10.1038/ncomms10377.

[98] Y. Tserkovnyak, A. Brataas, and G. E. W. Bauer, "Theory of current-driven magnetization dynamics in inhomogeneous ferromagnets," *J. Magn. Magn. Mater.*, vol. 320, no. 7, pp. 1282–1292, 2008, doi: 10.1016/j.jmmm.2007.12.012.

[99] I. N. Krivorotov, N. C. Emley, J. C. Sankey, S. I. Kiselev, D. C. Ralph, and R. a Buhrman, "Time-domain measurements of nanomagnet dynamics driven by spin-transfer torques.," *Science*, vol. 307, no. 5707, 2005, doi: 10.1126/science.1105722.

[100] G. A.G. and M. G.A., "Magnetization Oscillations and Waves.pdf." CRC Press, Inc., 1996.

[101] V. Vlaminck and M. Bailleul, "Spin-wave transduction at the submicrometer scale: Experiment and modeling," *Phys. Rev. B - Condens. Matter Mater. Phys.*, vol. 81, no. 1, p. 014425, 2010, doi: 10.1103/PhysRevB.81.014425.

[102] H. Kurebayashi, O. Dzyapko, V. E. Demidov, D. Fang, a J. Ferguson, and S. O. Demokritov, “Controlled enhancement of spin-current emission by three-magnon splitting.,” *Nat. Mater.*, vol. 10, pp. 660–664, 2011, doi: 10.1038/nmat3053.

[103] M. Sparks, R. Loudon, and C. Kittel, “Ferromagnetic relaxation. I. Theory of the relaxation of the uniform precession and the degenerate spectrum in insulators at low temperatures,” *Phys. Rev.*, vol. 122, no. 3, pp. 791–803, 1961, doi: 10.1103/PhysRev.122.791.

[104] P. Pincus, M. Sparks, and R. C. Lecraw, “Ferromagnetic relaxation. II. the role of four-magnon processes in relaxing the magnetization in ferromagnetic insulators,” *Phys. Rev.*, vol. 124, no. 4, pp. 1015–1018, 1961, doi: 10.1103/PhysRev.124.1015.

[105] C. L. Ordóñez-Romero, B. A. Kalinikos, P. Krivosik, W. Tong, P. Kabos, and C. E. Patton, “Three-magnon splitting and confluence processes for spin-wave excitations in yttrium iron garnet films: Wave vector selective Brillouin light scattering measurements and analysis,” *Phys. Rev. B - Condens. Matter Mater. Phys.*, vol. 79, no. 14, p. 144428, 2009, doi: 10.1103/PhysRevB.79.144428.

[106] J. A. C. Bland and B. Heinrich, *Ultrathin Magnetic Structures*. 1994.

[107] S. O. Demokritov *et al.*, “Bose-Einstein condensation of quasi-equilibrium magnons at room temperature under pumping,” *Nature*, vol. 443, no. 7110, pp. 430–433, 2006, doi: 10.1038/nature05117.

[108] E. R. J. Edwards, H. Ulrichs, V. E. Demidov, S. O. Demokritov, and S. Urazhdin, “Parametric excitation of magnetization oscillations controlled by pure spin current,” *Phys. Rev. B - Condens. Matter Mater. Phys.*, vol. 86, no. 13, pp. 1–4, 2012, doi: 10.1103/PhysRevB.86.134420.

[109] V. Lauer *et al.*, “Spin-transfer torque based damping control of parametrically excited spin waves in a magnetic insulator,” *Appl. Phys. Lett.*, vol. 108, no. 1, 2016, doi: 10.1063/1.4939268.

[110] Z. Wang, Y. Sun, M. Wu, V. Tiberkevich, and A. Slavin, “Control of Spin Waves in a Thin Film Ferromagnetic Insulator through Interfacial Spin Scattering,” *Phys. Rev. Lett.*, vol. 107, no. 14, p. 146602, Sep. 2011, doi: 10.1103/PhysRevLett.107.146602.

[111] M. Evelt *et al.*, “High-efficiency control of spin-wave propagation in ultra-thin yttrium iron garnet by the spin-orbit torque,” *Appl Phys Lett*, p. 5, 2016.

[112] A. Navabi *et al.*, “Control of Spin-Wave Damping in YIG Using Spin Currents from Topological Insulators,” *Phys. Rev. Appl.*, vol. 11, no. 3, p. 034046, Mar. 2019, doi: 10.1103/PhysRevApplied.11.034046.

[113] G. Talmelli *et al.*, “Spin-Wave Emission by Spin-Orbit-Torque Antennas,” *Phys. Rev. Appl.*, vol. 10, no. 4, p. 044060, Oct. 2018, doi: 10.1103/PhysRevApplied.10.044060.

[114] N. Vlietstra, J. Shan, B. J. van Wees, M. Isasa, F. Casanova, and J. Ben Youssef, “Simultaneous detection of the spin-Hall magnetoresistance and the spin-Seebeck effect in platinum and tantalum on yttrium iron garnet,” *Phys. Rev. B*, vol. 90, no. 17, p. 174436, Nov. 2014, doi: 10.1103/PhysRevB.90.174436.

[115] P. S. J. Russell and W.-F. Liu, “Acousto-optic superlattice modulation in fiber Bragg gratings,” *JOSA A*, vol. 17, no. 8, pp. 1421–1429, Aug. 2000, doi: 10.1364/JOSAA.17.001421.

[116] Y. Kajiwara *et al.*, “Transmission of electrical signals by spin-wave interconversion in a magnetic insulator,” *Nature*, vol. 464, no. 7286, Art. no. 7286, Mar. 2010, doi: 10.1038/nature08876.

[117] L. J. Cornelissen, J. Liu, R. A. Duine, J. B. Youssef, and B. J. van Wees, “Long-distance transport of magnon spin information in a magnetic insulator at room temperature,” *Nat. Phys.*, vol. 11, no. 12, Art. no. 12, Dec. 2015, doi: 10.1038/nphys3465.

[118] J. Li *et al.*, “Observation of magnon-mediated current drag in Pt/yttrium iron garnet/Pt(Ta) trilayers,” *Nat. Commun.*, vol. 7, no. 1, Art. no. 1, Mar. 2016, doi: 10.1038/ncomms10858.

[119] H. Wu *et al.*, “Observation of magnon-mediated electric current drag at room temperature,” *Phys. Rev. B*, vol. 93, no. 6, p. 060403, Feb. 2016, doi: 10.1103/PhysRevB.93.060403.

[120] R. Lebrun *et al.*, “Tunable long-distance spin transport in a crystalline antiferromagnetic iron oxide,” *Nature*, vol. 561, no. 7722, Art. no. 7722, Sep. 2018, doi: 10.1038/s41586-018-0490-7.

[121] J. Han *et al.*, “Birefringence-like spin transport via linearly polarized antiferromagnetic magnons,” *Nat. Nanotechnol.*, vol. 15, no. 7, Art. no. 7, Jul. 2020, doi: 10.1038/s41565-020-0703-8.

[122] W. Xing *et al.*, “Magnon Transport in Quasi-Two-Dimensional van der Waals Antiferromagnets,” *Phys. Rev. X*, vol. 9, no. 1, p. 011026, Feb. 2019, doi: 10.1103/PhysRevX.9.011026.

[123] S. Takei, A. Yacoby, B. I. Halperin, and Y. Tserkovnyak, “Spin Superfluidity in the $\ensuremath{\nu}=0$ Quantum Hall State of Graphene,” *Phys. Rev. Lett.*, vol. 116, no. 21, p. 216801, May 2016, doi: 10.1103/PhysRevLett.116.216801.

[124] D. Wesenberg, T. Liu, D. Balzar, M. Wu, and B. L. Zink, “Long-distance spin transport in a disordered magnetic insulator,” *Nat. Phys.*, vol. 13, no. 10, Art. no. 10, Oct. 2017, doi: 10.1038/nphys4175.

[125] N. Thiery *et al.*, “Nonlinear spin conductance of yttrium iron garnet thin films driven by large spin-orbit torque,” *Phys. Rev. B*, vol. 97, no. 6, p. 060409, Feb. 2018, doi: 10.1103/PhysRevB.97.060409.

[126] J. Gückelhorn, T. Wimmer, S. Geprägs, H. Huebl, R. Gross, and M. Althammer, “Quantitative comparison of magnon transport experiments in three-terminal YIG/Pt nanostructures acquired via dc and ac detection techniques,” *Appl. Phys. Lett.*, vol. 117, no. 18, p. 182401, Nov. 2020, doi: 10.1063/5.0023307.

[127] G. Catalan and J. F. Scott, “Physics and Applications of Bismuth Ferrite,” *Adv. Mater.*, vol. 21, no. 24, pp. 2463–2485, 2009, doi: https://doi.org/10.1002/adma.200802849.

[128] D. Lebeugle, D. Colson, A. Forget, M. Viret, A. M. Bataille, and A. Gukasov, “Electric-Field-Induced Spin Flop in BiFeO 3 Single Crystals at Room Temperature,” *Phys. Rev. Lett.*, vol. 100, no. 22, p. 227602, Jun. 2008, doi: 10.1103/PhysRevLett.100.227602.

[129] R. D. Johnson *et al.*, “X-Ray Imaging and Multiferroic Coupling of Cycloidal Magnetic Domains in Ferroelectric Monodomain ${\mathrm{BiFeO}}_{3}$,” *Phys. Rev. Lett.*, vol. 110, no. 21, p. 217206, May 2013, doi: 10.1103/PhysRevLett.110.217206.

[130] R. Moubah, G. Schmerber, O. Rousseau, D. Colson, and M. Viret, “Photoluminescence Investigation of Defects and Optical Band Gap in Multiferroic BiFeO$_{3}$ Single Crystals,” *Appl. Phys. Express*, vol. 5, no. 3, p. 035802, Feb. 2012, doi: 10.1143/APEX.5.035802.

[131] J. M. Gomez-Perez *et al.*, “Absence of evidence of spin transport through amorphous Y3Fe5O12,” *Appl. Phys. Lett.*, vol. 116, no. 3, p. 032401, Jan. 2020, doi: 10.1063/1.5119911.

[132] S. Kawachi, H. Kuroe, T. Ito, A. Miyake, and M. Tokunaga, “Resistive memory effects in BiFeO3 single crystals controlled by transverse electric fields,” *Appl. Phys. Lett.*, vol. 108, no. 16, p. 162903, Apr. 2016, doi: 10.1063/1.4947467.

[133] B. Andrzejewski, A. Molak, B. Hilczer, A. Budziak, and R. Bujakiewicz-Korońska, “Field induced changes in cycloidal spin ordering and coincidence between magnetic and electric anomalies in BiFeO3 multiferroic,” *J. Magn. Magn. Mater.*, vol. 342, pp. 17–26, Sep. 2013, doi: 10.1016/j.jmmm.2013.04.059.

[134] K. Uchida *et al.*, “Spin Seebeck insulator,” *Nat. Mater.*, vol. 9, no. 11, Art. no. 11, Nov. 2010, doi: 10.1038/nmat2856.

[135] T. Kikkawa, K. Uchida, S. Daimon, Z. Qiu, Y. Shiomi, and E. Saitoh, “Critical suppression of spin Seebeck effect by magnetic fields,” *Phys. Rev. B*, vol. 92, no. 6, p. 064413, Aug. 2015, doi: 10.1103/PhysRevB.92.064413.

[136] S. Seki *et al.*, “Thermal Generation of Spin Current in an Antiferromagnet,” *Phys. Rev. Lett.*, vol. 115, no. 26, p. 266601, Dec. 2015, doi: 10.1103/PhysRevLett.115.266601.

[137] S. M. Wu *et al.*, “Antiferromagnetic Spin Seebeck Effect,” *Phys. Rev. Lett.*, vol. 116, no. 9, p. 097204, Mar. 2016, doi: 10.1103/PhysRevLett.116.097204.

[138] J. König, M. Chr. Bønsager, and A. H. MacDonald, “Dissipationless Spin Transport in Thin Film Ferromagnets,” *Phys. Rev. Lett.*, vol. 87, no. 18, p. 187202, Oct. 2001, doi: 10.1103/PhysRevLett.87.187202.

[139] H. Chen, A. D. Kent, A. H. MacDonald, and I. Sodemann, "Nonlocal transport mediated by spin supercurrents," *Phys. Rev. B*, vol. 90, no. 22, p. 220401, Dec. 2014, doi: 10.1103/PhysRevB.90.220401.

[140] H. Chen and A. H. MacDonald, "Spin-Superfluidity and Spin-Current Mediated Non-Local Transport," *ArXiv160402429 Cond-Mat*, Apr. 2016, Accessed: Nov. 05, 2020. [Online]. Available: http://arxiv.org/abs/1604.02429.

[141] H. Skarsvåg, C. Holmqvist, and A. Brataas, "Spin Superfluidity and Long-Range Transport in Thin-Film Ferromagnets," *Phys. Rev. Lett.*, vol. 115, no. 23, p. 237201, Dec. 2015, doi: 10.1103/PhysRevLett.115.237201.

[142] S. Takei and Y. Tserkovnyak, "Nonlocal Magnetoresistance Mediated by Spin Superfluidity," *Phys. Rev. Lett.*, vol. 115, no. 15, p. 156604, Oct. 2015, doi: 10.1103/PhysRevLett.115.156604.

[143] A. Qaiumzadeh, H. Skarsvåg, C. Holmqvist, and A. Brataas, "Spin Superfluidity in Biaxial Antiferromagnetic Insulators," *Phys. Rev. Lett.*, vol. 118, no. 13, p. 137201, Mar. 2017, doi: 10.1103/PhysRevLett.118.137201.

[144] W. Chen and M. Sigrist, "Spin superfluidity in coplanar multiferroics," *Phys. Rev. B*, vol. 89, no. 2, p. 024511, Jan. 2014, doi: 10.1103/PhysRevB.89.024511.

[145] W. Chen and M. Sigrist, "Dissipationless Multiferroic Magnonics," *Phys. Rev. Lett.*, vol. 114, no. 15, p. 157203, Apr. 2015, doi: 10.1103/PhysRevLett.114.157203.

[146] B. Flebus, S. A. Bender, Y. Tserkovnyak, and R. A. Duine, "Two-Fluid Theory for Spin Superfluidity in Magnetic Insulators," *Phys. Rev. Lett.*, vol. 116, no. 11, p. 117201, Mar. 2016, doi: 10.1103/PhysRevLett.116.117201.

[147] E. Iacocca, T. J. Silva, and M. A. Hoefer, “Breaking of Galilean Invariance in the Hydrodynamic Formulation of Ferromagnetic Thin Films,” *Phys. Rev. Lett.*, vol. 118, no. 1, p. 017203, Jan. 2017, doi: 10.1103/PhysRevLett.118.017203.

[148] B. I. HALPERIN and P. C. HOHENBERG, “Hydrodynamic Theory of Spin Waves,” *Phys. Rev.*, vol. 188, no. 2, pp. 898–918, Dec. 1969, doi: 10.1103/PhysRev.188.898.

[149] Y. K. Kato, R. C. Myers, A. C. Gossard, and D. D. Awschalom, “Observation of the Spin Hall Effect in Semiconductors,” *Science*, vol. 306, no. 5703, pp. 1910–1913, Dec. 2004, doi: 10.1126/science.1105514.

[150] S. O. Valenzuela and M. Tinkham, “Direct electronic measurement of the spin Hall effect,” *Nature*, vol. 442, no. 7099, Art. no. 7099, Jul. 2006, doi: 10.1038/nature04937.

[151] T. Kimura, Y. Otani, T. Sato, S. Takahashi, and S. Maekawa, “Room-Temperature Reversible Spin Hall Effect,” *Phys. Rev. Lett.*, vol. 98, no. 15, p. 156601, Apr. 2007, doi: 10.1103/PhysRevLett.98.156601.

[152] I. M. Miron *et al.*, “Perpendicular switching of a single ferromagnetic layer induced by in-plane current injection,” *Nature*, vol. 476, no. 7359, Art. no. 7359, Aug. 2011, doi: 10.1038/nature10309.

[153] E. Saitoh, M. Ueda, H. Miyajima, and G. Tatara, “Conversion of spin current into charge current at room temperature: Inverse spin-Hall effect,” *Appl. Phys. Lett.*, vol. 88, no. 18, p. 182509, May 2006, doi: 10.1063/1.2199473.

[154] A. V. Chumak *et al.*, “Direct detection of magnon spin transport by the inverse spin Hall effect,” *Appl. Phys. Lett.*, vol. 100, no. 8, p. 082405, Feb. 2012, doi: 10.1063/1.3689787.

[155] M. Tinkham, *Introduction to Superconductivity*. Courier Corporation, 2004.

[156] T. J. Rieger, D. J. Scalapino, and J. E. Mercereau, “Time-Dependent Superconductivity and Quantum Dissipation,” *Phys. Rev. B*, vol. 6, no. 5, pp. 1734–1743, Sep. 1972, doi: 10.1103/PhysRevB.6.1734.

[157] R. Tidecks, “CURRENT-INDUCED NONEQUILIBRIUM PHENOMENA IN QUASI-ONE-DIMENSIONAL SUPERCONDUCTORS-INTRODUCTION,” *Springer Tracts Mod. Phys.*, vol. 121, pp. 1-+, 1990.

[158] P. K. Amiri and K. L. Wang, “Voltage-controlled magnetic anisotropy in spintronic devices,” *SPIN*, vol. 02, no. 03, p. 1240002, Sep. 2012, doi: 10.1142/S2010324712400024.

[159] Y. Tserkovnyak and M. Kläui, “Exploiting Coherence in Nonlinear Spin-Superfluid Transport,” *Phys. Rev. Lett.*, vol. 119, no. 18, p. 187705, Nov. 2017, doi: 10.1103/PhysRevLett.119.187705.

[160] T. Schneider *et al.*, “Self-stabilizing spin superfluid,” Nov. 2018, Accessed: Nov. 05, 2020. [Online]. Available: https://arxiv.org/abs/1811.09369v1.

[161] Y. Liu, G. Yin, J. Zang, R. K. Lake, and Y. Barlas, “Spin-Josephson effects in exchange coupled antiferromagnetic insulators,” *Phys. Rev. B*, vol. 94, no. 9, p. 094434, Sep. 2016, doi: 10.1103/PhysRevB.94.094434.

[162] Y. Liu, I. Barsukov, I. Krivorotov, Y. Barlas, and R. K. Lake, “Spin superfluid Josephson oscillator,” Jul. 2018, Accessed: Nov. 05, 2020. [Online]. Available: https://arxiv.org/abs/1807.01045v1.

[163] Y. Fan *et al.*, “Electric-field control of spin–orbit torque in a magnetically doped topological insulator,” *Nat. Nanotechnol.*, vol. 11, no. 4, Art. no. 4, Apr. 2016, doi: 10.1038/nnano.2015.294.

[164] C. Tang *et al.*, “Dirac surface state–modulated spin dynamics in a ferrimagnetic insulator at room temperature,” *Sci. Adv.*, vol. 4, no. 6, p. eaas8660, Jun. 2018, doi: 10.1126/sciadv.aas8660.

[165] H. Wang, C. Du, P. C. Hammel, and F. Yang, “Antiferromagnonic Spin Transport from ${\mathrm{Y}}_{3}{\mathrm{Fe}}_{5}{\mathrm{O}}_{12}$ into NiO,” *Phys. Rev. Lett.*, vol. 113, no. 9, p. 097202, Aug. 2014, doi: 10.1103/PhysRevLett.113.097202.

[166] W. Lin, K. Chen, S. Zhang, and C. L. Chien, “Enhancement of Thermally Injected Spin Current through an Antiferromagnetic Insulator,” *Phys. Rev. Lett.*, vol. 116, no. 18, p. 186601, May 2016, doi: 10.1103/PhysRevLett.116.186601.

[167] C. Safranski, E. Montoya, A. Smith, J.-R. Chen, and I. Krivorotov, “Easy-Plane Spin Hall Nano-Oscillator,” p. A22.001, 2018.